POLITECNICO DI TORINO

Facoltà di Ingegneria
Corso di Laurea in Ingegneria Aerospaziale

Sensitivity Analysis of Analytical Model for the Prediction of Trailing Edge Noise

Tutor: *prof. Renzo Arina*
Tutor: *prof. Andrea Ferrero*

Candidato: Gerardo Zampino

Abstract

Airfoil self-noise is defined as the acoustic emission by an airfoil immersed in uniform and steady fluid flow. As in most aeroacoustic noise generation situations, it is emitted by flow unsteadiness that interacts with the body surface and leads to broadband noise. There are mainly two broadband noise-generating mechanisms: the turbulence-interaction noise, involving the breakdown of oncoming vortexes on the leading edge of the airfoil, and the boundary-layer turbulence scattering at the trailing edge, known as trailing-edge (TE) noise.

In future, the increasing air traffic and the proximity of airport to the cities will produce several noise problems for the inhabitants. For this reason, noise prediction models assume increasing importance. Noise emission has to be reduced in order to guarantee an high comfort for both passengers and citizens. Another interesting application field is related to the wind turbines. They produce typical broadband noise that has negative effects on health, mainly psychological, for who lives around the wind farms. Reducing broadband noise is one of the main requirement for wind turbine design. However, airfoil self-noise is only a contribution of the acoustic pollution.

Keeping in mind the necessity of an accurate acoustic model during the design phase, this document provides a useful approach for noise prediction. The thesis consists firstly into a comparison of several analytical methods that allow to predict the sound pressure level for TE noise, in far field approximation, generated by airfoils at different angle of attack, immersed into an high Reynolds flux. Several models are studied to find an optimum configuration that well approximates the experimental measurements. However, in experiments, the different sound sources, due to the turbulence phenomena around the body, are not completely discernible. The contribution of radiated TE noise is studied for two geometries: NACA0012, a classical example of symmetrical airfoil used for wind design, and DU96-W-180, asymmetrical profile applied in wind turbines. This allows to evaluate in which geometrical configuration the acoustic prediction is more accurate.
The acoustic model is implemented in post processing data. The pressure, velocity and wall stress distribution around the profile are obtained using a numerical simulation based on Reynolds Averaged Navier-Stokes (RANS) equations with Spalart-Allmaras turbulent model.

Amiet's theory, described in reference [1], is the first model introduced in literature. As far as concern analytical aspects, the method is based on the Power Spectrum Density (PSD) and on the introduction of correlation length as function of the frequency, according to Corcos hypothesis. However, the condition of high shape ratio must be satisfied.

The pressure spectrum is obtained using empirical models such developed by Goody[2], Rozenberg[3], Kamuruzzaman[4] or Lee [5]. A simple solution was proposed by Amiet in his principal work but omitted in following chapters. Finally, the solutions are compared with experimental data [6, 7].

A sensitivity analysis is carried out in order to understand how the output of each pressure model is influenced by the boundary-layer quantities predicted with RANS simulations. Monte Carlo method is combined with Saltelli's approach which introduces global sensitivity factors useful to quantify the weight of each input parameter and estimate how the uncertainty propagates into the studied analytical models for the calculus of pressure spectrum density.

Contents

List of Figures

List of Tables

Part I

Airfoil Self-noise prediction theory

Chapter 1

Acoustic Theory

1.1 Introduction

An Airfoil immersed in turbulent flow generates sound due to unsteady flow interactions with a sharp-edge body. The overall sound radiated by a flap of wind turbines or a wing is the result of different mechanisms. It is possible to distinguish between the broadband noise and tonal noise. The first contribution is a matter of great interest in technologies that utilize sharp shapes, while tonal emission is almost negligible. The causes of the present distinction have to be found in two main reasons: the low pressure level and high frequencies that escapes the human hearing frequency range. Thus, the broadband noise is the only contribution for a structure with airfoil-like shapes in not accelerated motion.

There are mainly three noise-generating mechanisms. The turbulence-interaction noise is defined as a broadband radiated sound by the upstream turbulence involving the breakdown of oncoming vortexes on the leading edge of the airfoil. Boundary-layer turbulence scattering at the trailing edge is the source of trailing-edge noise (TE). Turbulent eddies are formed within the boundary layer and the interaction with the TE generates broadband aerodynamic noise. In acoustic terms, the edge presents itself as a sharp impedance discontinuity, scattering acoustic waves generated by fluid turbulence and creates an intensified radiated acoustic field.

Tonal emission is a property of vortex shedding noise, more typical for bluntness trailing edge. The narrow-band radiation is concentrated around a Strouhal peak value as a function of external flow speed such demonstrated by Brooks et Al. [6] with empirical formula. Intense turbulent eddies incoming from trailing edge are able to break coherent vortexes and reduce the amplitude of emission. For this reason, in high turbulent flow, vortex-shedding noise is not observed. Roger [8] developed a new model based on the solution of a reversed Sears' problem. It consists into an adaptation of Sears' lift fluctuations due to the stream disturbances, by introducing reverse flow velocity in order to include the Vortex-Shedding noise in the acoustic overview.

In 1959 Powell [9] firstly studied the problem of trailing-edge noise at low Mach number. However, Powell's model does not describe the real effect of pressure spectrum on the generation noise and the acoustic results are not congruent with experimental data. The author demonstrated the sound power is a function of flow velocity as $U_\infty^{4.6}$ but the

sound directivity is not defined. Powell's theory was a strong incentive to continue exploration of the turbulent noise emission as effect of pressure spectrum on the body surface. And it contributed to the elaboration of analytical studies that proposed alternatives for Lighthill acoustic analogy, defined as exact but expensive solution because of the interpretation of quadrupole source term. The theoretical methods, based on the linearized hydroacoustics equations, were developed to relate the pressure fluctuations on or near the edges of airfoil to the sound field. Crighton [10], Jones [11], Chase [12, 13] and Amiet [1] firstly described the self-noise production using Schwartzschild solution[14]. Chase formulated the problem by using Green function for zero mean flow and the noise problem was linked to surface pressure. The theory was developed for a semi-infinite plate without leading edge. Thus, the turbulence-interaction noise is neglected. This limitation does not influence the trailing-edge generation mechanism.
However, corrective theories introduced a series of hypothesis that allow to extend the Amiet's solution in many realistic applications for a shape ratio higher than 10. Roger and Moreau [15], proposed a back-scattering correction for Amiet's trailing-edge model in order to explain all effects of limited chord length. In the paper, Roger's model shows excellent results for low Helmhotz number, for which the chord is considered as acoustically compact. Small airfoils technologies are more subjected to scattering correction.

In 1978 Howe[16] published an unified theory of trailing edge noise. Howe's model tried to solve the acoustic problem for an high subsonic Mach number and he released a modified formula for Sound Pressure Level as function of Doppler factors. Moreover, the forward flight effects are implemented.

Kutta-Joukowski condition has to be discussed. It is defined as the correction of the circulation value of the flow around a sharp airfoil necessary to force a stagnation point on trailing edge. Jones[11], Crighton[10] and Howe were not able to refine how Kutta hypothesis should be applied for theoretical modeling. Howe's model demonstrates that using Kutta condition, Amiet's formula predictions exceeds that predicted by implementing Kutta condition of about 10 dB. Hence, in two-dimensional problems, removing a singularity at trailing edge leads a reducing radiation noise due to the sound interference that removes the oncoming turbulent flow contribution.

In late '80s, the development of computational fluid dynamics (CFD) and computational aeroacoustics (CAA) solved the problem of noise radiation for a large series of bodies immersed in turbulent flow. The computational aeroacoustics consists into solving the Ffowcs Williams and Hall equations by introducing an opportune noise source that generates the main pressure input on the body surface. The source type depends on the interaction between the wall and the external flow. Hence, the signal propagates in the entire domain discretized by a very thin mesh.
The numerical approach has an important limitation and direct simulation or hybrid techniques are preferred to describe the tiniest details of the sound generating mechanisms. For CAA methods, computational cost is not always suitable by calculators and this aspects implies an expensive time-consuming. The domain has to be discretized by introducing very small elements in order to correctly reproduce the acoustic propagation.

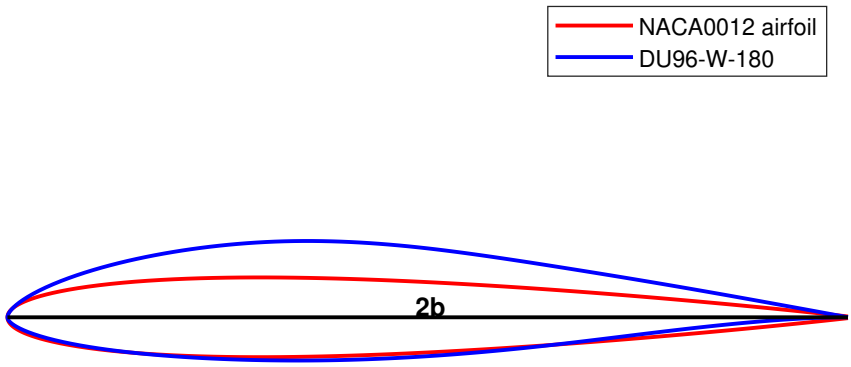

Figure 1.1: Comparison of the section geometries.

Thus, the total number of steps increases, in respect of that necessary for a classical CFD unsteady solution. On the other hand, analytical methods, based on acoustic analogy and wave scattering, are not devoted to reproducing the details of noise generating mechanisms, but rather to provide acceptable order of magnitude of the generated sound with fast and inexpensive calculations. Hybrid methods appear to be important for industrial applications because of reduced computational cost and good approximation of acoustical results. They are defined as a mixed approach that comes out from a combination of aerodynamic and acoustic equations: the fluid field, solution of the CFD simulation, is the main disturbance that represents the source term in the acoustic equation. The aerodynamics provides the pressure fluctuations on body surface while the acoustic equation provides the propagation mechanism. Examples are given by hybrid LES coupled with Ffowcs Williams and Hall far-field propagation or simplified theoretical surface pressure spectrum associated to a far-field propagation method.

Useful tool for noise prediction is proposed in following chapters. Firstly, the boundary layer profile is obtained as output of Reynolds Averaged Navier-Stokes (RANS) equations with Spalart-Allmaras turbulent model. Secondly, the Amiet's trailing edge theory is applied[17]. However, models like Amiet's trailing-edge noise are applied only for simple configurations such as flat plate or thin airfoil.
The contribution of radiated TE noise is studied for two geometries: NACA0012, a classical example of symmetrical airfoil used for wing design, and DU96-W-180, asymmetrical profile applied in wind turbines. The theoretical results are compared with experimental data.

NASA financed a series of experiments conducted by Brooks, Pope and Marcolini[6] that produced a document in which are analyzed velocity and incident effects on five different chord length NACA0012 profile. Tripped and untripped boundary layer are discussed. Furthermore, the empirical method were developed to compute intensity level due to the different noise mechanisms. The approach proposed by the authors is known as BPM model and it is still used in many applications. In reference [7] different analytical methods, mainly numerical, are applied on NACA0012 and DU96-W-180 profiles at varying incident and flow speed and compared with experimental data.

The acoustic analysis has important applications in wind turbines. The wind farms, close to the towns, have impact on the citizens wellness. The acoustic pollution, due to the incessant rotating blades, could cause a reduction of the attention, sleep disorder and annoyance. During the '90s several studies were conducted in order to define the best airfoil configuration that combines high performances and low sound level. The classical 4 digit NACA series 44 or the 6 digit series 63, were common airfoil families used for the design of wind turbines. However, they suffers a degradation of the performance because of premature transition. The DU series were introduces by Delft university[19] with different characteristics during the years. The DU96-W-180 is an example of profile designed for wind turbine applications. In the general DU yy-W-xxx airfoil series, 'DU' indicates the Delft University, followed by the last two digits of the year in which the profile was designed. The letter 'W' means that the main application is for the wind turbines and the last three digits are the ten times the maximum thickness.

In reference [18] the hybrid approach combining LES and the FWH acoustic analogy is used to predict the far field emissions and the authors demonstrate a good agreement with the experimental results. Merino Martinez et Al. designed a modified DU profile to introduce the reduction mechanism of the noise emission with flow-misaligned serrations at a high Reynolds number[20].
In the present paper, the DU96-W-180 profile is selected in order to demonstrate the validity of the hybrid proposed approach also for not symmetrical design. However, in real applications for wind turbines, the Reynolds number is very low and the acoustic emission is about 30 dB. Moreover, the experimental design in ref. [20] does not respect the present approach hypothesis. A future development of the present work consists into extension of the Amiet's theory for complex three dimensional configurations with taper and warp design.

1.2 Amiet's analytical theory

The main problem that the hybrid methods try to solve consists into reducing the time-consuming for the classical numerical approaches, without compromise the expected results; for this reason Amiet's theory represents an important starting point for the future applications because of its simple concept and good acoustic compliance with experimental data. However, it needs a series of input that are not available without a boundary layer simulation and a pressure spectrum that is obtained according to semi-empirical models. Amiet published in 1975 a new theory for trailing-edge noise prediction based on Schwartzchild solution. The author observed the airfoil immersed in turbulent flow produces acoustic noise due to gusts oncoming on the surface of the body. A typical eddy is composed by parallel gusts related to the trailing edge and skewed components. Even though the parallel type is the main cause of far-field sound emission and it is a simple contribution to compute, the skewed gusts produce a deleting lift fluctuations due to adjacent spanwise stations. For this reason, the pressure fluctuations in spanwise direction need major attentions. Spanwise fluctuations are neglected in the following chapters because of the fixed observer position in the mid-span section.

The basic assumption consists into turbulent stationary flow. Hence, turbulent veloc-

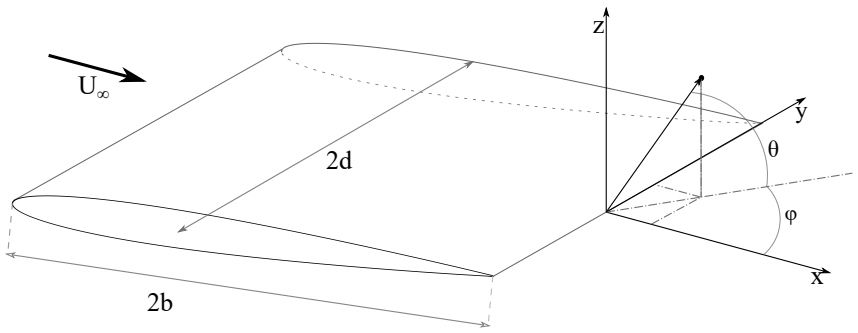

Figure 1.2: Scheme of the reference axis on the trailing edge.

ity field is not affected by the trailing-edge presence and the edge noise would exist even without the leading-edge. The convecting pressure pattern is generated by gusts past the trailing edge. The airfoil is assumed to have semi-infinite chord; thus, no leading edge exists. The hypothesis is valid for an acoustic compact body and the chord is mainly larger than the acoustic wavelength. The entire acoustic phenomena can be reproduced by two-dimensional simulation. The two-dimensional approach allows to drastically reduce the computational cost. For this reason the mesh has to be improved for only the characteristic section. This is possible to be implemented because of the high shape ratio and no taper or warp. The airfoil has constant shape all along the spanwise direction and the extremity vortexes are neglected. Thus, the distribution of pressure fluctuations is constant all along the wing.

The demonstration of the Amiet's formula takes part from the introduction of Schwartzchild solution. It is useful to divide the solution into two parts: firstly the plate is extended in order to obtain an infinite airfoil in both upstream and downstream directions; secondly the convective surface pressure is extended over the imaginary downstream part and it is added to a dipole distribution. However, a second solution is needed to delete the contribution of downstream airfoil. In real configuration, the chord is limited and Amiet's theory is not completely adapted for the acoustic prediction. The finite chord is hidden in the pressure spectra definition that is influenced by the RANS solution and the Amiet's formulation is adopted, though. The finite chord problem was solved by Roger [15] that complicated the Amiet's formula without a necessary improving model performances.

For the following dissertation, an airfoil of chord $2b$ and span $2d$ in a turbulent flow with mean speed U_∞ is considered. The reference coordinate system has origin at the mid-span section of the airfoil, in correspondence with trailing-edge. The y coordinate extends along spanwise direction, while x axis is direct in flow field direction. Finally, the z axis is normal to wing surface. The scheme is presented in the Figure 1.2, where the observer position is over the trailing edge along the z-axis. The angle ϕ and θ, define the observer location in polar coordinates. The SPL mainly depends on the observer position and decreases in function of the distance from the trailing edge.

The speed components are u, v and w, respectively along x, y and z axis. The turbulence is assumed to be frozen and turbulent velocity can be written as function of double spatial Fuorier transformation of w in the variables x and y. The Fourier components $\hat{w}_R$

are functions of wavenumbers in chordwise and spanwise directions can be calculated as

$$\hat{w}_R = \frac{1}{4\pi^2} \int \int_{-R}^{+R} w(x,y) e^{-i(k_x x + k_y y)} \mathrm{d}x \mathrm{d}y \tag{1.1}$$

where k_x and k_y are the wavenumbers, and R is a large but finite value, necessary to solve the integral.
Turbulent velocity is defined as

$$\tilde{w}(x,y,t) = \int \int_{-\infty}^{\infty} \hat{w}_R(k_x,k_y) e^{i[k_x(x-Ut)+k_y y]} \mathrm{d}k_x \mathrm{d}k_y \tag{1.2}$$

The distribution of pressure jump on flat plate was described by Amiet in reference [21]. Thus,

$$\Delta P(x,y,t) = 2\pi\rho_\infty U b \int \int_{-\infty}^{\infty} \hat{w}_R(k_x,k_y) g(x,k_x,k_y) e^{i(k_y y - k_x U t)}, \tag{1.3}$$

where the function $g(x,k_x,k_y)$ is the airfoil pressure distribution for sinusoidal gust. Fourier transformation is applied in order to introduce a frequency dependence. The integration interval is $-R/U_\infty < t < R/U_\infty$. Considering

$$\int_{-R/U_\infty}^{R/U_\infty} e^{i\xi t} \mathrm{d}t = 2\pi\delta(\xi), \tag{1.4}$$

the pressure distribution is obtained as

$$\Delta\hat{P}(x,y,\omega) = 2\pi\rho_\infty b \int_{-\infty}^{\infty} \hat{w}_R(k_x,k_y) g(x,K_x,k_y) e^{ik_y y} \mathrm{d}k_y, \tag{1.5}$$

where $K_x = -\omega/U_\infty$ is the chordwise turbulent wavenumber. As far as concern, the statistical definition of pressure fluctuations on the surface of the airfoil is a consequence of turbulent stochastic phenomena.
The cross power spectral density (cross-PSD) is defined by equation:

$$S_{qq}(x_1,x_2,y_1,y_2,\omega) = \lim_{R/U_\infty \to \infty} \left\{ \frac{\pi}{T} \mathrm{F}_{av} \left[\Delta\hat{P}^*(x_1,y_1,\omega) \Delta\hat{P}(x_2,y_2,\omega) \right] \right\}. \tag{1.6}$$

From equation (1.5), the expected value F_{av} in (1.6) can be reduced as

$$\mathrm{F}_{av} \left[\hat{w}_R(K_x,k_y) \hat{w}_R^*(K_x,k_y) \right] = \frac{R}{\pi} \delta(k_y - k_y') \phi_{ww}(k_x,k_y'), \tag{1.7}$$

where

$$\phi_{ww}(k_x,k_y) = \int_{-\infty}^{\infty} \phi_{ww}(k_x,k_y,k_z) \mathrm{d}k_z, \tag{1.8}$$

is the energy spectrum of turbulence.

Combining (1.5) and (1.7), it can be written

$$S_{qq}(x_1,x_2,y_2-y_1,\omega) = 4\pi^2\rho_\infty^2 b^2 U \int_{-\infty}^{\infty} g^*(x_1,K_x,k_y) g(x_2,K_x,k_y) \phi_{ww}(K_x,k_y) e^{ik_y(y_2-y_1)} \mathrm{d}k_y. \tag{1.9}$$

The difference $y_2 - y_1$ is the distance between the two points in spanwise direction for which the cross-PSD is computed. According to Curle and Kirchhoff, the far-field sound can be modeled by a surface dipole distribution equal in strength to the total force on the airfoil. The far-field pressure can be obtained integrating equation (1.6) over the airfoil surface. However, it is possible to demonstrate the PSD is related to cross-PSD. Thus,

$$S_{pp}(x,y,z,\omega) = \left(\frac{\omega z}{4\pi c_0 \sigma^2}\right)^2 \iiint S_{qq}(x_1,x_2,y_2-y_1,\omega) e^{\frac{i\omega}{c_0}\left[\beta^{-2}(x_1-x_2)(M-\frac{x}{\sigma})+y\frac{y_2-y_1}{\sigma}\right]} \mathrm{d}x_1 \mathrm{d}x_2 \mathrm{d}y_1 \mathrm{d}y_2. \tag{1.10}$$

where $\beta^2 = 1 - M^2$ and $\sigma^2 = x^2 + \beta^2(y^2 + z^2)$. Substituting the equation (1.9) in (1.10), the far-field acoustic PSD assume a simplified form. It allows to rewrite far-field PSD as following:

$$S_{pp}(x,y,z,\omega) = \left(\frac{\omega z \rho_\infty b}{c_0 \sigma^2}\right)^2 U_\infty d\pi \int_{-\infty}^{\infty} \left[\frac{\sin^2(dk_y + d\omega y/c_0\sigma)}{(dk_y + d\omega y/c_0\sigma)\pi}\right] |\mathcal{L}(x,K_x,k_y)|^2 \phi_{ww}(K_x,k_y)\mathrm{d}k_y, \tag{1.11}$$

where $\mathcal{L}$ is the chordwise integral of the surface loading. The function $\mathcal{L}$, is written as

$$\mathcal{L}(x,K_x,k_y) = \int_{-b}^{b} g(x_0,K_x,k_y) e^{-i\omega x_0 (M - x/\sigma)/c_0\beta^2} \mathrm{d}x_0. \tag{1.12}$$

If the frequency is small, the function $\mathcal{L}$ is reduced to the sectional lift. For a large aspect ratio airfoil, the assumption of infinite span is still valid. On the other hand, for high frequencies and small turbulent scale, large aspect assumption in not necessary.

The incident gusts are the main causes of sound generation and they are characterized by an own wavelength. As the wavelength decreases, the load tends to be concentrated near the leading edge; for this reason the influenced spanwise region becomes smaller and smaller. In fact, in equation (1.11) the ratio between sine function and its argument tends to infinitesimal value.
For an observer in mid-span section, only $k_y = 0$ gust contributes to the sound, while the skewed gusts have symmetrical effects that does not affect the observer's perception. In the general case $y \neq 0$ and $d \to \infty$, the argument of integral in equation (1.11) is replaced by $\omega y/c_0\sigma$. Hence, the PSD is written as

$$S_p p(x,0,z,\omega) \to \left(\frac{\omega z \rho_\infty b}{c_0 \sigma^2}\right)^2 \pi U_\infty d\, |\mathcal{L}(x,K_x,0)|^2 \phi_{ww}(K_x,0). \tag{1.13}$$

In conclusion, for a large span assumption, a two-dimensional airfoil theory for a compressible flow is enough accurate if used to compute the noise produced by oncoming gusts on the trailing edge. In fact, when d tends to a large value, the intersection point of a gust with the airfoil moves with subsonic velocity in the fluid direction and the sound produced is negligible. However, the surface pressure distribution over the airfoil is a function of both subsonic and supersonic gusts. Furthermore, the observer in far-field hears only the sound produced by gusts with acoustic wavefront normal to the line joining observer and airfoil.

1.2.1 Validity conditions of Amiet's Theory

The simple case of an observer at $y = 0$ plane section is considered in this work. However, it is important to understand which requirements allow to reduce the errors induced by approximation of infinite spanwise airfoil; therefore, the equation (1.13) carries out a valid result.
It is possible to demonstrate that integral value

$$\int_0^t \frac{\sin^2(\xi d)}{\xi^2} \mathrm{d}\xi \tag{1.14}$$

for $t = 10/d$ is about 90% of the result obtained for $t \to \infty$. For this reason the formula (1.13) had a good validity for $k_y > 10/d$. The function ϕ_{ww} is not sensitive to k_y if it is much less than K_x. Therefore, for $K_x >> 10/d$, ϕ_{ww} in equation (1.10) can be taken outside the integral. The similarity rules were presented by Graham[22]. He showed for $MK_x >> k_y$ that the response is independent from k_y.

Amiet's theory is rigorous when $MK_x d$ tends to infinity value. According to the present assumption, functions $\mathcal{L}$ and ϕ_{ww} are not dependent on k_y and the PSD can be written as:

$$S_{pp}(x, y, z, \omega) = \left(\frac{\omega z \rho_\infty b M}{\sigma}\right) d \left|\mathcal{L}(x, K_x, 0)\right|^2 l_y(\omega) S_{ww}(\omega) \tag{1.15}$$

where $l_y(\omega)$ is the cross-correlation length and S_{ww} is the Pressure Spectral Density of velocity fluctuation in z direction. The correlation length is calculated by definition as

$$l_y(\omega) = \frac{1}{R_{ww}(K_x, 0)} \int_0^\infty R_{ww}(K_x, y) \mathrm{d}y = \pi \phi_{ww}(K_x, 0) / R_{ww}(K_x, 0); \tag{1.16}$$

in which R_{ww} is the Fourier transformation of ϕ_{ww} in respect of k_y variable.

1.2.2 Airfoil pressure response function by Schwartzschild solution

The airfoil pressure response function can be obtained from the general Schwartzschild solution, as described by Amiet in reference [23]. The flat plate extends from $\bar{x} = -2$ to $\bar{x} = 0$; where the symbol $\bar{\cdot}$ indicates not dimensional quantities divided by semichord b.
The linearized equation for velocity potential Φ is given by:

$$\left[\nabla^2 - M^2 \left(\frac{b}{U}\frac{\partial}{\partial t} + \frac{\partial}{\partial \bar{x}}\right)^2\right] \Phi(\bar{x}, z, t) = 0. \tag{1.17}$$

The boundary conditions have to be imposed:

$$\Phi(\bar{x}, 0, t) = 0 \qquad \bar{x} \leq -2 \tag{1.18}$$

$$\frac{\partial \Phi}{\partial z}(\bar{x}, 0, t) = b w(\bar{x}) e^{i\omega t} \qquad -2 < \bar{x} < 0 \tag{1.19}$$

$$\frac{\mathrm{D}\Phi}{\mathrm{D}t} = 0 \qquad \bar{x} \geq 0 \tag{1.20}$$

where D/Dt is the lagrangian derivative. A sinusoidal in time assumption is used in order to simplify the solution as a product between a spatial function $\varphi(\bar{x}, z)$ and an exponential one $e^{i\omega t}$. Considering the coordinates transformation

$$\bar{x} \to \bar{X} \quad z \to Z/\beta \quad \omega t \to T - M\mu\bar{X}$$

the boundary formulation can be written as:

$$\varphi_{xx} + \varphi_{zz} + \mu^2\varphi = 0, \tag{1.21}$$

with

$$\varphi(\bar{X}, 0) = 0 \qquad \bar{X} \leq -2 \tag{1.22}$$

$$\frac{\partial\varphi}{\partial z}(\bar{X}, 0) = \frac{b}{\beta} w(\bar{X}) e^{-iM\mu X} \qquad -2 < \bar{X} < 0 \tag{1.23}$$

$$(i\bar{K_x} + \frac{\partial}{\partial X})\varphi(\bar{X}, 0) = 0 \qquad X \geq 0. \tag{1.24}$$

The parameter μ is defined by $M\omega b/(U_\infty\beta^2)$.

According to Schwartzschild[14], the function φ satisfies both wave equation and the boundaries conditions

$$\varphi(\bar{X}, 0) = F(\bar{X}) \qquad \bar{X} > 0 \tag{1.25}$$

$$\varphi_z(\bar{X}, 0) = 0 \qquad \bar{X} < 0 \tag{1.26}$$

when it is written as

$$\varphi(\bar{X}, Z) = \frac{1}{\pi}\int_0^\infty G(\bar{X}, \xi, Z) F(\xi) \mathrm{d}\xi, \tag{1.27}$$

where $G(\bar{X}, \xi, 0) = (-\bar{X}/\xi)^{1/2}[1/(\xi - \bar{X})]e^{-i\mu(\xi-\bar{X})}$ for $\bar{X} < 0$ and $F(\bar{X})$ is function of the boundary conditions.

Solution for compressible gusts

Schwartzschild solution allows to satisfy only two conditions. For this reason, it is necessary to implement an iterative procedure that solves Sear's problem by introducing a series of corrections. All solutions satisfy the no permeability condition on airfoil surface, and one of the remaining boundary conditions of the problem.

The first solution, with only permeability condition, is found:

$$\varphi^{(0)}(\bar{x}, \bar{z}) = \frac{ib}{2\beta}\int_{-\infty}^{\infty} H_0^{(2)}\{\mu[(\bar{x} - \xi)^2 + \beta^2\bar{z}^2]^{1/2}\} w(\xi) e^{i\mu M(\bar{x}-\xi)} \mathrm{d}\xi, \tag{1.28}$$

in which H_0 is defined as Hankel function. For $\bar{x}$ where the airfoil is not present, the value $w(\bar{x})$ is important to solve the integral in equation (1.28). The Schwartzschild solution is necessary to remove $\varphi^{(0)}$ for $\bar{x} < -2$ due to the physics boundaries. However, to compute the correction of leading edge $\psi^{(1)}$, the flat plate is assumed to extend downstream to

infinity. From equation (1.27), with changed sign for $\bar{X}$, it is possible to obtain the leading edge correction as

$$\psi^{(1)}(\bar{x},0) = -\frac{1}{\pi}\int_0^\infty \left(\frac{\bar{x}}{\xi}\right)^{\frac{1}{2}} e^{-i\mu(1-M)(\bar{x}+\xi)}\varphi^{(0)}(-\xi,0)\frac{\mathrm{d}\xi}{\bar{x}+\xi}. \tag{1.29}$$

The total contribution, for upstream region is given by

$$\varphi^{(1)} = \varphi^{(0)} + \psi^{(1)}.$$

For the region downstream, it is valid the boundary condition $\mathrm{D}\varphi/\mathrm{D}t = 0$. Since the pressure is a function of the potential velocity, the downstream contribution is calculated as:

$$\varphi(\bar{x},\bar{z}) = -\frac{b}{\rho_\infty U_\infty}\int_{-\infty}^{\bar{x}} P(\xi,\bar{z})e^{-iK_x(x-\xi)}\mathrm{d}\xi. \tag{1.30}$$

Since the value of p and ψ are linearly related, p is a solution of wave equation. Hence, from (1.27) in real coordinates,

$$p^{(2)}(\bar{x},0) = -\frac{1}{\pi}\int_0^\infty \left(\frac{x}{\xi}\right)^{\frac{1}{2}} e^{-i\mu(1+M)(\bar{x}+\xi)}P^{(1)}(\xi,0)\frac{\mathrm{d}\xi}{\bar{x}+\xi}. \tag{1.31}$$

The correction $\varphi^{(2)}$ of the second step can be calculated by imposing in equation (1.30), $P^{(2)} = P^{(1)} + p^{(2)}$. However, the new solution $\varphi^{(2)}$ is not zero ahead of airfoil. So, it is used as input for the next step, to compute $\varphi^{(3)}$ until to reach a sufficient accuracy.

For the Sears problem, it is possible to compute a closed form for $P^{(1)}$, and from equation (1.29), it is written

$$\varphi_s^{(1)}(x,0) = (1-i)E[\bar{K}_x(1-M)\bar{x}]\varphi_s^{(0)}. \tag{1.32}$$

In conclusion, substituting the hypothesis of sinusoidal gust, for which

$$P = P_0 e^{i[\omega(t-x/U_\infty)]-k_y y}, \tag{1.33}$$

in equation (1.31), the airfoil pressure jump, with $k_y = 0$, at mid-span section, and normalized by P_0, is obtained as

$$g(\bar{x},K_x,\omega) = p^{(2)} = \left\{(1+i)E[-\bar{x}(\mu(1+M)+\bar{K}_x)] - 1\right\}e^{-i\bar{K}_x\bar{x}} \tag{1.34}$$

where the function E is a combination of Fresnel integrals. The function E is defined as:

$$E(x) = \int_0^x \frac{e^{-i\xi}}{\sqrt{2\pi\xi}}\mathrm{d}\xi. \tag{1.35}$$

1.3 Far-field solution

The airfoil response function is useful to compute the far-field noise from surface pressure spectrum. Standard techniques for spectral analysis can be used. However, the surface pressure field can be rather complex and for this reason some simplifying hypothesis are introduced.
In general cases, the pressure spectrum is composed by several spectral component with different wavenumber and convection velocity U_c, but the product $U_c K_x = \omega$ is almost constant. This aspect is necessary to compute the sum of all contributions due to all spectral components, in the same form of equation (1.33). The frequency is assumed to be known, the convection velocity is fixed as a certain percentage of free stream velocity, thus K_x is calculated. However, this assumption appears to be reasonable, due to the direct dependence from the frequencies. With the above approximation, the far-field sound emission is calculated from equation (1.15) for an observer in mid-span plane. Hence,

$$S_{pp}(x, 0, z, \omega) = \left(\frac{\omega b z}{2\pi c_0 \sigma}\right)^2 l_y(\omega) d \left|\mathcal{L}\right|^2 S_{ww}(\omega), \tag{1.36}$$

where c_0 is the sound speed, while $\mathcal{L}$ is the integral of airfoil pressure distribution calculated as

$$\mathcal{L} = \int_{-2}^{0} g(\xi, K_x, \omega) e^{-i\mu\xi(M - x/\sigma)} \mathrm{d}\xi. \tag{1.37}$$

The parameters are $\sigma^2 = x^2 + \beta^2 z^2$, $\beta^2 = 1 - M^2$ and $\mu = M\omega b/(U\beta^2)$. The integral in equation (1.37) has a closed form given by

$$\mathcal{L} = \frac{1}{\Theta}\left\{(1+i)\left[\sqrt{\frac{1 + M + \bar{K}_x/\mu}{1 + x/\sigma}} E(2\mu(1 + \frac{x}{\sigma})) e^{-i2\Theta} - E(2\mu(1+M) + 2\bar{K}_x)\right] + 1 - e^{-i2\Theta}\right\}, \tag{1.38}$$

where $\Theta = \bar{K}_x + \mu(M - x/\sigma)$. The above results are still valid until the hypothesis of a stationary turbulence past the edge is respected. For a turbulent boundary layer with no mean pressure gradient, Corcos assumption is introduced. The ratio between $S_{ww}(\omega, y)/S_{ww}(\omega, 0)$ is a function of only dimensionless variables and the cross-correlation length is given by

$$l_y(\omega) = 2.1 \frac{U_c}{\omega}. \tag{1.39}$$

Amiet proposed an empirical approximated formula in order to compute the surface pressure spectrum S_{ww} that is omitted in following discussion because of its inconsistent results in respect of the experimental data.

1.4 Surface pressure spectrum models

In general, the pressure on airfoil surface is complex to be described, due to its strong dependence on not stationary phenomena, such as gusts that flow over the profile. However,

many models was developed to answer the question about the frequency contribution of the pressure variation at different point along the chordwise. Goody[2], firstly proposed a solution of the problem. All following models are adaptation of Goody's one, by introducing more complex effects and the compressibility of fluid (Rozenberg[3] model is an example).
A general expression is here proposed, in which the constants assume a different value according to model used. In all cases, the pressure spectrum presents a not explicit Reynolds influence because it is hidden in the boundary layer quantities definition. Hence,

$$\frac{S_{ww}}{S_{ref}} = \frac{a(\omega^*)^b}{[i(\omega^*)^c + d]^e + [f R_T \omega^*]^h} \tag{1.40}$$

where ω^* is a not dimensional frequency and S_{ref} a reference value for which the pressure spectrum is scaled. R_T represents the time ratio between the inner and outer layer.

1.4.1 Goody's spectrum model

Goody proposed an empirical model to compute the power spectral density as function of Reynolds number and of boundaries quantities. The frequency affects the scaling pressure spectrum; in fact, the existence of an inner scaling or an outer scaling, define a different approach for pressure spectrum at local distance from the surface. The measured spectra decays as $\omega^{-0.8}$ for a large scale of Reynolds number. This assumption is correct only for low frequencies, while as $\omega \to \infty$, the model describes a more rapid decreasing, with exponent -5. In order to consider the different behavior on the entire range of frequencies, the parameter R_T is computed as

$$R_T = \frac{\delta}{U_e}\frac{u_\tau^2}{\nu} = \frac{\delta}{U_e}\frac{\tau_w}{\mu_f}, \tag{1.41}$$

where δ was used as boundary layer characteristic dimension while the inner variable $u_\tau^2 = \tau_w/\rho$, by definition. The spectrum is scaled by $S_{ref} = \tau_w^2\delta/U_e$, while $\omega^* = \omega\delta/U_e$. The Reynolds effect on the shape of pressure spectrum is to increase the size of the overlap range with experimental points. The speed U_e is the external velocity of the boundary layer.
In conclusion, Goody's model was developed only for zero gradient flow; for this reason it is not adapted for any airfoils.
The constants in the model are:

a=3	b=2	c=0.75	d=0.5	e=3.7
f=1.1	g=-0.57	h=7	i=1	

1.4.2 Rozenberg's spectrum model

In many applications, the turbulent boundary layer is affected by an adverse mean gradient for example on the suction side of a profile or a blade. Rozenberg's model was developed to introduce the compressibility at large Mach number and inside the boundary layer.

For this reason, Rozenberg's model is more accurate to describe the flow field around airfoils rather than Goody's one. In respect of Goody's model, the reference length is the displacement thickness δ^* and the scaled pressure is given by the stress near the surface where it assumes the maximum value. Considering Zagarola-Smits's parameter $\Delta = \delta/\delta^*$, as index of the the effect of pressure gradient, and the Clauser's equilibrium parameter

$$\beta_c = \frac{\theta}{\tau_w}\frac{\mathrm{d}p}{\mathrm{d}x},$$

it is possible to quantify the local gradient effect. Cole's constant Π is the wake strength parameter, obtained by solving the equation:

$$2\Pi - \ln(1+\Pi) = \kappa\frac{U_e}{u_\tau} - \ln\left(\frac{\delta^* U_e}{\nu}\right) - \kappa C - \ln\kappa, \tag{1.42}$$

where κ is the von Karman constant and $C = 5.2$. An analytical expression was proposed by Rozenberg in ref. [3], in which Cole's wake parameter is defined as function of β_c. Rozenberg obtained

$$\Pi = 0.8\left(\beta_c + 0.5\right)^{3/4}. \tag{1.43}$$

The constants in equation (1.40), according to Rozenberg's model, are defined by:

$a = [2.82\Delta^2(6.13\Delta^{-0.75} + d)^e][4.2(\Pi/\Delta) + 1]$ b=2 c=0.75
$d = 4.76(1.4/\Delta)^{0.75}[0.375e - 1]$ $e = 3.7 + 1.5\beta_c$ f=8.8 g=-0.57
$h = \min(3, 19/\sqrt{R_T}) + 7$ i=4.76

1.4.3 Kamruzzaman's spectrum model

Kamaruzzaman's model introduces a series of correction in the Rozenberg's formula by considering a series of experimental data for airfoils at different angle of attack. The previous model is modified as following described:

1. the denominator is changed in order to guarantee a decreasing trend like ω^{-5} as $\omega \to \infty$;

2. the exponent were modified to better agree with experimental measurement;

3. the Reynolds number dependence is better modeled;

4. the time ratio parameter R_T is calculated with δ^*.

The wall pressure spectrum is scaled by $\tau_w^2\delta^*/U_e$. The constants are summarized in following scheme.

$a = 0.45[1.75(\Pi^2\beta_c^2)^m + 15]$ b=2 c=1.637
d=0.27 e=2.47 $f = 1.15^{-2/7}$ g=-2/7
$m = 0.5[\delta^*/(1.31\theta)]^{0.3}$ i=1 h=7

1.4.4 Lee's spectrum model

Lee and Villaescusa [5] suggested an extended version of Rozenberg's model to obtain an accurate prediction for not symmetric and high leading airfoil. At high frequencies, the model assume a rapid decay for zero or low pressure gradient. For middle frequencies, Rozenberg presents an higher amplitude than Lee's model. For this reason, the constant d is modified as function of equilibrium parameter.

$a = [2.82\Delta^2(6.13\Delta^{-0.75} + d)^e][4.2(\Pi/\Delta) + 1]$	if $\beta_c > 50$	$a^* = \max(1, (0.25\beta_c - 0.52)a)$
b=2	c=0.75	f=8.8
d=0.27	if $\beta_c < 0.5$	$d = \max(1.0, 1.5d)$
$h = \min(5.35, 0.139 + 3.1043\beta_c, 19/\sqrt{R_T}) + 7$	if h=12.35	$h = \min(3, 19/\sqrt{R_T}) + 7$
g=-0.57	i=4.76	$e = 3.7 + 1.5\beta_c$

Chapter 2

Fluid dynamic physical models

The TE noise problem is solved starting from CFD simulation that allows to reconstruct the velocity and pressure field around the airfoil in two dimensional hypothesis. Boundary layer quantities for high Reynolds number and compressible flow are input of the acoustic model. However, an hybrid approach was developed because of two main reasons:

1. The computational aeroacoustics (CAA) requires a large computing resources. It has a series of applications only for academic cases because of expensive in time and allocated memory. The time consuming is in contrast with the industrial requirements of good solution in minimum time. In fact, all methods, that are included inside the CAA definition, are based on a simulation of noise source, acoustic propagation through a complex and not uniform flow, and a sound radiation in far-field hypothesis. Unsteady flow simulations, like Direct Numerical Simulation (DNS) or Large Eddy Simulation (LES), allow to answer the necessity of noise generation prediction; however they are not available for all types of noise sources. All mechanisms of turbulence noise generation and propagation, in previous chapter described, can be developed by solving Navier-Stokes equations from the body surface while the far-field propagation is described with transport equations (for uniform and not turbulent flow, Ffowcs Williams-Hawking equation is used). The length scale is too large in order to be easily managed: the turbulent eddies that are noise sources have small length and high energy, while acoustic waves are characterized by relatively high wavelength but small energy. For this reason the mesh must be very thin to obtain accurate results.

2. The noise developed by sharp airfoil-like body can be studied introducing other analytical theories. The pressure field on the body surface is the results of Reynolds Average Navier-Stokes equations. RANS simulations require less computational resources rather than CAA approach. This allows to reduce the computational time thanks to a larger mesh that must reproduce only the fluid dynamics phenomena around the body. Turbulent models have to be discussed,too. The choice of turbulent model associated to RANS equations is not simple because it affects the acoustic results.

2.1 Euler equations

Eulerian equations are a set of fluid dynamic equations governing the adiabatic and inviscid flow. They express the principles of mass, momentum and energy conservation. Eulerian model describes also not linear waves like shocks, compression or expansion. In many applications, the energy conservation equation can be substituted by the conservation of entropy. Considering a two dimensional domain, Eulerian equation can be written as:

$$\frac{\partial \rho}{\partial t} + \frac{\partial}{\partial x_j}(\rho u_j) = 0; \tag{2.1}$$

$$\frac{\partial \rho u_j}{\partial t} + u_i \frac{\partial \rho u_j}{\partial x_i} = -\frac{\partial p}{\partial x_j}; \tag{2.2}$$

$$\frac{\partial E_n}{\partial t} + u_j \frac{\partial E_n}{\partial x_j} = 0; \tag{2.3}$$

where ρ is the density, p the pressure and E_n the total energy per volume unit. The state equation, define the relationship between energy, pressure and velocity, which generic components are u_j, according to a certain reference system. Thus,

$$E_n = \frac{p}{\gamma - 1} + \frac{1}{2}\rho(u_1 + u_2)^2. \tag{2.4}$$

2.2 Navier-Stokes equations

For some phenomena with diffusive effects such as heat transmission and viscous stress, Navier-Stokes equations are introduced. Newton's and Fourier's laws are necessary to close the set of equations. Hence,

$$\frac{\partial \rho}{\partial t} + \frac{\partial}{\partial x_j}(\rho u_j) = 0; \tag{2.5}$$

$$\frac{\partial \rho u_j}{\partial t} + \frac{\partial \rho u_i u_j}{\partial x_i} = -\frac{\partial p}{\partial x_j} + \frac{\tau_{ij}}{\partial x_j}; \tag{2.6}$$

$$\frac{\partial E_n}{\partial t} + \frac{\partial}{\partial x_i}(u_i(E_n + p)) = \frac{\partial}{\partial x_j}\left[u_i \tau_{ij} - q_j\right]. \tag{2.7}$$

The heat flux is obtained by Fourier law as

$$q_j = -\frac{\gamma}{\gamma - 1}\frac{\mu \mathbb{R}}{\mathrm{Pr}}\frac{\partial T}{\partial x_j} \tag{2.8}$$

in which Pr is the Prandtl number, μ is the dynamic viscosity, γ is the specific heat ratio and $\mathbb{R}$ is the specific ideal gas constant for the air.

The component of shear stress tensor τ_{ij} are obtained with Boussinesq theory as

$$\tau_{ij} = 2\mu\left[S_{ij} + \frac{1}{3}\frac{\partial u_j}{\partial x_j}\delta_{ij}\right]. \tag{2.9}$$

The strain rate tensor is given by

$$S_{ij} = \frac{1}{2}\left(\frac{\partial u_i}{\partial x_j} + \frac{\partial u_j}{\partial x_i}\right). \tag{2.10}$$

2.3 Reynolds Averaged Navier-Stokes equations

RANS equations are time-averaged equations that come out from decomposition of all quantities as sum of the average values and the turbulent fluctuations. The main idea is to introduce a mean average in time in Navier-Stokes equations to obtain a new set of partial differential equations. Mean propriety of fluid are unknown variables of the problem. The main limit of this approach consists into the description of not resolved scales from knowing the mean flow. Hence, the velocity is defined as

$$\mathbf{U} = \bar{\mathbf{U}} + \mathbf{u}';$$

where the term u', is the fluctuations which mean value $\bar{u'}$ is zero. However, $\bar{\mathbf{u}'^2}$ is not null by definition The eddy effects of all scales are hidden in the fluctuating component.

Using the law (2.3) in Navier-Stokes equations, it can be written:

$$\frac{\partial \rho \bar{U}_j}{\partial t} + \frac{\partial}{\partial x_j}\left(\rho \bar{U}_j \bar{U}_i + \rho \bar{u_i' u_j'}\right) = \frac{\partial \bar{p}}{\partial x_j} + \frac{\partial}{\partial x_j}\left[\mu\left(\frac{\partial \bar{U}_i}{\partial x_j} + \frac{\bar{U}_j}{\partial x_i}\right)\right]. \tag{2.11}$$

The term $\rho \bar{u_i' u_j'}$ is the Reynold stress in which the eddies introduce the effect of viscosity. The equation (2.11) is not closed; for this reason it is necessary to introduce a modeling Reynold stress. An example is given by Spalart-Allmaras model.

2.4 Spalart-Allmaras model

Spalart-Allmaras[24] model (SA) allows to solve the turbulence flow field by introducing only one transport equation of modified turbulent viscosity. However, its solution is adapted for fully turbulent flows and applicable for both compressible and uncompressible fluids. The model has local solution. Thus, the local prediction does not depend on the solution computed in near points. The first proposed model had many problems with under-resolved meshes and it shows unphysical transient configuration with wrong results. In other cases, the modified viscosity $\tilde{\nu}$ assumes negative values that are not physically correct. The modified model was introduced in ref. [25] in order to solve these problems. The compressible turbulent transport equation was obtained by combining the classical Spalart-Allmaras model with the mass conservation law. Hence, it is proposed

$$\begin{aligned}&\frac{\partial \rho \tilde{\nu}}{\partial t} + \frac{\partial}{\partial x_j}\left(\rho u_j \tilde{\nu}\right) = \\ &\rho(P - D) + \rho f_{t1} u'^2 + \frac{1}{\sigma_{SA}}\frac{\partial}{\partial x_j}\left[\rho(\nu + \tilde{\nu})\frac{\partial \tilde{\nu}}{\partial x_j}\right] + \rho\frac{c_{b2}}{\sigma_{SA}}\frac{\partial \tilde{\nu}}{\partial x_k}\frac{\partial \tilde{\nu}}{\partial x_k} + \frac{1}{\sigma_{SA}}(\nu + \tilde{\nu})\frac{\partial \rho}{\partial x_k}\frac{\partial \tilde{\nu}}{\partial x_k};\end{aligned} \tag{2.12}$$

where P and D are functions of modified vorticity $\tilde{S}$ and modified viscosity $\tilde{\nu}$. The equation (2.12) has to be included in the following set of equations:

$$\frac{\partial \rho}{\partial t} + \frac{\partial}{\partial x_j}(\rho u_j) = 0; \tag{2.13}$$

$$\frac{\partial}{\partial t}(\rho u_j) + \frac{\partial}{\partial x_i}(\rho u_j u_i) = -\frac{\partial p}{\partial x_j} + \frac{\partial}{\partial x_j}(\tau_{ij} + \bar{\tau}_{ij}) \tag{2.14}$$

$$\frac{\partial E_n}{\partial t} + \frac{\partial}{\partial x_j}[u_j(E_n + p)] = \frac{\partial}{\partial x_j}[n_i(\tau_{ij} + \bar{\tau_{ij}}) - q_j]\,. \tag{2.15}$$

Reynold stresses are evaluates according Bussinesq assumption:

$$\nu_t = \tilde{\nu} f_{v1}, \quad f_{v1} = \frac{\chi^3}{\chi^3 + c_{v1}^3}, \quad \chi = \frac{\tilde{\nu}}{\nu}.$$

The turbulent stress tensor is defined as

$$\bar{\tau}_{ij} = 2\mu_t \left[S_{ij} - \frac{1}{3}\frac{\partial u_k}{\partial x_k}\delta_{ij} \right], \tag{2.16}$$

where the turbulent viscosity is given by $\mu_t = \rho\tilde{\nu} f_{v1}$; while τ_{ij} is the generic element of laminar stress matrix. Production P and destruction D contributions have explicit expression:

$$P = c_{b1}(1 - f_{t2})\tilde{S}\tilde{\nu} \quad D = c_{w1} f_w \left(\frac{\tilde{\nu}}{d}\right)^2,$$

where d is the distance to the closest wall. The modified vorticity $\tilde{S}$ is always positive in physical situations and more than $0.3S$. However, the Spalart-Allmaras correction is necessary to obtain a positive value of $\tilde{S}$ on the entire range of possible vorticity S. The function f_{v2} can assume negative values in a certain range of χ. Thus

$$\tilde{S} = \begin{cases} S + \bar{S} & \text{for} \bar{S} \geq -c_{v2} S \\ S + \frac{S(c_{v2}^2 S + c_{v3}\bar{S})}{(c_{v3} - 2c_{v2})S - \bar{S}} & \text{for} \bar{S} < -c_{v2} S, \end{cases} \tag{2.17}$$

where

$$\bar{S} = \frac{\tilde{\nu}}{k^2 d^2} f_{v2} \quad f_{v2} = 1 - \frac{\chi}{1 + \chi f_{v1}}.$$

The function

$$f_w = g\left[\frac{1 + c_{w3}^6}{g^6 + c_{w3}^6}\right]^{1/6}, \quad g = r + c_{w2}(r^6 - r) \quad r = min\left(\frac{\tilde{\nu}}{\tilde{S}k^2 d^2}, r_{lim}\right). \tag{2.18}$$

The trip and laminar suppression terms are introduced in equation (2.12) in order to force the transition point. However, the model is not appropriate to study the transitional flow as Spalart at Al. demonstrated. For this reason, trip and laminar suppression terms are not present in previous description.

Finally, the constants are:

$c_{b1} = 0.1355$	$\sigma_{SA} = 2/3$	$c_{b2} = 0.622$	$c_{v1} = 7.1$	$c_{v2} = 0.7$
$c_{v3} = 0.9$	$c_{w1} = c_{b1}/k^2$	$c_{w2} = 0.3$	$c_{w3} = 2$	$c_{t1} = 1$
$c_{t2} = 2$	$c_{t3} = 1.2$	$c_{t4} = 0.5$	$r_{lim} = 10$	k=0.41

2.5 Boundary conditions

Boundary and initial conditions have to be improved in order to regulate the calculus. The propagation of little disturbs in the fluid is imposed with the hypothesis of characteristic signals. For diffusive phenomena, the fluxes are forced through the surfaces that outline the finite elements of the mesh. In many cases, empirical corrections are introduced.

Because of wave propagation effects, the eulerian model presents boundary conditions depending on dimension and shape of computational domain. The Boundary conditions are imposed along the propagation lines. On the surface of the body is valid the principle of not permeation and tangent direction for the velocity.

In Navier-Stokes equations, diffusive terms are not negligible. At the wall, no-slip condition has to be imposed while energy diffusion depends on the wall characteristics.

For the Spalart-Allmaras model, the main purpose consists into imposing a correct boundary condition for the modified viscosity. Thus, on the solid surfaces are still valid not permeation and no-slip hypothesis, while the turbulent fluctuations are null because the flow speed is identically zero. As a direct consequence, the turbulent viscosity is zero, too. In the inlet, the turbulent viscosity has to be imposed. Generally, for fully turbulent flows, modified viscosity $\tilde{\nu}$ is between three and five times the kinematic viscosity.

Chapter 3

Global sensitivity analysis

The sensitivity analysis aims to identify how the uncertainty in the input parameters influences the uncertainty in the output of a numerical or empirical model. However, the numerical description is not a perfect representation of the physical phenomena. The introduction of several simplification assumptions is necessary to reproduce the real world but the scientific method is subjected to errors. The mathematical approximation and the accuracy of measurements are the main causes of error.
The sensitivity approach allows to study the model corroboration, which ensures the correctness of the model itself and it shows if the approach depends on a fragile assumption. However, all input quantities have a different effect on the output results; thus, drafting a hierarchy on quantities relevance is necessary to distinguish which parameters are negligible and which ones must be measured with a major accuracy, especially in the experimental tests. Sensitivity answers the question about which factor is most deserving of further analysis.

Sensitivity analysis brings to a model simplification that consists into identify some factors or compartments of the model can be fixed or modified in order to improve the general performance. Moreover, critical regions in the input quantities are underlined. This approach is important for system reliability.
In general, it is possible to note that high uncertainty in the input factors does not imply a low quality of the resulting model. In fact, only few inputs affects the output.

A possible approach for the sensitivity analysis is a local evaluation based on derivatives. The derivative $\partial Y_j/\partial X_i$ describes the effects of X_i input parameter on the Y_j output. Unfortunately, many problems occurs when complex model with many equations and non linear functions, is run. It is prohibitive to compute, in both analytical and numerical way, the derivatives. However, the derivative-based methods are not expensive in computational time because the model has to be executed few times in comparison with the extrapolated methods; while they are hard to be implemented in coding.
The sensitivity analysis of the pressure spectrum models is carried out by introducing a series of global factors that define the single contribution of the inputs on the model's output.

A Monte Carlo analysis is used to extrapolate random values for each input quantities.

The hypothesis of normal distribution is not necessary. The variance is arbitrary, while the mean values are fixed to the measured quantities that come from previous RANS simulations. A new acoustic simulation in which the inputs are a pseudo-random combination of all factors is run. For N combinations of factors, it is necessary to run N times the acoustic code.
In general, defining as α, β, γ the input quantities for which a normal distribution function $\mathcal{N}(\sigma, \bar{\alpha})$ is considered, a matrix of NxN terms with random combination of all quantities is computed. Thus,

$$\begin{bmatrix} \alpha_1 & \beta_1 & \gamma_1 & \dots & \zeta_1 \\ \alpha_2 & \beta_2 & \gamma_2 & \dots & \zeta_2 \\ \alpha_3 & \beta_3 & \gamma_3 & \dots & \zeta_3 \\ & & \vdots & & \\ \alpha_N & \beta_N & \gamma_N & ... & \zeta_N \end{bmatrix},$$

from which it is possible to obtain the output vector

$$\begin{bmatrix} Y_1 \\ Y_2 \\ Y_3 \\ \vdots \\ Y_N \end{bmatrix}.$$

3.1 Scatterplots definition

The scatterplot is a graph in which the outputs of a single model are plotted as function of the random input. Over the x axis is plotted the single input, while y axis contains the model output. This method introduces only a qualitative study about the influence of the generic input with only a visual depiction of the output. A scatterplot with a sort of uniform cloud of points over the entire range of input values is synonymous of small influence, rather than a factor for which the point distribution presents a stretched shape. An example is reported in Figure 3.1, in which it is represented the first step of sensitivity analysis for Goody's spectrum model. It is almost evident the strong dependence of the model from the friction coefficient c_f, for which the graph in Figure 3.1(b) appears to be elongated. On the other hand, the uncertainty on boundary thickness δ does not influences the model output. This conclusion can be obtained also using a global sensitivity approach. The scatterplots in the example were drawn fixing the same variance for the inputs. A normal distribution function is introduced. However, the hypothesis of normal distribution does not influences the general behavior of the graphs.

3.2 Global sensitivity factors

3.2.1 First-order index

The global sensitivity factors are defined as the ratio of two variances calculated for the model in two different operating conditions by fixing one or more input parameters. How-

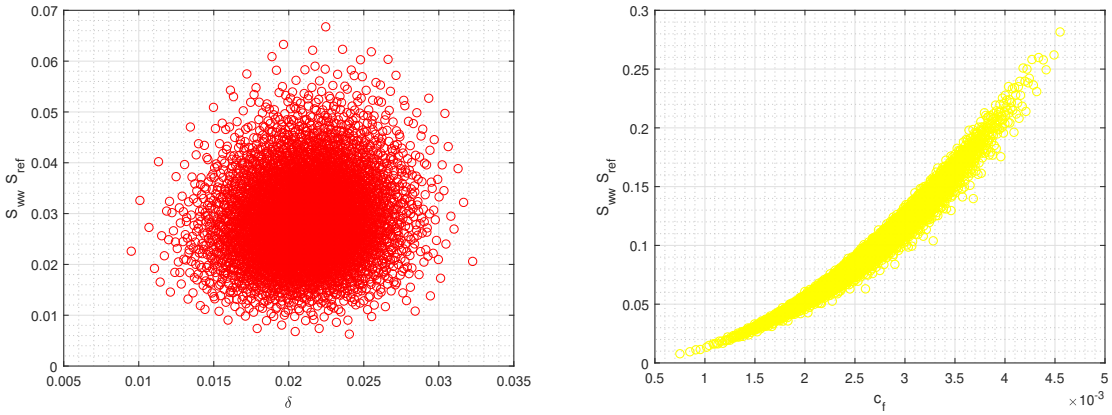

(a) Scatterplot of δ. (b) Scatterplot of c_f.

Figure 3.1: Scatterplot analysis for Goody model

ever, for more parameters, it is assumed they are independent. This assumption is not always verified: in many application, in fact, inputs can be related by a correlation dependence.

The choice of experimental design depends on the expected way a single parameter uncertainty influences the output. For example, if Y is a function of several quantities X_i that are assumed independent and with a uniform distribution in $[0, 1]$ interval, a linear model can be used and it consists into a linear approximation of the outputs. Hence, in other terms

$$Y = b_0 + \sum_{i=1}^{k} b_i X_i \tag{3.1}$$

where k is the number of input parameters. The constants b_i are unknown at the beginning of the analysis. For N simulations, where $N > k + 1$, the linear system to solve can be written as:

$$\begin{bmatrix} 1 & x_{11} & \dots & x_{1k} \\ 1 & x_{21} & \dots & x_{2k} \\ & & \vdots & \\ 1 & x_{N1} & \dots & x_{Nk} \end{bmatrix} \begin{pmatrix} b_0 \\ b_1 \\ \vdots \\ b_k \end{pmatrix} = \begin{pmatrix} y_1 \\ y_2 \\ \vdots \\ y_N \end{pmatrix} \tag{3.2}$$

Although the system is overdetermined, it is always possible to solve the linear problem just considering the least square matrix. The main advantage consists into a relatively low cost due to a small number of parameters to compute. However, the linear model can be applied only for simple problems for which the linear dependence is a plausible assumption. In other conditions, for example not linear systems, this method does not bring useful information. A regression model, such as the linear model, are designed to compute also the standardized regression coefficients like $\hat{\beta}_i = b_i \sigma_i / \sigma_Y$, where σ_i is the variance of the i-th input quantity and σ_Y, the variance of the model output. $\hat{\beta}$ indexes are often used for sensitivity analysis: high $\hat{\beta}$ value means high parameter influence. If

the starting model is linear, it is possible to demonstrate that

$$\sum_{i=1}^{k} \hat{\beta}_i^{\,2} = 1. \tag{3.3}$$

For not linear model, the formula in equation (3.3) is not more valid; for this reason it is necessary to introduce the conditional variance.

It is assumed X_i the i-th input factor. If X_i is fixed as a constant x_i^*, the resulting variance of Y, calculated over all X except for X_i, is defined as conditional variance and it is written as $V_{X_i}(Y|X_i = x_i^*)$. It is reasonable to think that the conditioned variance for a fixed input is less than the total variance $V(Y)$ due to the elimination of uncertainty source. For this reason, V_{X_i} is a good approximation of the relative importance of X_i in the entire model.

Two main difficulties are evident: the sensitivity depends on the fixed values imposed; thus the choice of x_i^* influences V_{X_i}; on the other hand, the conditional variance could assume, in many cases, a greater value than $V(Y)$ and it does not give any more information about model behavior. The average value, calculated over all possible x_i^* allows to remove the dependence of $V_{X_i}(Y|X_i = x_i^*)$ on x_i^*. The notation $E_{X_i}(V_{X_i})$ indicates the mean value of variances so calculated.
It is possible to demonstrate

$$E_{X_i}(V_{X_1}(Y|X_i)) + V_{X_i}(E_{X_i}(Y|X_i)) = V(Y). \tag{3.4}$$

Since (3.4), $V_{X_i}(E_{X_i}(Y|X_i)) \leq V(Y)$ and the first-order sensitivity index of X_i on Y is defined as:

$$S_i = \frac{V_{X_i}(E_{X_i}(Y|X_i))}{V(Y)}. \tag{3.5}$$

The high value of sensitivity index implies an influential input variable. For single parameter function, the global sensitivity factor S_1 assume unit value.

3.2.2 Nonadditive models and second-order index

A model is defined as additive model if it is possible to separate the effects of input variables in a variance decomposition framework[26]. In other terms, the output variance is completely ranged and each input contributes in part to the output variance. Thus, it is valid

$$\sum_{i=1}^{k} S_i = 1.$$

For non additive models, the first-order indexes are not enough to reconstruct the all uncertainty contribution; however, they are sufficient precise to describe the single

parameter contribution. The sum of first-order indexes is minor than one. In symbols

$$\sum_{i=1}^{k} S_i \leq 1.$$

The second-order index is defined by introducing two fixed values for two different input quantities. It is possible to compute the variance

$$V_{X_{ij}}(E_{X_{ij}}(Y|X_i, X_j)) = V_i + V_j + V_{ij} \tag{3.6}$$

where V_i, V_j and V_{ij} define the variances for average of output values and for i-th or j-th fixed input variables. Moreover, the term V_{ij} is the interaction factor between X_i and X_j and it describes the way how the response of Y depends on both X_i and X_j combined. From equation (3.6), it is possible to write

$$\frac{V_{X_{ij}}(E_{X_{ij}}(Y|X_i, X_j))}{V(Y)} = S_i + S_j + S_{ij}. \tag{3.7}$$

The term S_{ij} is the second-order sensitivity factor.

By fixing three or more input variables it is possible to compute a third-order index and so on. The main purpose is to reconstruct the entire spectrum of the variance of Y, that depends not only on the single input, but also on their interaction. For k factors, the sum of all order indexes are equal to one. In fact,

$$\sum_{i=1}^{k} S_i + \sum_{i=1, j>1}^{k} S_{ij} + \sum_{i=1, j>1, l>j}^{k} S_{ijl} + S_{123\ldots k} = 1. \tag{3.8}$$

The main problem consists into the great number of elements for the series in equation (3.8), equal to $2^k - 1$. Consequentially, this approach is not helpful in many circumstances.

The total effect term has to be introduced. It describes the total contribution on model behavior of the single input variable. In other terms, it is the sum of global sensitivity factor of upper orders that were obtained by fixing X_i value:

$$S_{T_i} = \left(1 - \frac{V_{X_i}(E_{X_i}(Y|X_i))}{V(Y)}\right) = S_i + \sum_{j=2}^{k} S_{ij} + \ldots + S_{ijk}. \tag{3.9}$$

For only three input variables, the total effect term is

$$S_{T_1} = S_1 + S_{12} + S_{13} + S_{123}.$$

This demonstrates the total indexes are always bigger than the first order factors and the sum of total indexes is higher than one. The values of global indexes slightly depends on the number of points. By increasing the number of random input points, the global factors slightly variate but the order magnitude remains constant.

3.2.3 Pseudo-random sampling with low discrepancy sequences

The first step for sensitivity approach consists into sampling the input variables. Generally, it is possible to improve a random generation method for an uniform distribution inside [0,1] interval. It is always possible to reconstruct the generic interval $[a, b]$, on which the quantity distribution is known. However, very elaborate sampling methods can be improved in order to describe all possible combinations for the inputs. Multivariate stratified sampling or Latin hypercube sampling are valid alternatives to the random point generation. They are complex methods to improve in numerical code (see ref. [26]) but they allow to gesture a large number of variables.

Mote Carlo method was chosen because of its simple codification and small number of variables to be analyzed. However, a simple Monte Carlo method improves a series of clusters and gaps that introduce areas of different statistical importance. The cluster is defined as an area with a large number of close points and the model function is studied in details; while, where a gap occurs, the model has no enough points for a statistical analysis. As direct consequence, a simple random method requires a large number of points in order to reduce the inconsistent intervals. Furthermore, discrepancies tends to accumulate for a k-series of variables. For this reason a pseudo-random sampling, also known as low discrepancy method, was chosen.

The pseudo-random sampling is improved through an algorithm that chooses a new point enough away from the previous selected point. The term pseudo-random is used to define a not uniform distribution that is predictable with an algorithm. Halton or Sobol sequences can be used for the present purpose. The effect of Halton distribution is shown in Figure 3.2, in which a two dimensional space is sampled against a complete random method. It is evident the pseudo-random sampling allows to cover the entire domain without gaps or clusters. Increasing the number of points, the two graphs coincide.

3.2.4 Saltelli's Monte-Carlo based numerical sensitivity approach

Saltelli's method was proposed to compute sensitivity indexes by Monte Carlo random distribution[27, 26]. The following approach allows to improve a numerical method based only on model function evaluations without theoretical limits on the input number.

The first step consists into creation a matrix of random (or pseudo-random) values of Nx2k dimension, where k is the number of input quantities and N is the number of points chosen for the simulation. From this first matrix, it is possible to introduce the matrices A and B, by extrapolating the first and second k columns, as reported in formulas (3.10) and (3.11). Thus,

$$A = \begin{bmatrix} x_1^{(1)} & x_2^{(1)} & x_3^{(1)} & \dots & x_k^{(1)} \\ x_1^{(2)} & x_2^{(2)} & x_3^{(2)} & \dots & x_k^{(2)} \\ x_1^{(3)} & x_2^{(3)} & x_3^{(3)} & \dots & x_k^{(3)} \\ & & \vdots & & \\ x_1^{(N)} & x_2^{(N)} & x_3^{(N)} & \dots & x_k^{(N)} \end{bmatrix}; \tag{3.10}$$

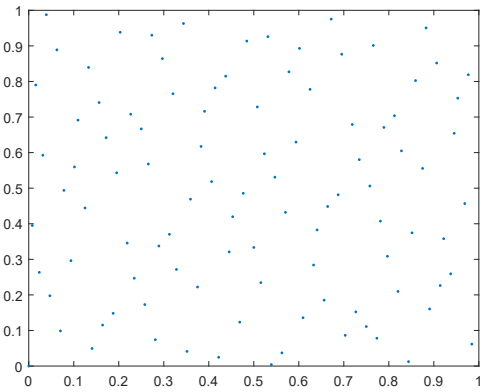

(a) Scatterplot for Halton sequence and N=100.

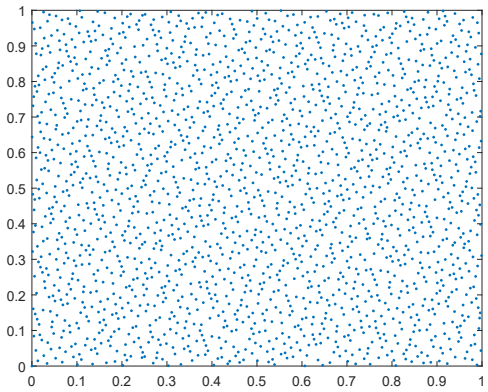

(b) Scatterplot for Halton sequence and N=2000.

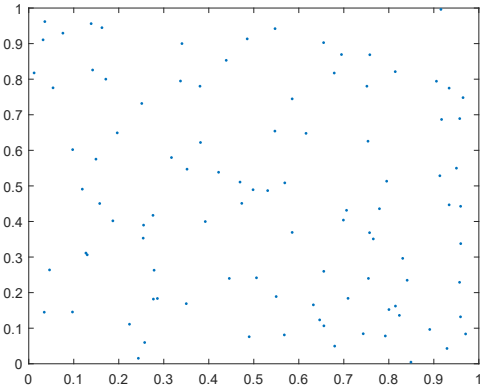

(c) Scatterplot for random sequence and N=100.

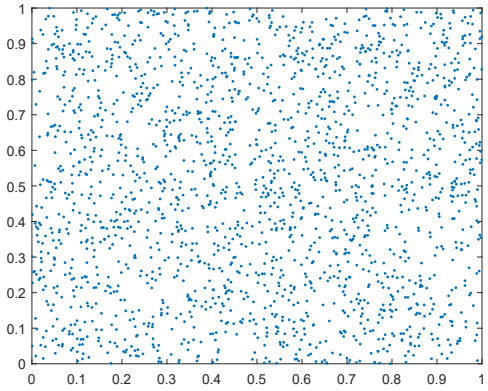

(d) Scatterplot for random sequence and N=2000.

Figure 3.2: Comparison between Halton pseudo-random sampling method and a Monte Carlo method.

and

$$B = \begin{bmatrix} x_{k+1}^{(1)} & x_{k+2}^{(1)} & x_{k+3}^{(1)} & \dots & x_{2k}^{(1)} \\ x_{k+1}^{(2)} & x_{k+2}^{(2)} & x_{k+3}^{(2)} & \dots & x_{2k}^{(2)} \\ x_{k+1}^{(3)} & x_{k+2}^{(3)} & x_{k+3}^{(3)} & \dots & x_{2k}^{(3)} \\ & & \vdots & & \\ x_{k+1}^{(N)} & x_{k+2}^{(N)} & x_{k+3}^{(N)} & \dots & x_{2k}^{(N)} \end{bmatrix}. \tag{3.11}$$

The matrix C_i, is obtained from B in which the i-th column is taken from A:

$$C_i = \begin{bmatrix} x_{k+1}^{(1)} & x_{k+2}^{(1)} & \dots & x_{i}^{(1)} & \dots & x_{2k}^{(1)} \\ x_{k+1}^{(2)} & x_{k+2}^{(2)} & \dots & x_{i}^{(2)} & \dots & x_{2k}^{(2)} \\ x_{k+1}^{(3)} & x_{k+2}^{(3)} & \dots & x_{i}^{(3)} & \dots & x_{2k}^{(3)} \\ & & \vdots & & & \\ x_{k+1}^{(N)} & x_{k+2}^{(N)} & \dots & x_{i}^{(N)} & \dots & x_{2k}^{(N)} \end{bmatrix}. \tag{3.12}$$

The model is applied by imposing as input quantities each row elements of previous

matrices. Hence, the output vectors are:

$$y_a = f(A) \quad y_b = f(B) \quad y_{c_i} = f(C_i)$$

The first order sensitivity indexes are so computed:

$$S_i = \frac{1/N y_a \cdot y_{c_i} - f_0^2}{1/N y_a \cdot y_a - f_0^2} = \frac{1/N \sum_{i=1}^{N} y_a^{(i)} y_{c_i}^{(i)} - f_0^2}{1/N \sum_{i=1}^{N} y_a^{(i)} y_a^{(i)} - f_0^2}, \tag{3.13}$$

where

$$f_0^2 = \left(\frac{1}{N} \sum_{i=1}^{N} y_a^{(i)} \right)^2 .$$

In a similar way, it is introduced the total effect index as:

$$S_{T_i} = 1 - \frac{1/N y_b \cdot y_{c_i} - f_0^2}{1/N y_a \cdot y_a - f_0^2} = \frac{1/N \sum_{i=1}^{N} y_b^{(i)} y_{c_i}^{(i)} - f_0^2}{1/N \sum_{i=1}^{N} y_a^{(i)} y_a^{(i)} - f_0^2}, \tag{3.14}$$

The total number of model evaluation is $N(k+2)$, that is less than N^2 runs necessary for the simple Monte Carlo method.

Part II

Numerical Setup and Results

Chapter 4

RANS solution

In order to compute the input quantities of Amiet's model, Reynold Averaged Navier-Stokes (RANS) equations are solved, with a Spalart-Allmaras turbulent model[28]. The velocity field around the airfoil is obtained by imposing the initial condition as described in Chapter 2. The RANS equations are written in dimensionless form.
Dimensionless approach allows to adapt the solution for different body and experimental conditions by modifying the reference quantities and imposing the upstream velocity or the chord dimension. The main advantage of dimensionless approach consists into the possibility to describe the fluid field around the body for a series of experimental condition with fixed Reynolds and Mach number. However, the reference quantities are necessary to convert the dimensionless solution into dimensional quantitie to substitute in Amiet's acoustic formula. The reference length is the chord, used also to scale the boundary thickness; while the stagnation pressure and stagnation temperature are assumed constant and set as reference values. The static quantities, sound speed and fluid reference viscosity are calculated as following described. The gas used for all simulation is air, approximated to ideal gas, thus the perfect gas state equation is applied. The specific heat ratio is $\gamma = 1.4$. The code needs also the Prandtl number for both laminar and turbulent flow. Thus,

$$Pr = 0.72 \quad Pr_{tr} = 0.9,$$

The airfoil surface is supposed to be adiabatic in all simulations; hence the thermal effect is negligible. For the initialization, the Mach is imposed in inlet boundary, equal to $M = 0.16$. The fluid is almost uncompressible. High Reynolds number is chosen to simulate a typical airplane flying configuration. Simulations are launched at different Reynolds and various angles of attack. However, zero incidence is mainly studied because of the large experimental data in literature.

For Spalart-Allmaras model, was imposed the inizial value

$$\frac{\rho\tilde{\nu}}{\rho\nu} = 3,$$

as initial condition. The governing equations are discretised according to the method of lines: a discontinuous Galerkin finite element method is used for the spatial discretisation while time integration is performed by the implicit first order Euler scheme. For this

reason, the inviscid solution is leaded out and employed as initial condition for the Spalart-Allmaras simulation.

4.0.1 Reference condition estimation

The Reynolds number and Mach are fixed. Knowing the airspeed U_∞ and density ρ_∞ in experimental conditions that are reported in the reference papers (see ref. [6, 7]), it is possible to define all reference quantities.

Hence,

$$c_0 = MU_\infty \quad T_\infty = c_0^2/(\gamma R)$$

. The pressure is calculated as $p_\infty = RT_\infty\rho_\infty$.
Thus, it is possible to write

$$T_{ref} = \left(1 + \frac{\gamma - 1}{2}M^2\right) T_\infty, \tag{4.1}$$

$$p_{ref} = \left(1 + \frac{\gamma - 1}{2}M^2\right)^{\frac{\gamma}{\gamma-1}} p_\infty, \tag{4.2}$$

$$\rho_{ref} = \frac{p_{ref}}{RT_{ref}}. \tag{4.3}$$

The reference speed is defined as

$$U_{ref} = \sqrt{RT_{ref}}. \tag{4.4}$$

Finally, the viscosity is obtained from the Reynolds number definition:

$$\mu_{ref} = \frac{U_\infty \rho_{ref} c}{\mathrm{Re}}. \tag{4.5}$$

4.1 Mesh generation

Two dimensional mesh is generated using Gmesh software.
NACA0012 airfoil points are imported and a computational domain is created. The body is fixed in the origin of the reference system while the angle of incidence is modified rotating the upstream flow. The inlet boundary conditions are critical to be imposed. In fact, it is necessary to guarantee that the flow enters the domain in the inlet boundary area and it does not exit. If the boundary conditions are not correctly implemented, disturbance waves can propagate in the domain due to errors generated by the code. Thus, the shape of the domain is shown in Figure 4.1. The lateral sides have 20° inclination. In this case, it is possible to implement also high angle of incidence without modify the mesh. The outlet boundary is univocal defined.

Unstructured mesh with quad elements is used. The elements have higher dimension in the external area rather than near the body surface, in order to reduce the total number of mesh elements and, consequentially, the computational cost. Indeed the external flow is not affected by the presence of the body and its behavior is assimilated to the

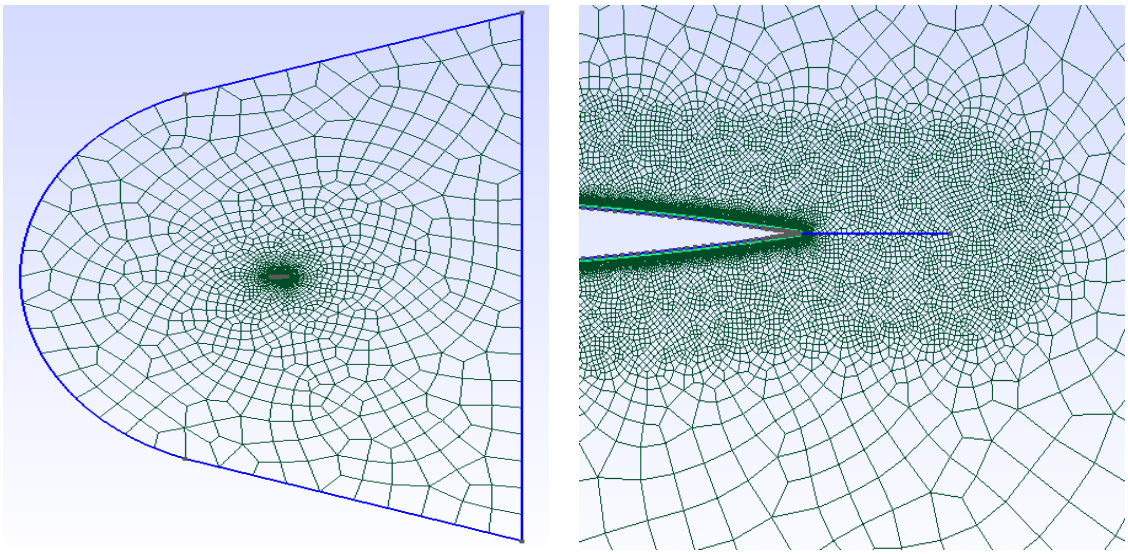

(a) Entire overview of the mesh. (b) Details of the mesh around the body.

Figure 4.1: Mesh of the computational domain.

undisturbed flow. Big compact mesh does not affect the solution. The downstream the profile is created a mesh region with small elements along the chordwise direction. The elements are immersed in the wake region and they allow to describe the wake evolution immediately downstream the body where high resolution is required.

The boundary layer is characterized by a structured quad mesh. It consists into a series of rectangular elements with increasing dimension by moving away from the airfoil surface. Close to the body surface, the rectangular mesh is necessary in order to correctly solve the the boundary layer. The height of boundary elements is an index of the accuracy of boundary solution and it corresponds to the minimum distance from the wall the flow characteristics are computed. The mesh improved has minimum dimensionless height equal to $5\,10^{-5}$ and it is enough accurate to compute the inner layer. The extrapolation of the velocity field on the body surface is obtained by modifying the RANS code that saves the airspeed in the quadrature points closest to the extrapolation line.

In Figure 4.1 is reported the entire grid. Obviously, the dimension of the computational domain is chosen to avoid possible interaction between the airfoil and the external domain border. The distance of twenty times chord was chosen. The shape of the external field allows to correctly implement the inlet boundary condition also for high angle of attack. The Figure 4.2 shows the detailed grid in proximity of the wall. Quadrature points of the mesh are used to extrapolate the airspeed and to compute the boundary quantities by definition.

The same steps are followed to build the computational grid for DU96-W-180 profile. The points of the geometry are imported in Gmesh software and the external domain is created with the same characteristic previous described.

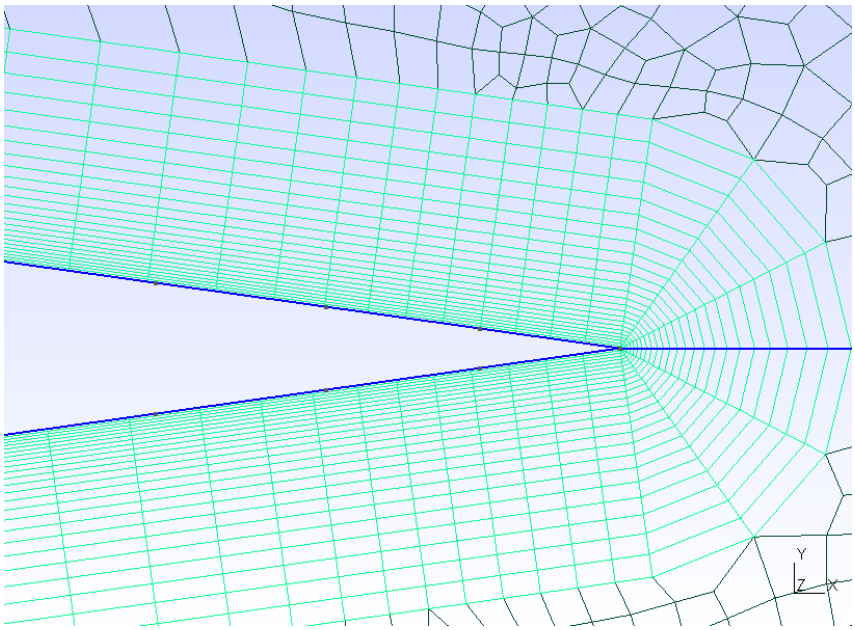

Figure 4.2: Details of the boundary layer mesh.

4.2 Pressure coefficient and speed profile

4.2.1 NACA0012 airfoil

The first profile analyzed is NACA0012 airfoil. In following cases, the Mach number is fixed at 0.16 and Reynolds is $1.5\,10^6$. The pressure coefficient and the boundary layer profile are compared with the theoretical trend in order to validate the RANS simulations. For zero angle of attack the c_p coefficient presents a symmetric distribution according to the theoretical prediction for a symmetric airfoil, as shown in Figure 4.3. The same graph is obtained with Xfoil analysis that is plotted in the same figure and it is considered as reference in the following description. The two curves perfectly coincide almost along the entire chord and this demonstrates the simulation has a good agreement with the expected results. The same analysis was repeated also for different angle of attack. Obviously, the symmetrical property is lost and the c_p reaches smaller values on the suction side. The Figure 4.4 compares the c_p coefficient obtained with Xfoil simulation and the pressure distribution of RANS solution at incident $\alpha = 6°$ and $Re = 1.5\,10^6$. The both curves show a maximum value equal to one in correspondence of stagnation point very close to the leading edge. In the central part of the airfoil the pressure distribution is almost identical for both series of data. The minimum value of c_p is reached at 2% of the chord where the airspeed assumes the maximum value. However, the Xfoil solution exhibit a smaller value rather than RANS solution. And it implies a local higher velocity for the reference case.

The friction coefficient is plotted as function of the dimensionless chord position. It is the main input parameter of the pressure spectra models and it is reasonable comparing the RANS results with the Xfoils reference plot. In Figure 4.5, the friction coefficient is plotted at various angle of attack. For zero incidence, the distribution of friction is

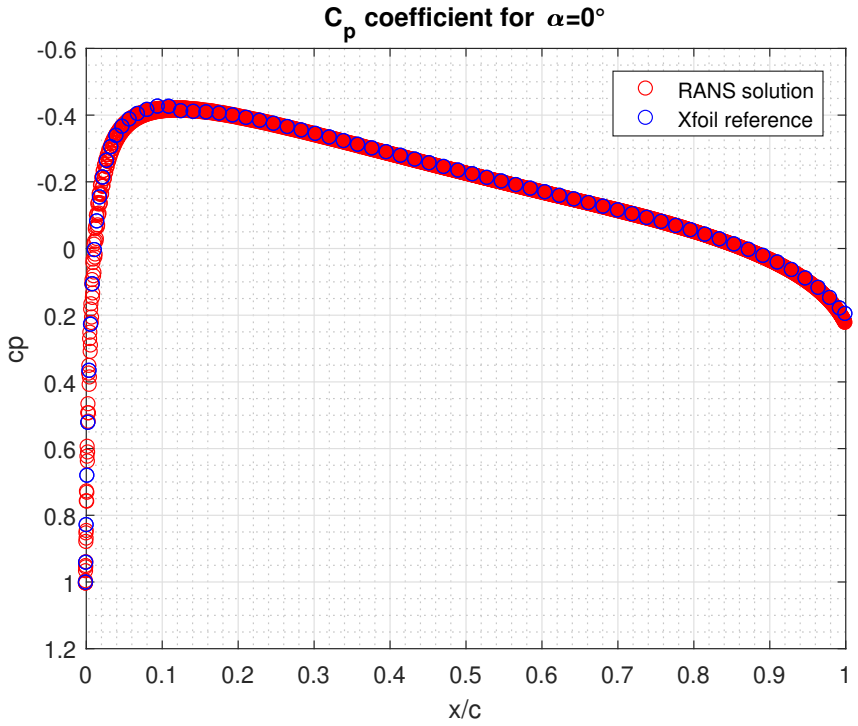

Figure 4.3: Pressure coefficient distribution around NACA0012 airfoil at 0° of incidence.

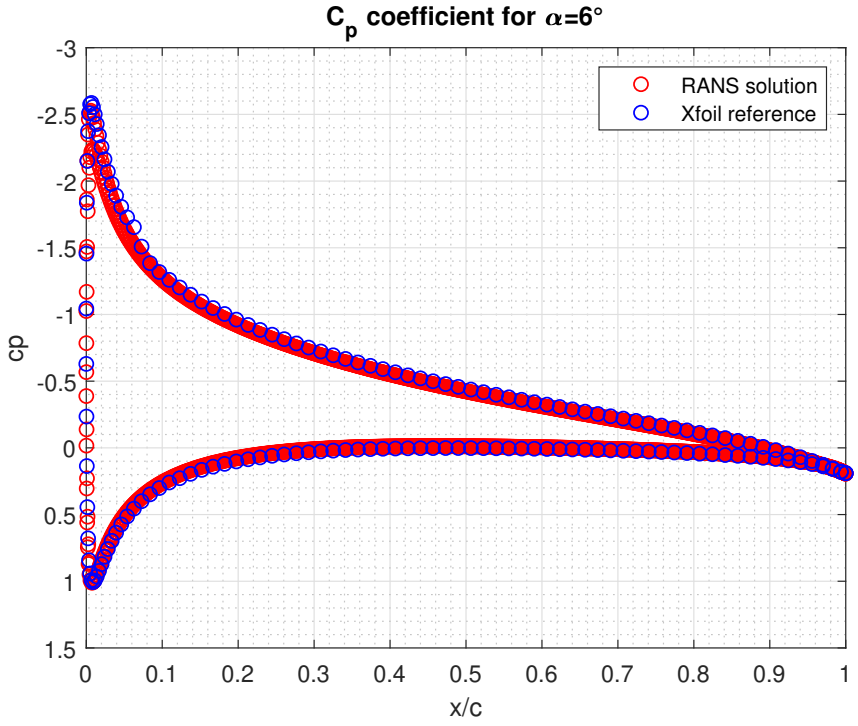

Figure 4.4: Pressure coefficient distribution around NACA0012 airfoil at 6° of incidence.

symmetric and the difference between theoretical and predicted graph is evident near the trailing edge that is the area of interest for the present work. The Xfoil solution shows two peaks near the leading edge that the numerical simulation does not predict. The two curves move closer in the central zone until to almost coincide. For not zero angle of attack, the symmetrical property is lost and the curves for the suction and the pressure sides are perfectly discernible. However, the proposed cases for 4° ad 6° incidence, show a predicted c_f over the suction side that perfectly overlies the reference curve for the major part of the chord, especially close the trailing edge. The main differences are visible for 6° incidence but they are almost negligible for the acoustic purpose because they involve the leading edge area. In conclusion, the RANS solution is accurate in the zone of interest and the pressure spectra models can be correctly applied. The Xfoil reference shows two peaks. For the pressure side the plot appears almost flat and the curves coincide all over the entire chord, excepted near the leading edge.

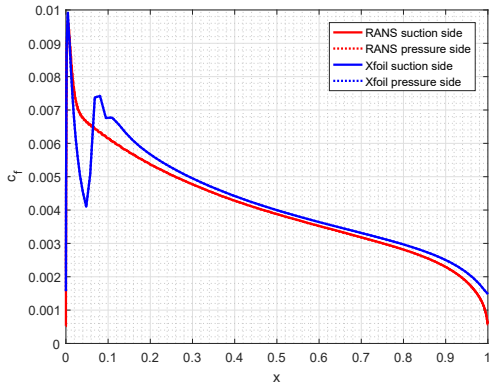

(a) 0° incidence and Re=1.5 10^6.

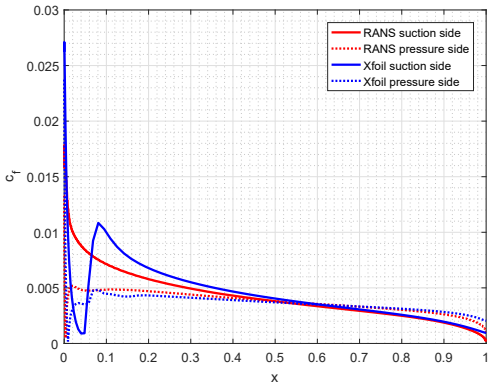

(b) 4° incidence and Re=1.5 10^6.

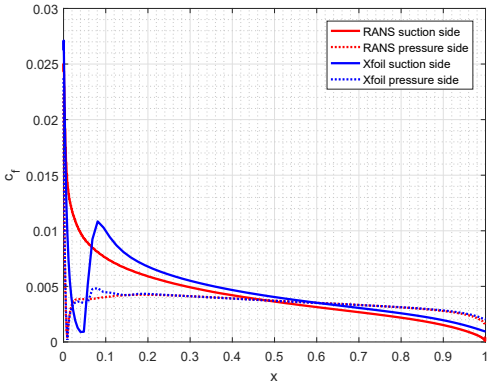

(c) 6° incidence and Re=1.5 10^6.

Figure 4.5: Comparison of friction coefficient at Re=1.5 10^6 and at various angle of attack.

For further information, the contour lines for Mach number are reported in Figure 4.6 for the 0° and 6° incidence. Obviously, in proximity of the body surface the airspeed comes from zero to the external velocity due to the boundary layer. The velocity field assumes a symmetric configuration for zero angle of attack. Increasing the incidence, the flow field

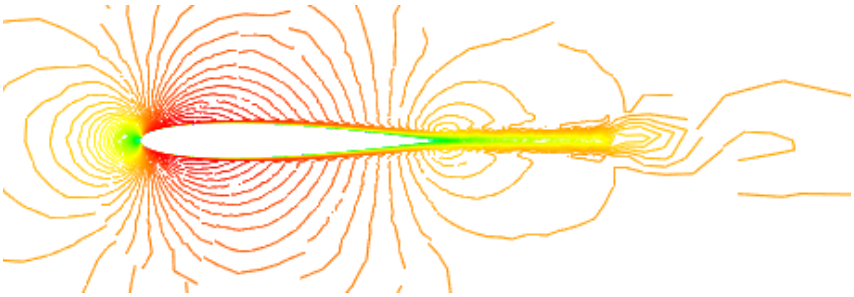

(a) 0° incidence and Re=1.5 10^6.

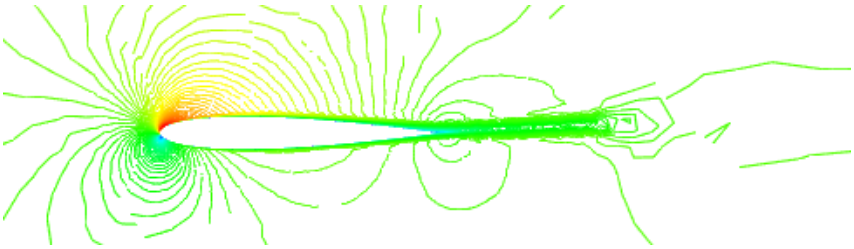

(b) 6° incidence and Re=1.5 10^6.

Figure 4.6: Comparison of the Mach field around the NACA0012 profile at different angles of attack.

around the body lost his symmetry. The stagnation point is evident near the leading edge on the pressure side; while the gas accelerates in the red zone (Figure 4.6(b)). The wake is evident behind the body and it theoretically propagates to the infinity downstream. However, the simulation was stopped after reached a stationary solution for which the derivative in time of airspeed is about 10^{-5}. The main limit, but at the same time the main quality of the Amiet's theory, is the possibility to discuss the acoustic emission by a stationary solution that provides the mean quantities for turbulent flow, without the necessity of a LES or DNS simulations.
The boundary thickness is shown in Figure 4.6, where it is evident for the six degrees configuration an higher value at the suction side near the trailing edge.

The quantity $\rho\tilde{\nu}$ is drawn in Figure 4.7, that shows the general trend of the turbulence viscosity in the boundary layer. It is evident the position of flow transition from laminar to turbulent, in proximity of the leading edge. However, the flow can be considered as completely turbulent. The transitional chord position is used to improve a forced transition solution in Xfoil software in order to calculate the reference value for displacement thickness and momentum thickness. The transition take place at about 0.1 times the chord but it depends on the angle of attack. The two graphs present an important difference near the trailing edge and the asymmetry of the field is almost evident. The red zone corresponds to high turbulent area and obviously it is the central part of the wake field. The external field is characterized by an uniform turbulence that was imposed as initial condition.

The boundary layer speed profile is obtained by extrapolation of the two mean components of the velocity, $\bar{u}$ and $\bar{v}$, along the normal direction on the body surface that coincide

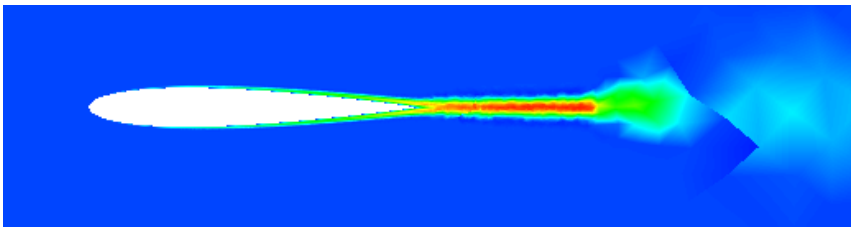

(a) 0° incidence and Re=1.5 10^6.

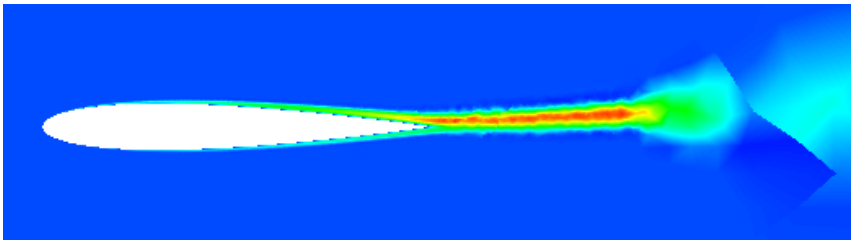

(b) 6° incidence and Re=1.5 10^6.

Figure 4.7: Comparison of the field $\rho\tilde{\nu}$ around the NACA0012 profile at different angles of attack.

to the line of the boundary mesh (see Fig. 4.2) However, increasing the distance from the wall, the number of points that provide the flow velocity, lowers because of unstructured mesh. In fact, the code is able to get the mesh nodes nearest a certain direction imposed but not to get internal point of the mesh elements. For this reason, the velocity profile, as following discussed, is almost perfectly predicted with high number of points near the body surface. The viscous sublayer with its linear law and the logarithmic zone are well described.

The position of boundary layer extrapolation is now discussed. The Amiet's theory does not specify the position in which correspondence the pressure spectrum has to be computed. However, the sensitivity analysis helps to find how the position parameter, hidden inside the boundary quantities, influences the acoustic phenomena and how much the position "in proximity" of the trailing edge is important. The noise emission for different positions is compared for acoustic purpose. However, to capture the trailing edge noise is important to fix the position as close as possible to the trailing edge. In RANS simulation is quite prohibitive to get 99% of the chord because the flux is influenced by the wake and numerical results could be affected by errors. However, $x/c = 0.95$ allows to limit this problem. The boundary quantities are so calculated at 80%, 90%, 95% and 98% of the chord. In Figure 4.8 the extrapolated boundary profiles and the theoretical one are compared for different position along the chordwise direction. It is shown the curves have a good agreement with the theoretical formulation for all position studied. The temperature profile is omitted because it is useless for acoustic purpose.

The velocity outside the boundary layer grows by stepping away from the surface. Thus, it is impossible to define which velocity limits the boundary layer, like it happens for a flat plate. For this reason, it is necessary to introduce a conventional external

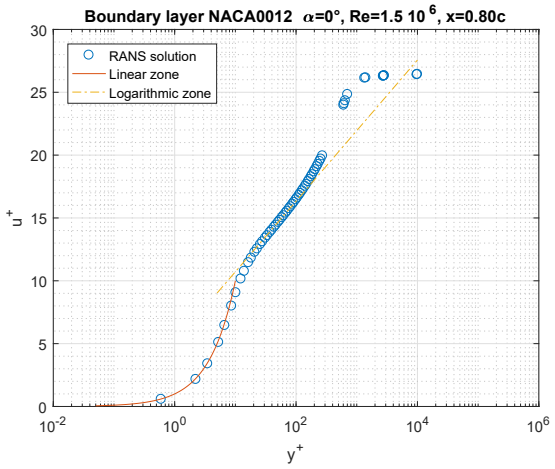

(a) Zero degree incidence at Re=1.5 10^6 and 80% of the chord.

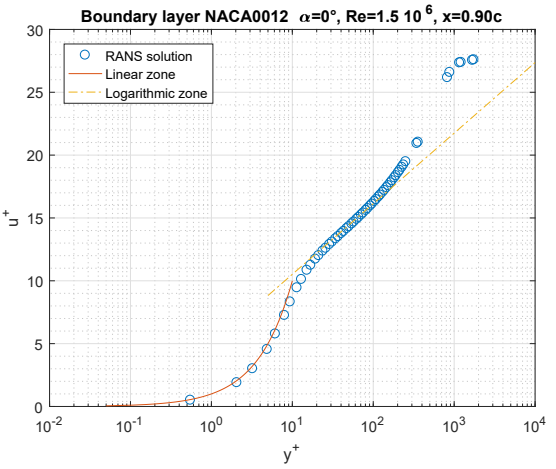

(b) Zero degree incidence at Re=1.5 10^6 and 90% of the chord.

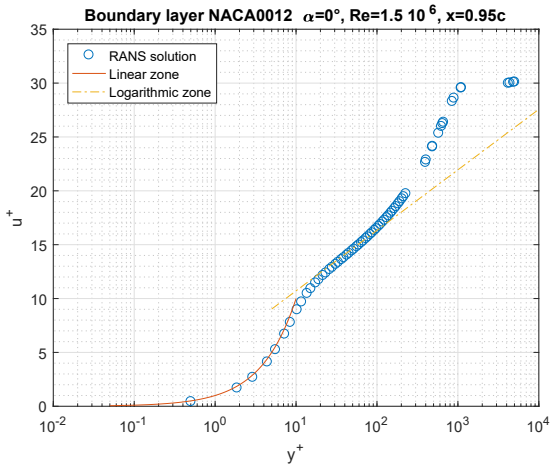

(c) Zero degree incidence at Re=1.5 10^6 and 95% of the chord.

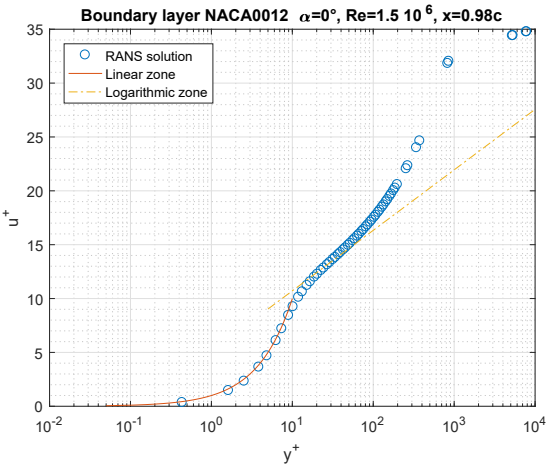

(d) Zero degree incidence at Re=1.5 10^6 and 98% of the chord.

Figure 4.8: Dimensionless turbulent velocity profiles.

velocity in order to compute the boundary quantities. According to reference [6], the isentropic airspeed is defined as the theoretical local speed for the inviscid flow. It can be extrapolated from the Euler numerical simulation otherwise from its definition. Thus, the isentropic Mach number is

$$M_{is} = \sqrt{\frac{2}{\gamma - 1} p^{-\frac{\gamma-1}{\gamma}-1}},$$

where p is the local pressure. So, the external temperature is defined as

$$T_{ext} = 1 + \frac{\gamma - 1}{2} M_{is}^2$$

and

$$U_e = M_{is} \sqrt{\frac{\gamma}{T_{ext}}}. \tag{4.6}$$

The equation (4.6) is very useful to compute the convective speed in the chordwise direction as described by Amiet's theory, also with scattering correction. The convective speed is a portion of the external velocity.

The boundary thickness δ is the distance from the airfoil surface for which the airspeed reaches the 99 percent of external velocity. The boundary layer is built from extrapolated points; therefore. Thus, in order to obtain a better solution, the interpolation of the available data is used and integrated. The δ is fixed as integration limit for the calculus of the displacement and momentum thickness. The quantities δ^* and θ are computed according their definitions:

$$\delta^* = \int_0^\delta \left(1 - \frac{U}{U_e}\right) \mathrm{d}\left(\frac{x}{c}\right)$$
$$\theta = \int_0^\delta \frac{U}{U_e} \left(1 - \frac{U}{U_e}\right) \mathrm{d}\left(\frac{x}{c}\right)$$

The method of trapezoids is used to solve the integral. The error committed is negligible due to the high number of points.

In Table 4.1 are compared the dimensionless displacement and momentum thickness obtained with Xfoil and RANS simulations, at different position along the chordwise and for various angle of attack. In general case, the numeric solution tends to coincide with the reference Xfoil quantities. However, it does not provide the boundary thickness that is the input for the Goody's spectrum model. Also reference [6] proposes a series of empirical equations that allows to compute δ^* and θ near the trailing edge by knowing the incidence and Reynolds number. Brooks distinguished between stunned and unstunned boundary. This last configuration corresponds to the RANS analysis carried out.

From the Table 4.1 it is evident the little error that is almost less then three percent. The extrapolation position has important effects on the estimated error. For zero incidence, the maximum error involves δ^* at 95% of the chord where it assumes about 3% value. The momentum thickness θ shows little variation in the error estimation that

Angle of attack 0°		x/c	98%
	Xfoil solution	RANS analysis	error
δ^*/c	0.005135	0.005137	-0.04%
θ/c	0.003299	0.003252	1.41%
H	1.556	1.58	
		x/c	95%
	Xfoil solution	RANS analysis	error
δ^*/c	0.004431	0.0043	-2.95644%
θ/c	0.002888	0.002838	-1.7313%
H	1.534	1.515	
		x/c	90%
	Xfoil solution	RANS analysis	error
δ^*/c	0.003742	0.003738	-0.10689%
θ/c	0.002518	0.002557	1.5488%
H	1.486	1.462	
		x/c	80%
	Xfoil solution	RANS analysis	error
δ^*/c	0.002572	0.002306	-10.34%
θ/c	0.001763	0.001508	-14.46%
H	1.486	1.462	

Table 4.1: Comparison of boundary quantities on the suction side for NACA0012 by Xfoil and RANS solution at different position and zero incidence.

varies around 1.5%. The configuration for 4° incidence, presents the same general trend. However, θ has not negligible error around 2.9% for 80% of the chord.
The configuration for 6° of incidence shows the main problems. At 95% of the chord δ^* has 0.3% error, on respect to the reference value; while θ is subjected to 3.3% error. By moving the extrapolation point towards the leading edge the absolute value of the error for δ^* increases until 6.3%. For 80% of the chord, θ have 4.7% error.

4.2.2 DU96-W-180 airfoil

The present approach is applied also for different geometries in order to discuss the effect of high adverse pressure gradient. The pressure spectra models were introduced for flat plate or thin profiles, thus, the Amiet's results cannot be applied in any possible cases. The first step consists into the extrapolation of the boundary quantities in proximity of the trailing edge. Thus, the mesh is imported into the RANS code and the fluid field is carried out. The angle of attack is always zero due to the experimental data available for the chosen profile.

Pressure distribution, in terms of c_p coefficient, is reported in Figure 4.9 where RANS prediction perfectly overlies the Xfoil solution. The different behavior between suction and pressure side is due to the not symmetrical configuration. However, a little difference is evident close to the trailing edge but it is negligible for the present purpose. Obviously, in respect of the NACA airfoil, the DU96-W-180 profile shows higher c_p in absolute value

Angle of attack 4°		x/c	95%
	Xfoil solution	RANS analysis	error
δ^*/c	0.00571	0.005757	0.823117%
θ/c	0.0036	0.003663	1.75%
H	1.58611	1.57166	
		x/c	90%
	Xfoil solution	RANS analysis	error
δ^*/c	0.004717	0.004765	1.0175%
θ/c	0.003086	0.003145	1.91186%
H	1.5285	1.5151	
		x/c	80 %
	Xfoil solution	RANS analysis	error
δ^*/c	0.004035	0.004139	2.58%
θ/c	0.002706	0.002816	3.95%
H	1.491	1.470	

Table 4.2: Comparison of boundary quantities n the suction side for NACA0012 by Xfoil and RANS solution at different position and 4° of incidence.

Angle of attack 6°		x/c	98 %
	Xfoil solution	RANS analysis	error
δ^*/c	0.0103	0.0108	4.85%
θ/c	0.0058	0.0062	6.89%
H	1.77	1.75	
		x/c	95%
	Xfoil solution	RANS analysis	error
δ^*/c	0.00819	0.008215	0.31%
θ/c	0.005130	0.00530	3.31%
H	1.6	1.55	
		x/c	90%
	Xfoil solution	RANS analysis	error
δ^*/c	0.006181	0.006048	-2.15%
θ/c	0.003922	0.003851	-1.81%
H	1.528	1.515	
		x/c	80%
	Xfoil solution	RANS analysis	error
δ^*/c	0.005316	0.00507	-4.63%
θ/c	0.003477	0.003301	-5.06%
H	1.529	1.536	

Table 4.3: Comparison of boundary quantities on the suction side for NACA0012 by Xfoil and RANS solution at different position and 6° of incidence.

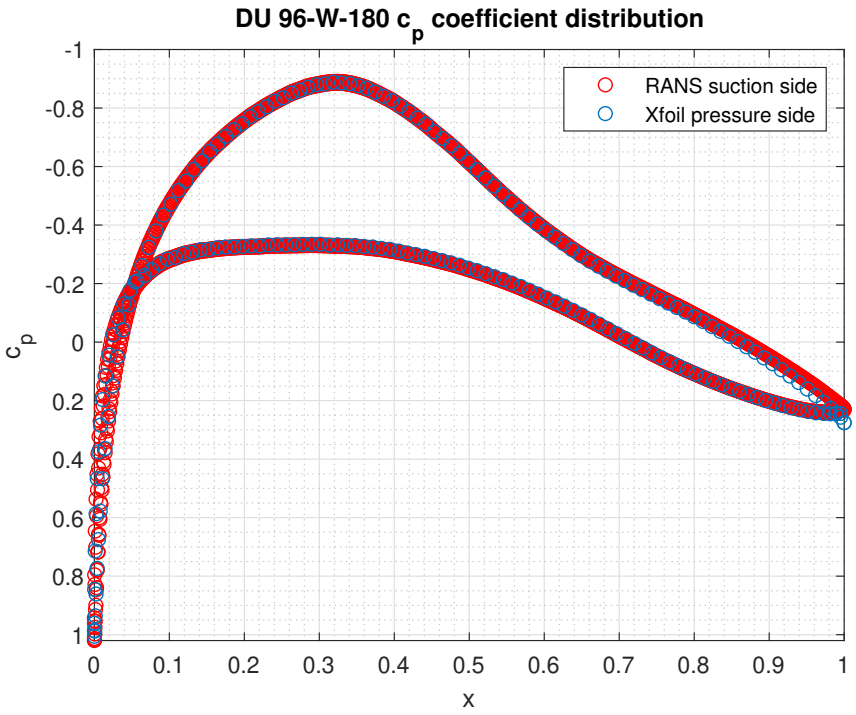

Figure 4.9: Pressure coefficient distribution around DU96-W-180 airfoil at 0° of incidence.

on the top surface that means higher local velocity.

The Figure 4.10 displays the friction coefficient distribution obtained by RANS and Xfoil solution on the entire profile. Near the leading edge, the Xfoil solution shows some peaks on both suction and pressure sides but they disappear for the RANS solution. The RANS solution displays a lower level than the reference one, while it links up with the reference curve in the central chord zone. The curves on the suction side almost coincide but the error barely increases near the trailing edge. On the pressure side the error is lower than the value computed on top surface and it is almost zero in trailing edge zone. Moreover, the error is around 2% over the central chord segment. Generally, the prediction is accurate for both pressure and friction distribution.

For further information, the Mach field around the DU96-W-180 profiles is reported in Figure 4.11. Obviously, the wake behind the body is not symmetric and the boundary layer on top seems to be larger than the bottom surface due to the curvature of the profile. Moreover, the boundary thickness is larger than the equivalent zero incidence case for NACA profile. The turbulent viscosity $\rho\tilde{\nu}$ is plotted in Figure 4.12 and it allows to evidence the zones in the fluid field where the turbulence is more intense. The central zone of the wake is characterized by an high turbulence level while the external fluid appears homogeneous with a constant level imposed in the boundary conditions. The transition from laminar to turbulent boundary layers happens close to the leading edge. According to the present observation, forced transitional position has to be imposed in Xfoil program for the calculus of reference thickness.

In Figure 4.13 the dimensionless velocity profile at different positions is plotted in

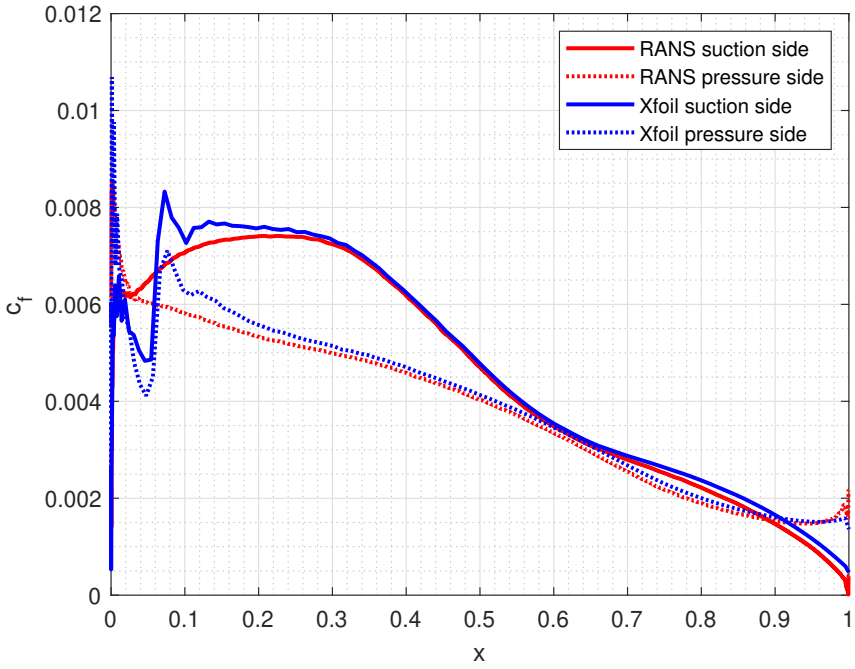

Figure 4.10: Friction coefficient distribution around DU96-W-180 airfoil at 0° of incidence.

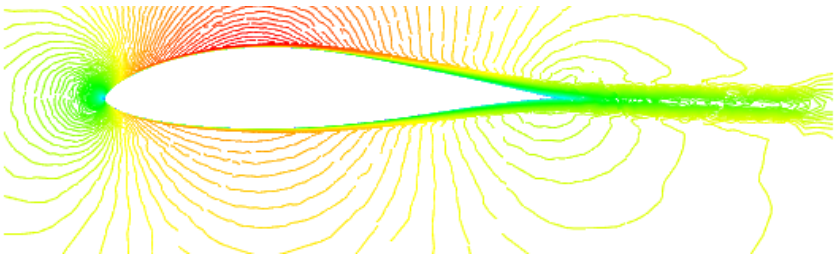

Figure 4.11: Mach field around the DU96-W-180 profile at zero angle of attack and Re=1.5 10^6.

Figure 4.12: $\rho\tilde{\nu}$ field on the DU96-W-180 profile at zero angle of attack and Re=1.5 10^6.

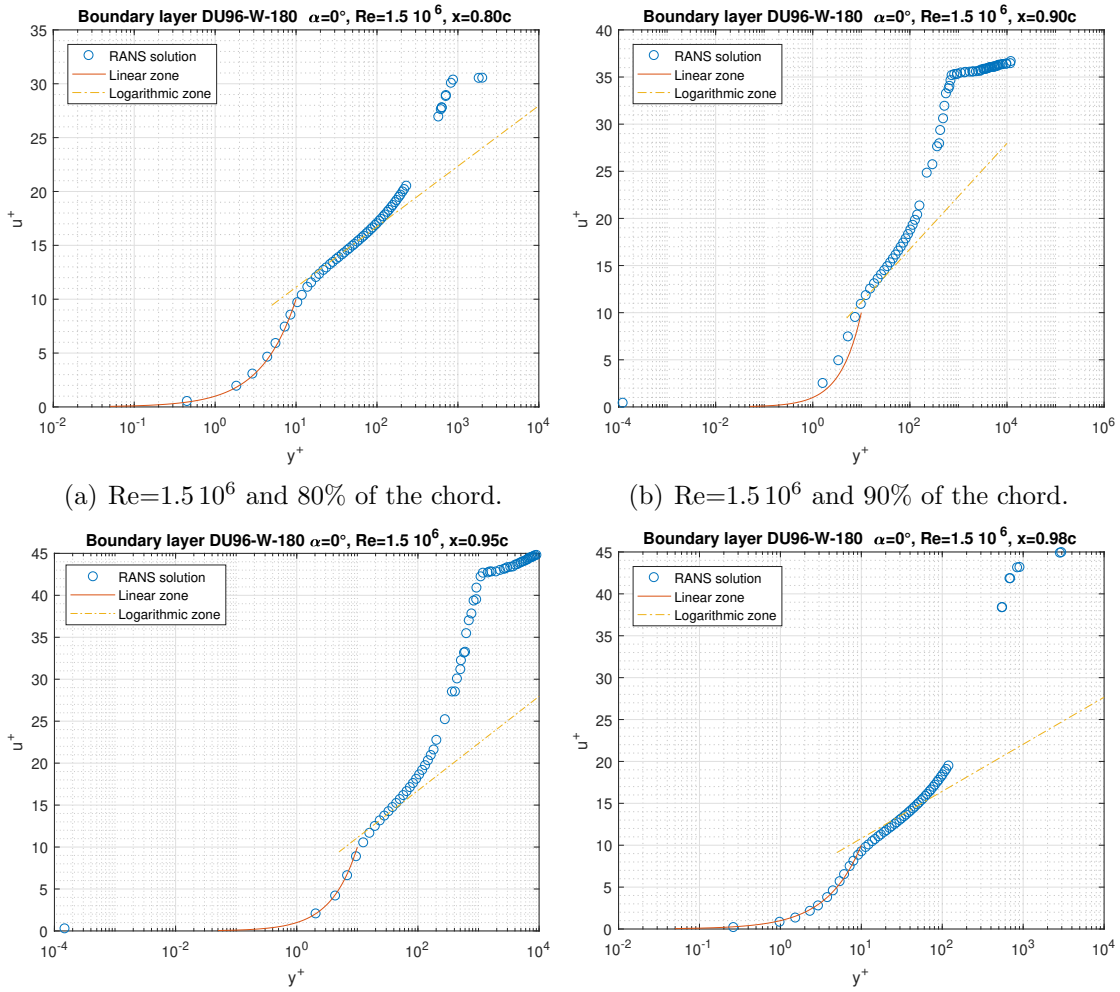

(a) Re=1.5 10^6 and 80% of the chord.

(b) Re=1.5 10^6 and 90% of the chord.

(c) Re=1.5 10^6 and 95% of the chord.

(d) Re=1.5 10^6 and 98% of the chord.

Figure 4.13: Dimensionless turbulent velocity profiles for DU96-W-180 on the suction side.

order to verify the accuracy of the RANS solution. From the Figure 4.13, the predicted boundary layer is conformed with the theoretical description excepted for $x = 0.90c$ where the linear zone does not completely overlie the theoretical trend. The boundary thickness is computed by introducing the isentropic velocity as the external airspeed. The δ thickness coincides with the distance from the surface for which the velocity reaches the 99% of the external one. The δ^* and θ is obtained according to the their definition by using the numerical integration with the trapezoidal method.

However, the Table 4.4 compares the displacement and momentum thickness on both sides of the airfoil with the reference Xfoil solution. The RANS simulation returns different errors between the suction and pressure side. Generally, the error is lower for the bottom surface rather than the suction side. However, the general trend is not predictable as function of the chordwise position. In fact, for 98% of the chord and over the suction side, θ shows the 9.55% error that decreases until 2% for $x = 0.95c$. Opposite trend is displayed for δ^*, that comes from 2.98% to 4.20% error. On the pressure side, the error

Angle of attack 0°	x/c	98%			
	Suction side			**Pressure side**	
	Xfoil	RANS	error	Xfoil	RANS	error
δ^*/c	0.010206	0.01051	2.98%	0.005777	0.005378	-6.98%
θ/c	0.005307	0.005814	9.55%	0.003654	0.003498	-4.26%
H	1.9231	1.980		1.581	1.537	
		x/c	95%			
	Xfoil	RANS	error	Xfoil	RANS	error
δ^*/c	0.007994	0.007655	-4.20 %	0.005679	0.005451	-4.01%
θ/c	0.004528	0.004445	-1.83%	0.003547	0.003349	-5.58%
H	1.765	1.7221		1.60	1.63	
		x/c	90%			
	Xfoil	RANS	error	Xfoil	RANS	error
δ^*/c	0.006069	0.005329	-12.2%	0.005193	0.0048025	-7.5%
θ/c	0.003687	0.003267	-11.4%	0.003251	0.002899	-10.8%
H	1.640	1.631		1.5973	1.660	
		x/c	80%			
	Xfoil	RANS	error	Xfoil	RANS	error
δ^*/c	0.004249	0.00403	-5.12%	0.004026	0.004503	-11.8%
θ/c	0.002721	0.002607	-4.19%	0.002564	0.003050	-18.9%
H	1.56	1.54		1.57	1.47	

Table 4.4: Comparison of boundary quantities for DU96-W-180 airfoil, obtained by Xfoil and RANS solution at different position and zero angle of attack.

is always negative. However, for both δ^* and θ, the error is between 4.01% and 7%. For this reason it is not more negligible. From the Table 4.4, it is evident for $x = 0.80c$, the boundary layer prediction on the pressure side is not accurate, with about 18 % error for θ. On the suction side the error is limited. On the other hand, the case $x = 0.90c$ shows very low accuracy on both top and bottom surface, with a mean error of 11.1% The error about δ^* and θ influences the acoustic results in different ways in function of the frequency (see chap. 8). It is evident in Figure 4.13 where the prediction is not always over the theoretical curves. However, the ratio H is almost the same for both reference and simulation prediction and the error in percentage is lower than 10%. The most accurate prediction is obtained for $x = 0.98c$ for both suction and pressure side.

Chapter 5

Acoustic simulations and results for NACA0012

The trailing edge noise is defined as the sound emitted by the turbulent interaction between the flow and the body surface in the proximity of the trailing edge. Firstly, NACA0012 airfoil is studied. The Sound Pressure Level (SPL) is calculated by substituting inside the Amiet's formula, the pressure spectrum density. However, it is very important to specify the angle of attack, the fluid conditions and the position of the observer in which the SPL is calculated. In fact, it is possible to demonstrate that the noise perception decreases like $1/z^2$, where z is the observer distance from the trailing edge. In all following cases the observer is located in the mid-span section, in order to limit the interaction with external vortexes.

And the high shape ratio wing allows to use the two dimensional solution. Generally, Amiet's approach is a valid alternative to the classical CAA method when the wing shows a shape ratio $d/b > 10$. Zero incidence configuration is firstly studied in order to understand how the airspeed and the airfoil dimension influence the noise emission. In literature the experimental data are reported for different test situations that can be correctly reproduced by imposing the right initial conditions and reference quantities. For this reason different profiles in dimensions are considered in order to discuss how the chord or span dimension influences the phenomena. The effect of Reynolds number is introduced,too.

The central frequencies assume very important interest because of the human ears sensibility. In fact, the perception of the sound is barely modified as function of the frequency and the SPL has to be weighted with a certain weight function. Thus, the observer hears a sound with a perceived SPL slightly different from the measured one. Hence, the acoustic models have to reproduce, with high accuracy, the main behavior limited at high-medium frequencies range.

The question about how the incidence influences the acoustic emission is answered. The angle of attack for the following cases 5 and 6 is fixed at 4° and 6°, respectively, while the chord is equal to 0.4 m. Nevertheless, the airfoil used for numerical simulation has null thickness at the trailing edge. However, the real models used for the experiments

			Angle of attack 0°		
CASE 1:		$\mathrm{Re} = 1.5\,10^6$	$U_\infty = 56$ m/s	$c = 0.4$ m	$2d = 1$m
Velocity	U_{ref}	293.912	m/s		
Pressure	p_{ref}	$1.0315\,10^5$	Pa		
Temperature	T_{ref}	300.9389	K		
Viscosity	μ_{ref}	$1.8310\,10^{-5}$	kg/(m s)		
CASE 2:		$\mathrm{Re} = 1.5\,10^6$	$U_\infty = 71.3$ m/s	$c = 0.3048$ m	$2d = 0.4275$ m
Velocity	U_{ref}	302.50	m/s		
Pressure	p_{ref}	$1.1024\,10^5$	Pa		
Temperature	T_{ref}	318.78	K		
Viscosity	μ_{ref}	$1.7469\,10^{-5}$	kg/(m s)		
CASE 3:		$\mathrm{Re} = 0.85\,10^6$	$U_\infty = 55.5$ m/s	$c = 0.2286$ m	$2d = 0.4275$ m
Velocity	U_{ref}	235.50	m/s		
Pressure	p_{ref}	$0.6679\,10^5$	Pa		
Temperature	T_{ref}	193.15	K		
Viscosity	μ_{ref}	$1.4900\,10^{-5}$	kg/(m s)		
CASE 4:		$\mathrm{Re} = 0.85\,10^6$	$U_\infty = 39.6$ m/s	$c = 0.3048$ m	$2d = 0.4275$ m
Velocity	U_{ref}	168.00	m/s		
Pressure	p_{ref}	$0.34122\ \ 10^5$	Pa		
Temperature	T_{ref}	98.3344	K		
Viscosity	μ_{ref}	$1.75\ \ 10^{-5}$	kg/(m s)		

Table 5.1: Table of reference quantities for different cases and at zero incidence angle.

conducted by Brooks in reference [6], are characterized by rounded edge that influences the noise radiation and it generates vortex shedding noise. Some models based on Amiet's theory were developed to simulate the vortex shedding noise[8] but they are not implemented in the present work because of their low accuracy.

5.1 Zero incidence configuration

The equation 1.36 is applied to calculate the third of band SPL. The Table 5.1 summarizes the main reference quantities and the geometrical configuration for each cases. The case 1 differs from the case 3 because of the chord dimension and the upstream airspeed, while Mach number and Reynolds are fixed by the numerical solution. Therefore, since the comparison with the two cases, it is possible to describe the chord and span dimension effects. A direct comparison is not possible because of the different U_∞; nevertheless, the analysis of the results can bring interesting conclusion. However, in the equation 1.36 the mid-span d is explicit while the chord influence is hidden inside the pressure spectrum. Increasing the span and the chord dimension, the noise emission grows, too.

The reference [6] does not provide any information about the Mach number, or the initial air conditions, except for the case 2. However, it defines a Mach of about 0.2 for all experiments without specify the details. The main parameters that define the boundary layer is the Reynolds number. In following figures only the suction side is reported in

order to guarantee a simpler interpretation of the graphs.

In Figure 5.1(a) the pressure spectra density, calculated at 80% of the chord is displayed. Rozenberg's and Lee's models are close for low frequencies and both curves assume the highest values for $f = 200$ Hz. Nevertheless, increasing the frequencies the difference between the two models arises and reaches more than 20 dB/Hz for $f = 10000$ Hz. For the central frequency range, the two curves show an error of about 2 dB/Hz that is generally acceptable. Lee's model is characterized by a very rapid decreasing trend at high frequencies while this behavior is less pronounced moving through the trailing edge. Goody's curve is almost flat around 40 dB/Hz and, for this reason, it is not adapted to reproduce correctly the acoustic phenomena on the entire frequency range. It slightly depends on the position along the chordwise.

Kamruzzaman proposed a model that differs from the Rozenberg's one at very low frequencies. For $f > 5000$ Hz the error between the Kamruzzaman's and Rozenberg's model reduces. From Figure 5.1(b) and 5.1(c) it is evident Kamruzzaman's spectrum highly depends on the boundary extrapolation position rather than the other proposed models. Goody's curve is almost invariant while the red curve is translated upward. Lee's model shows higher tangent coefficient in respect to 80% chord position. In Figure 5.1(d), the yellow curve exceeds the red one for $f > 5000$ Hz. It means the predicted spectrum is little higher for the Kamruzzaman's model, rather than the Rozenbeg's one. Goody's model is invariant and the Lee's one assumes parabolic shape.

The Figure 5.2 summarizes the PSD of the case 2 which reference values are reported in Table 5.1. The Reynolds number is $1.5\,10^6$ and the velocity U_∞ is the maximum considered in the present work. Indeed the Reynolds is the same of Case 1 the PSD is little different. The peak values are around the 55 dB/Hz and the curves do not present any particular trend that differs from the Case 1. The curves appear moved upward (downward) as the chord, or the span, arises (decreases). Is is possible to note that for 80% of the chord, the PSD level of Lee's model shows a value of 15 dB/Hz at 20 kHz. Moving forward the TE, Lee's model shows increasing values. Moreover, the Goody's curve displays a little peak for medium frequencies, that is more accentuated than the case 1.
Rozenberg's model assumes the highest values on almost the entire frequency range and it clearly differs from the Kamruzzaman's curve. Only for 98% of the chord, the order of curves is inverted at very high frequency.

The case 3 is described in Figure 5.3, where the effect of Reynolds number and geometry is evident. The Reynolds number is reduced to $0.85\,10^6$, as well as the chord and the span dimension. Obviously, the sound emission is characterized by a lower SPL rather than the first case. However, this aspect is not completely evident from the pressure spectra density. In Figure 5.3(a), the Kamruzzaman model is slightly higher than the Rozenberg's one and it differs from the case 1. Nevertheless, the curves of the two cases are very close. The peak value is reached by Rozenberg's curve for all boundary extrapolation positions considered and it is almost the same in all figures. Moreover, Goody's curve predicts the lowest PSD level on the entire frequency range but it assumes

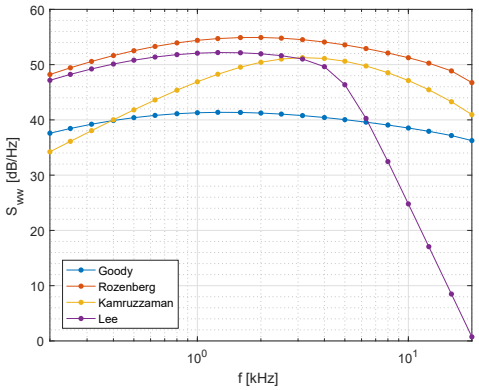

(a) PSD for Re=1.5 10^6 and 80% of the chord.

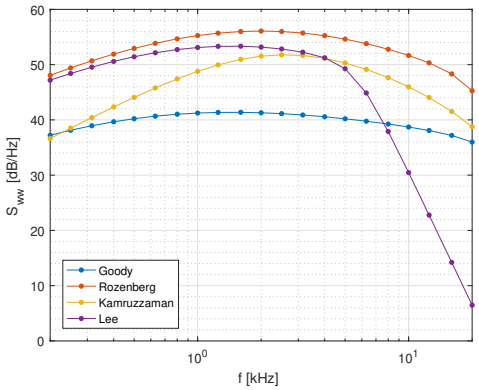

(b) PSD for Re=1.5 10^6 and 90% of the chord.

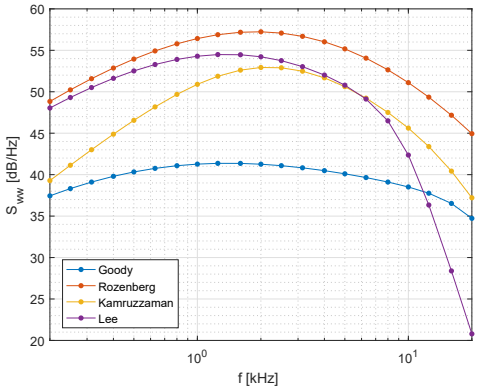

(c) PSD for Re=1.5 10^6 and 95% of the chord.

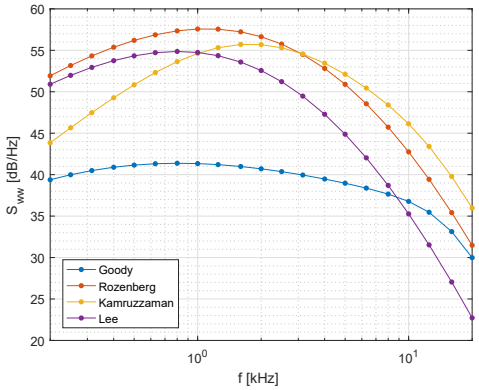

(d) PSD Re=1.5 10^6 and 98% of the chord.

Figure 5.1: Case 1: Power spectral density (PSD) at different boundary position.

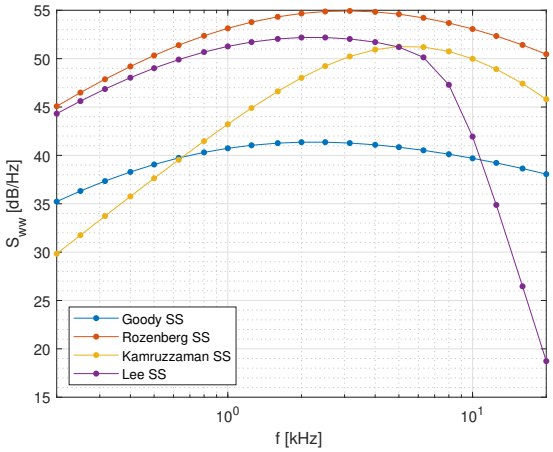

(a) PSD for Re=1.5 10^6 and 80% of the chord.

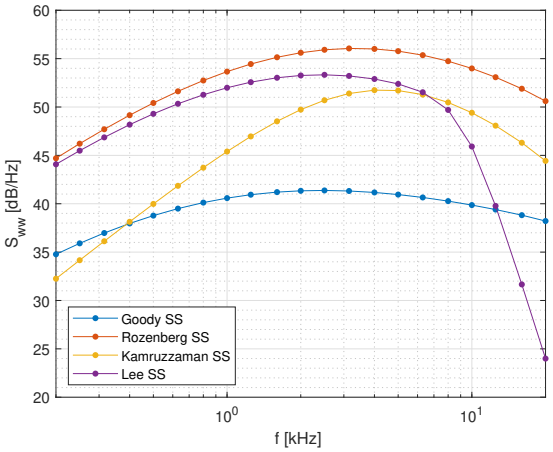

(b) PSD for Re=1.5 10^6 and 90% of the chord.

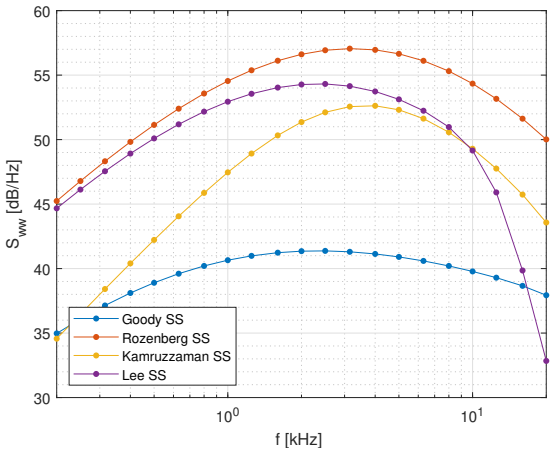

(c) PSD for Re=1.5 10^6 and 95% of the chord.

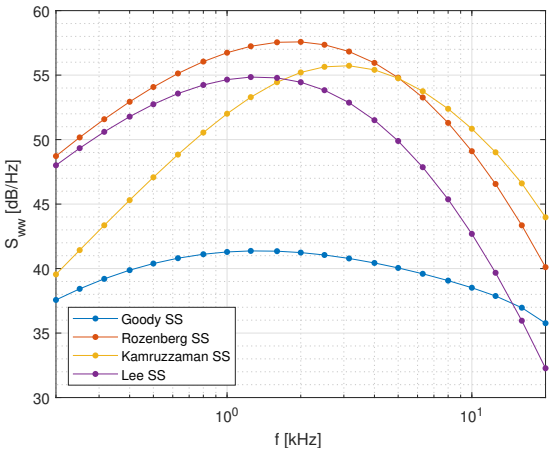

(d) PSD Re=1.5 10^6 and 98% of the chord.

Figure 5.2: Case 2: Power spectral density (PSD) at different boundary position.

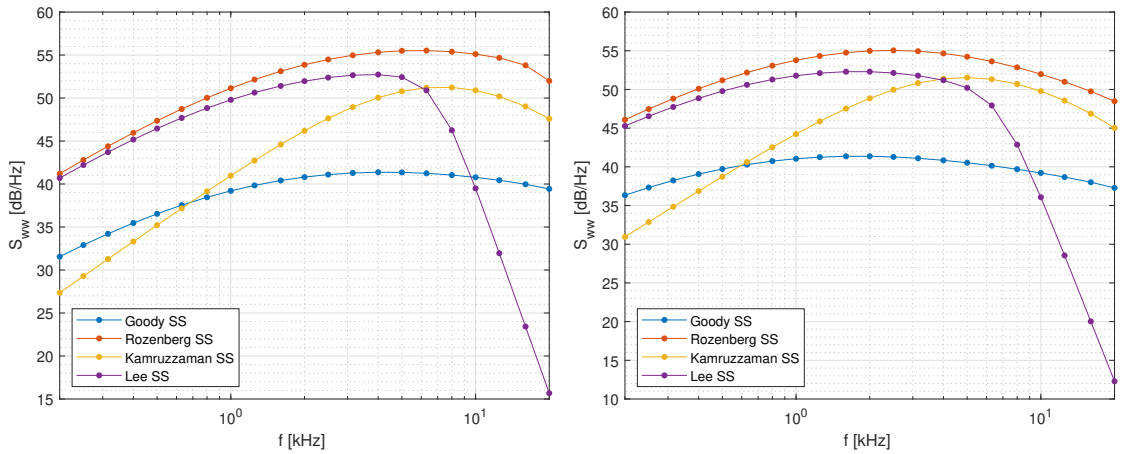

(a) PSD for Re=$0.85\,10^6$ and 80% of the chord. (b) PSD for Re=$0.85\,10^6$ and 90% of the chord.

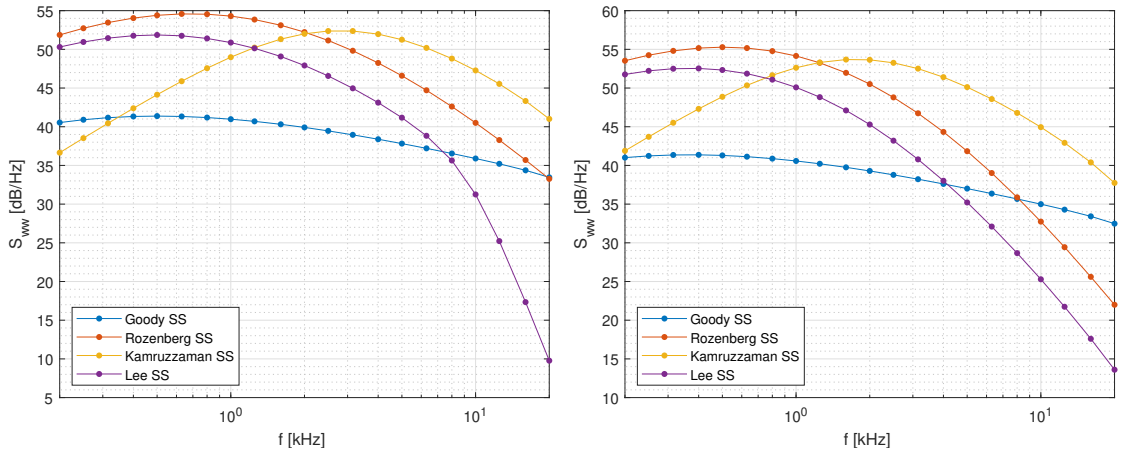

(c) PSD for Re=$0.85\,10^6$ and 95% of the chord. (d) PSD Re=$0.85\,10^6$ and 98% of the chord.

Figure 5.3: Case 3: Power spectral density (PSD) at different boundary position.

a parabolic shape. Kamruzzaman's model exceeds the red curve only at 98% of the chord and at high frequencies.

The Case 4 shows the minimum airspeed studied. In respect of the Case 2, only the velocity is reduced (and the Reynolds); thus, the expected sound emission is lower. In Figure 5.4 the PSD are plotted. The Goody's curve is almost flat around 40 dB/Hz and gradually declines by arising the frequency. However, the other models do not present any important difference from the previous described cases: Rozenberg's curve has the highest values on the entire frequency range, Kamruzzaman's model follows the Rozenberg's one and Lee's curve rapidly falls a high frequencies.

The most important difference with the case 2 is evident at high frequencies for all chord position: all the curves show a lower PSD level that sometimes is negative and not physical. This is the main behavior of Lee's model for $x = 0.80c$ and $x = 0.90c$. On the contrary, at small frequencies, Kamruzzaman's models assume higher value than the one

predicted by case 2. The peak of the curves slightly declines.

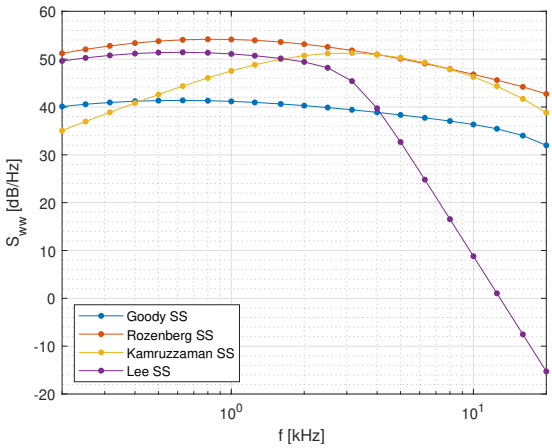

(a) PSD for Re=0.85 10^6 and 80% of the chord.

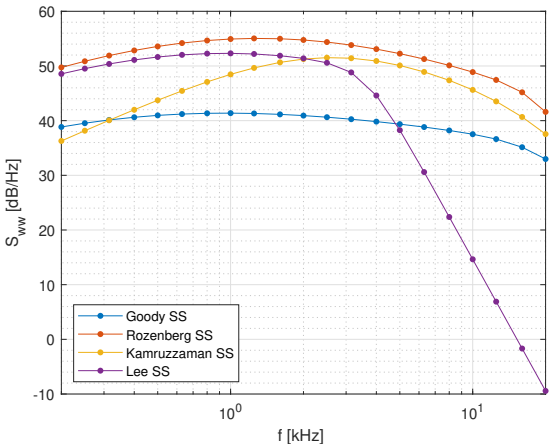

(b) PSD for Re=0.85 10^6 and 90% of the chord.

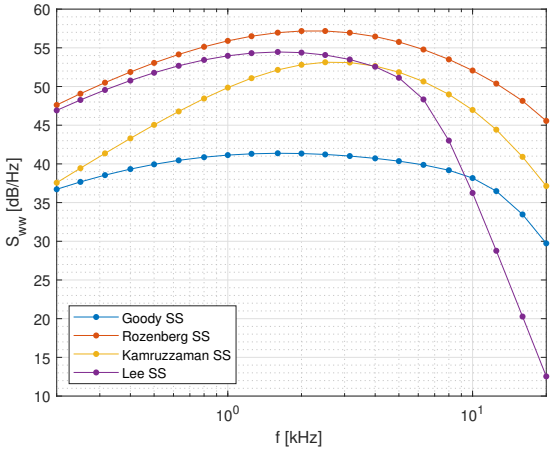

(c) PSD for Re=0.85 10^6 and 95% of the chord.

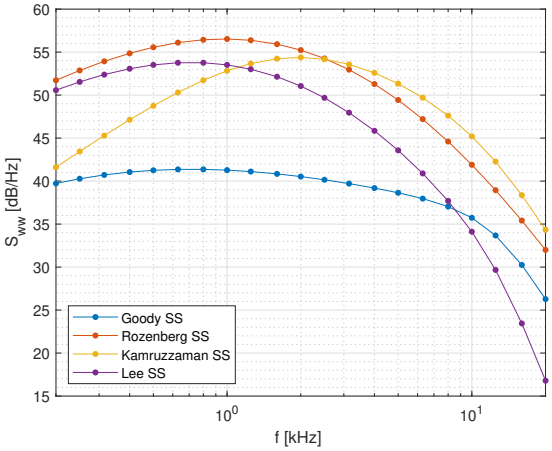

(d) PSD Re=0.85 10^6 and 98% of the chord.

Figure 5.4: Case 4: Power spectral density (PSD) at different boundary position.

Obviously, the same considerations for each case are valid for the both pressure and suction side because of the completely symmetry of the velocity field at zero incidence. Thus, the acoustic emission for the suction side has to be summed to 6 dB to count also the bottom surface contribution. However, a little difference between the two sides are inevitable due to the grid points.

The SPL is shown in the Figure 5.5, where the Amiet's theory is applied The PSD is calculated at 98% of the chord for all cases. It is evident the Goody's model is not able to describe correctly the noise emission. It introduces an error of about 9 dB for central frequencies that is not negligible. However, for very low frequencies and for the case 3, Goody's prediction is higher than Kamruzzaman's and better fix the experimental data. In Figure 5.5(c), the blue curve is very close to the Rozenberg's and Lee's models while it differs gradually by increasing the frequency. Also, the peak frequency is wrong predicted by the model.

In Figure 5.5(a), the case 1 sound emission is shown. Rozenberg's model better approximates the acoustic data. For $f > 2000$ Hz, the two curves, the red and green ones, with an error fo less than 1 dB. However, for low frequencies, Rozenberg's is not adapted for acoustic purpose, while Kamruzzaman's model introduces an error of 2 dB. The peak frequency is correctly predicted by Rozenberg. Lee's model overlaps the experimental curve for $f < 100$ Hz, indeed the curve rapidly plummets at high frequencies. This behavior makes Lee's model not accurate for acoustic prediction. In case 2, Kamruzzaman's model predictions is very accurate. The yellow graph overlaps the experimental data, almost perfectly. Goody's and Lee's models are completely wrong, while Rozengerg's tends to the green curve only for $f > 10^4$ Hz.

The case 3 was calculated in order to evince the Reynolds and geometrical effect. Kamruzzaman's curve is very close to experimental data but it is subjected to an almost constant negative error. The other models are not enough accurate. By comparison with the cases 2 and 4, it is possible to note that the sound emission for case 4 is the minimum studied at zero incidence. Obviously, reducing Reynolds number, the noise radiated declines, too. In conclusion, deceasing the velocity or the chord, while the span is constant, allows to reduce the noise emission.

In Figure 5.5(d) the Sound Pressure Level for the case 4 is displayed. It is very interesting because the geometry is the same of case 2, but the observer position, while the Reynolds number reduces. Generally, low speed means low sound pressure. By comparison with the Figure 5.5(b), the experimental SPL is smaller of about 4 dB while the predicted shape is the same in both figures. Kamruzzaman's model is still the most accurate model all over the frequency range. Rozenberg's and Lee's models are not interesting because of their rapid decreasing trend. They are completely wrong models. Goody's curve overlaps the Lee's one for very low frequencies and it slightly lowers for $f > 1000$ Hz. It introduce a good approximation in the limit of 2 dB for central frequencies.

5.2 Influence of the angle of attack

The incidence influence is here discussed. To investigate the influence of the attack angle, it is necessary to retrace the same steps for the null configuration:

1. Solve the RANS equations in order to reconstruct the velocity field around the airfoil;
2. Extrapolate the boundary layer quantities in proximity to the trailing edge;
3. Apply the pressure spectrum model as input of the Amiet's theory;
4. Compare the results with experimental data.

In Table 5.2 are reported the reference conditions used for the acoustic analysis at different angle of attack only for the NACA0012 profile because of the available experimental data. The chord is fixed at 0.4 m and the Re $= 1.5\,10^6$. The observer is locate in the normal direction on the trailing edge at distance of 1 m and in mid-span section. The Mach number is 0.16 for all following simulations.

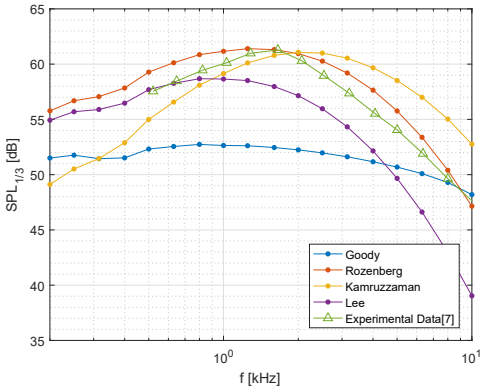

(a) Case 1: Sound pressure level.

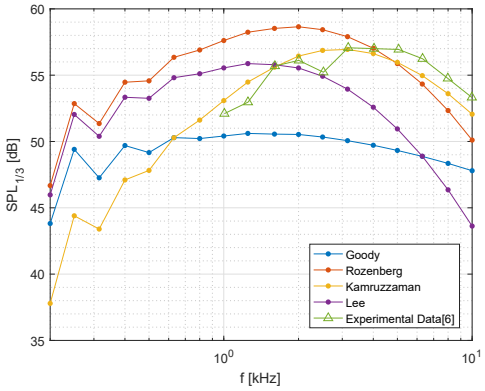

(b) Case 2: Sound pressure level.

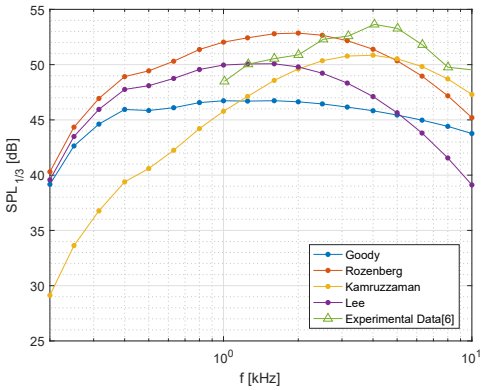

(c) Case 3:Sound pressure level.

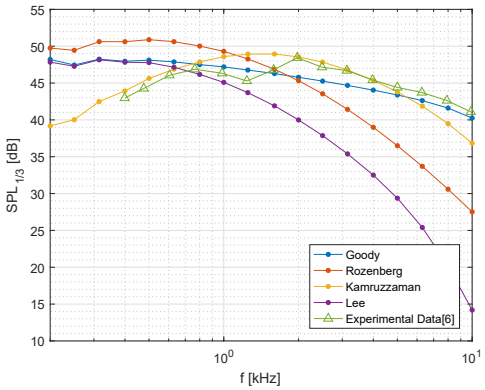

(d) Case 4:Sound pressure level.

Figure 5.5: Comparison of the noise emission due to different pressure spectrum models at zero incidence angle.

			Angle of attack 4°		
CASE 5:		$\mathrm{Re} = 1.5\,10^6$	$U_\infty = 54.8$ m/s	$c = 0.4$ m	$2d = 1$m
Velocity	U_{ref}	279.1917	m/s		
Pressure	p_{ref}	$0.9327\,10^5$	Pa		
Temperature	T_{ref}	271.3734	K		
Viscosity	μ_{ref}	$1.7404\,10^{-5}$	kg/(m s)		
			Angle of attack 6°		
CASE 6:		$\mathrm{Re} = 1.5\,10^6$	$U_\infty = 53$ m/s	$c = 0.4$ m	$2d = 1$ m
Velocity	U_{ref}	269.93	m/s		
Pressure	p_{ref}	$0.8725\,10^5$	Pa		
Temperature	T_{ref}	253.83	K		
Viscosity	μ_{ref}	$1.6834\,10^{-5}$	kg/(m s)		

Table 5.2: Resuming table of small angle of attack.

The total sound emission is the result of the pressure fluctuation propagation on both side of the airfoil. The velocity field is not symmetric and the boundary layer quantities have to be extrapolated on the both body surfaces. In Figure 5.6 are reported the pressure spectra curves, obtained at different chord position. Suction and pressure side curves are compared in the two figures. Obviously, the pressure side is characterized by a thinner boundary layer and it barely influences the acoustic emission: the PSD is lower than the one calculated on the suction side which represents the main contribution for the acoustic phenomena. However, the pressure side is not negligible and it contributes on the total SPL level. In all cases, Rozenberg's curve shows the greatest values and it is assumed as reference. Goody's model is still the less reliable approach in terms of pressure spectra. In fact, it is characterized by very low level and it introduces an error of 20 dB/Hz in respect to the Rozenberg's model. The general trend is well predicted as well as the frequency peak is almost the same for all models (except for the Kamruzzaman's that reaches the greatest value very close to 2000 Hz). The PSD on the pressure side is reported in Figure 5.6(b). For Goody's model, the curves are very similar Thus, Goody's model is not able to capture the differences between the two body surfaces. However, the angle of attack is very little and the fluid field is barely affected by incidence. A first comparison with previous studied cases proves that the curve at zero incidence has lower values. Thus, arising the incidence implies a grow of noise. The peak slightly grows (about 1 dB/Hz), and the error remains almost constant all over the frequency range. The peak corresponding frequency is lower than 1 kHz.

Rozenberg's model has the highest level at low frequencies that are not significant for the acoustic emission. The curve reaches the peak at mean frequencies and rapidly decreases. The same trend is evident for Kamruzzaman's and Lee's approaches. Particularly, Rozenberg's curve show a peak value of 58 dB/Hz, which is higher than 56 dB/Hz obtained for the zero incidence angle configuration. Analogous considerations can be observed in PSD graph between the pressure and suction side.
In Figure 5.6(b), the corresponding curves to Rozenberg's and Lee's approaches have a parabolic trend and they immediately drop. As consequences, the pressure side is characterized by a lower PSD level. Its difference with the suction side grows at high frequencies. The related effect becomes more and more important at high incidence angle when the acoustic phenomena coincide with the main term radiated by the suction side. Kamruzzaman's model is an exception because the two curves are very similar on both body surfaces and the contribution of pressure side is not negligible on the entire range of frequencies. Hence, the error between the pressure and suction side is evident and the two results are very similar. They differ with an error of 2 dB/Hz for $f = 200Hz$, until null value for $f = 20$ kHz.
Lee's model is slightly affected by the angle of attack. Hence, the main difference with the null configuration consists into the rapid reduction of the value that reaches less than 10 dB/Hz at high frequencies.

The PSD is extrapolated at 98% of the chord,too. The main difference with the previous case consists mainly in the shape of pressure side spectrum. Goody's model is not able to evidence the difference between the both sides of airfoil. In fact the two blue curves

in Figures 5.6(d) and 5.6(c) are very similar. Thus, the blue curves in the Figures 5.6(c) and 5.6(d) overlie for a large frequency range. Lee's and Rozenberg's models present PSD on the pressure side higher than the suction side curve. The difference is evident at high frequencies and it becomes the main contribution for acoustic purpose.

In order to complete the study of the extrapolation point influence, in Figure 5.7 are

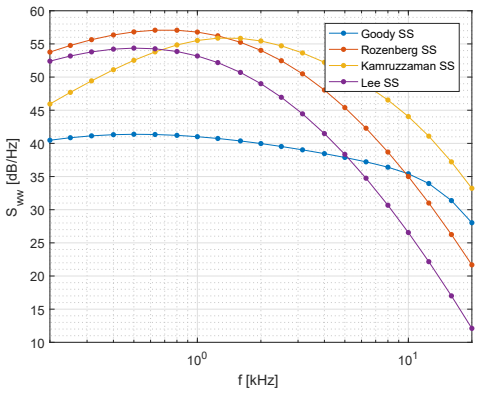

(a) Case 5:S_{ww} on the suction side and 95% of the chord.

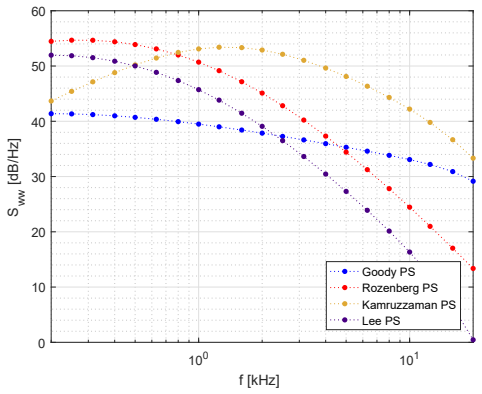

(b) Cae 5: S_{ww} on the pressure side and 95% of the chord.

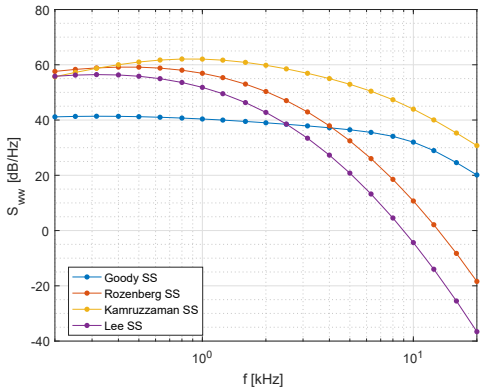

(c) Case 5: S_{ww} on the suction side and 98% of the chord.

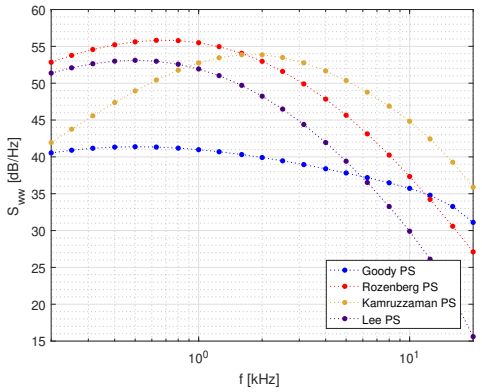

(d) Case 5: S_{ww} on the pressure side and 98% of the chord.

Figure 5.6: Comparison of the PSD on the pressure (PS) and suction side (SS) at different chord position for the case 5.

reported the S_{ww} plots for 80% and 90% of the chord.

In Figure 5.8 the acoustic emission is compared with the experimental data. The chord position is influential rather than the previous cases and this aspect is evident due to the almost null error introduced with the acoustic data. For $x = 0.80c$, all considered models are not able to correctly predict the acoustic emission. Rozenberg's and Goody's model are very close over the entire frequency range and they assume the maximum predicted SPL level. However, the two curves overlie the experimental data only for $1000 < f < 2000$ Hz; while the error rises with the frequency. Lee's prediction underestimates the noise emission for all frequencies. Moreover, Kamruzzaman's curve il

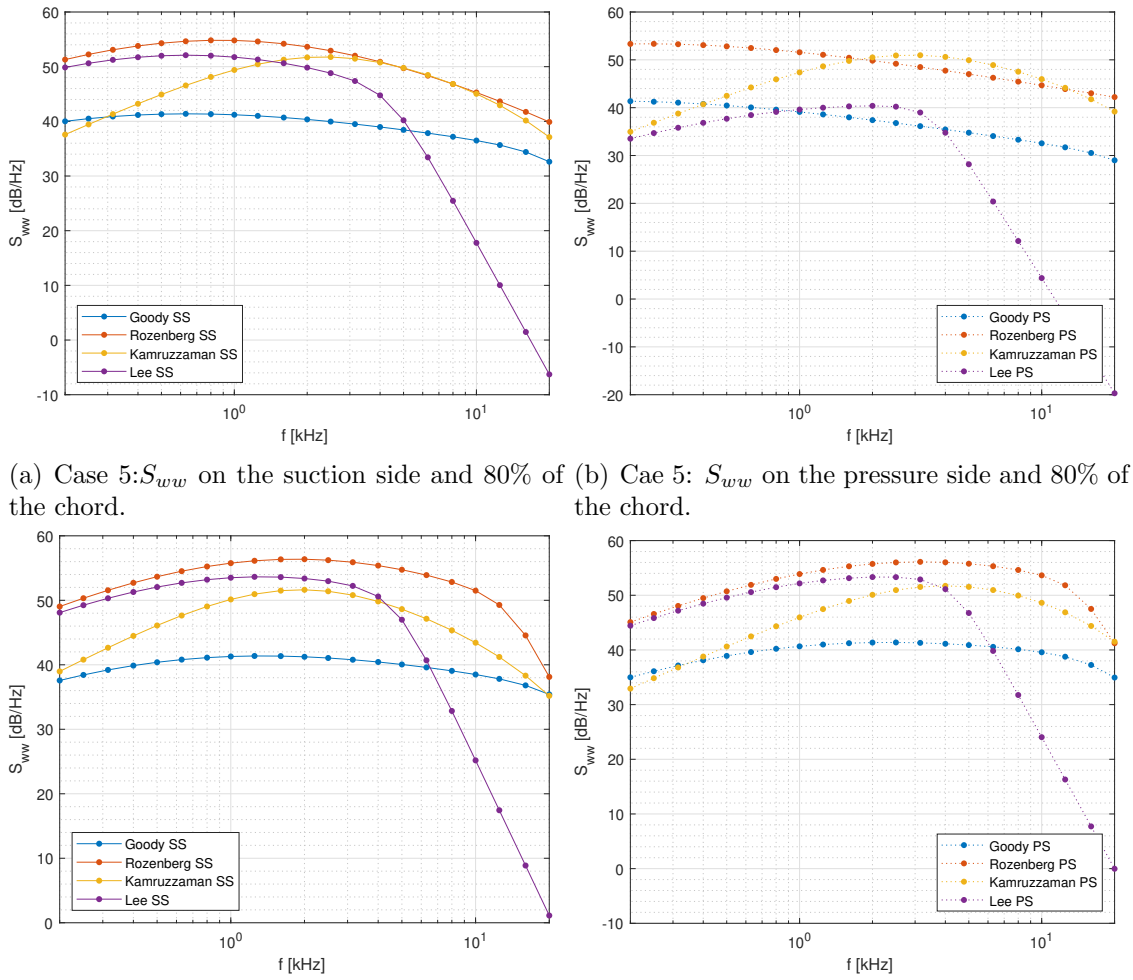

(a) Case 5:S_{ww} on the suction side and 80% of the chord.

(b) Cae 5: S_{ww} on the pressure side and 80% of the chord.

(c) Case 5: S_{ww} on the suction side and 90% of the chord.

(d) Case 5: S_{ww} on the pressure side and 90% of the chord.

Figure 5.7: Comparison of the PSD on the pressure (PS) and suction side (SS) at different chord position for the case 5.

lower than the green curve until 2000 Hz and it overestimates the SPL for $f > 2000$ Hz. Analogous considerations can be made for $x = 0.90c$, where only Rozenberg's model is accurate over a very restrict range. Nevertheless, moving forward the TE, the prediction better fits the experimental points. For $x = 0.95c$, Kamruzzaman's model fits the experimental data mainly for the central frequencies. Lee's and Goody's model are not able to describe the acoustic phenomena as well as Rozenberg's one. However, Kamruzzaman's approach predicts a surplus error of 2 dB. In Figure 5.8(d) the graph shows the best agreement with the experiments. Rozenberg's model perfectly describes the acoustic emission for central frequencies but it differs from the green plot for $f > 3000$ Hz when Goody's model appears to be the best solution. Kamruzzaman's plot overestimates the acoustic emission; thus it is a conservative approach. However, the error is very low at 1000 Hz. Lee's model shows completely wrong trend. In conclusion, it is not possible to define which model mainly describes the acoustic phenomena all over the frequency range. Nevertheless, using Rozenberg's approach appears the best solution to guarantee

a reduction of predicted error over the medium frequencies.

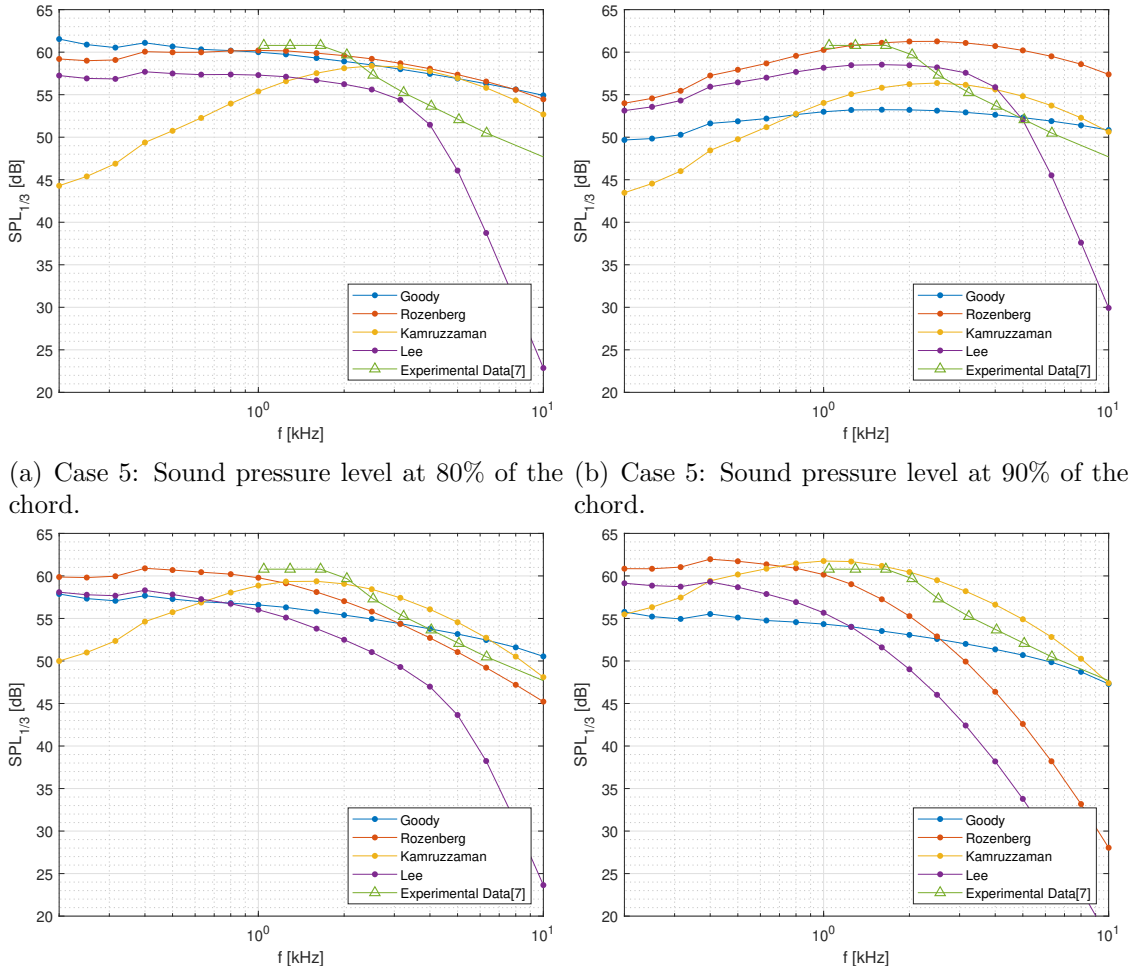

(a) Case 5: Sound pressure level at 80% of the chord.

(b) Case 5: Sound pressure level at 90% of the chord.

(c) Case 5: Sound pressure level at 95% of the chord.

(d) Case 5: Sound pressure level at 98% of the chord.

Figure 5.8: Comparison of the noise emission due to different pressure spectrum models at 4° incidence and various chord position.

The case 6 is reported in the Figure 5.9, where the suction and pressure side PSD are compared. The angle of incidence implies a growing peak in respect to the case 5. The boundary layer quantities are extrapolated only at 95% and 98% of the chord. As demonstrated in the previous chapters, the sound level is well predicted while approaching the trailing edge. Thus, the pressure spectrum is computed and plotted in Figure 5.9.

The differences between the two body sides are more evident. However, the contribution of the pressure side spectrum in not negligible; even at high frequencies where it is the main acoustic component. The curves obtained on suction side has parabolic shape in semi logarithmic graph, and the value decreases very rapidly for Rozenberg's and Lee's models. Comparing with the previous cases, at very high frequencies the spectrum assumes negative values that are not physically acceptable. This problem does not belong to Kamruzzaman's approach which have positive value on the entire range of frequency

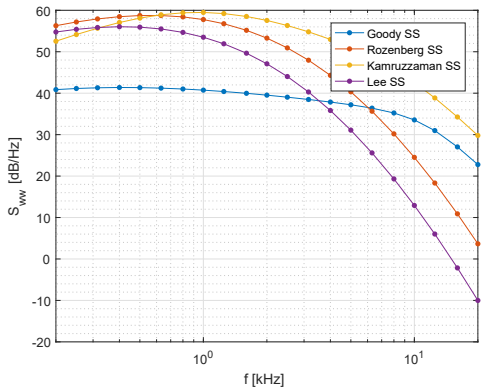

(a) Case 6:S_{ww} on the suction side and 95% of the chord.

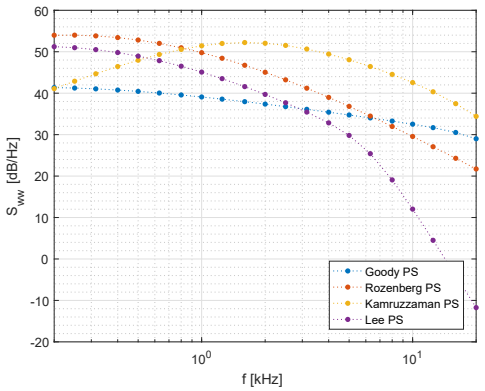

(b) Case 6: S_{ww} on the pressure side and 95% of the chord.

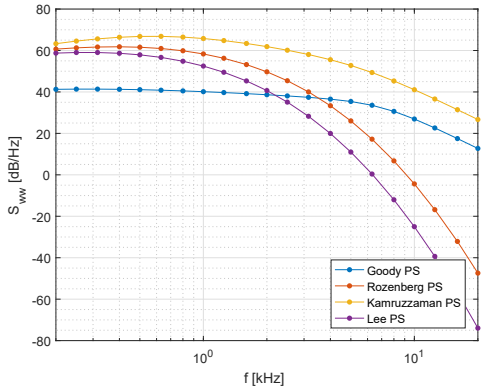

(c) Case 6: S_{ww} on the suction side and 98% of the chord.

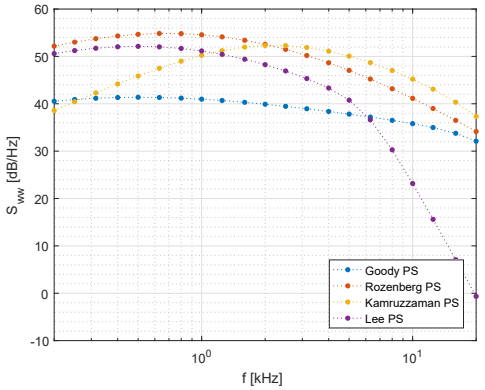

(d) Case 6: S_{ww} on the pressure side and 98% of the chord.

Figure 5.9: Comparison of the PSD on the pressure (PS) and suction side (SS) at different chord position for the case 6.

variation.

About the case $x = 0.95c$, the pressure spectra are close each other especially at low frequencies. Kamruzzaman's curve assumes the highest values while Goody's one shows a flat curve. It is an obviously conclusion due to the dependence of the models from the boundary quantities. With respect to the zero incidence, on the pressure side the boundary layer is characterized by smaller thickness, that implies also little δ^* and θ; as consequences the pressure spectrum exhibit a decreasing intensity.

Finally, the PSD is plotted also for 80% and 90% of the chord. In these cases, the curves are very similar.

In Figure 5.9(c) the suction side spectrum is reported. The previous consideration are still valid about the general behavior of the models. Only kamruzzaman's model shows a considerable peak of 67 dB/HZ for $f = 670$ Hz. Rozenberg's and Lee's models assume the same behavior and they present lower level than Kamruzzaman's one. Goody's model is the worst approach due to its almost constant value for a large frequency range. The blue curve slightly depends on frequencies only for $f > 2000$ Hz. The pressure side

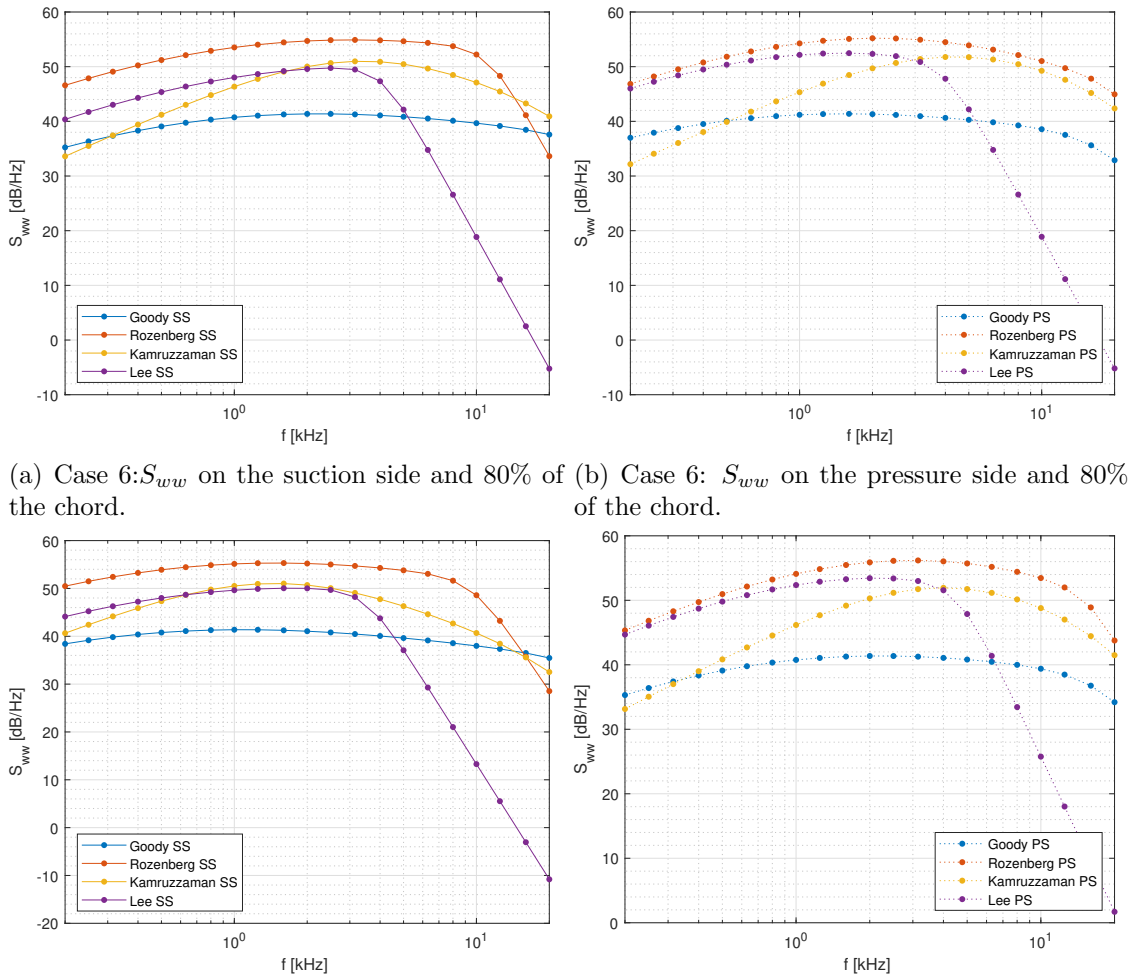

(a) Case 6:S_{ww} on the suction side and 80% of the chord.

(b) Case 6: S_{ww} on the pressure side and 80% of the chord.

(c) Case 6: S_{ww} on the suction side and 90% of the chord.

(d) Case 6: S_{ww} on the pressure side and 90% of the chord.

Figure 5.10: Comparison of the PSD on the pressure (PS) and suction side (SS) at different chord position for the case 6.

curves are plotted in the Figure 5.9(d) and compared with the suction side prediction. Kamruzzaman's model is characterized by predicted values less than the corresponding suction side curve for the entire considered interval. In fact, the errors reduces with the frequencies. It is about 20 dB/Hz for very low frequencies while it reaches the null value for 8000 Hz. Goody's prediction is always higher than the corresponding suction side curve. Furthermore, Rozenberg's and Lee's curves exceed the comparable plot for $f > 1000$ Hz and they become the main contribution. In refers to the previous cases, the effect of the incidence is mainly relevant. While the zero incidence angle does not show the problem of the two different spectra on both airfoil sides due to airfoil symmetric configuration, the extrapolation of suction side boundary layer is enough to describe the entire acoustic measurement. The comparison with the experimental data is necessary to validate the models. However, it is evident from the Figures 5.11(c) and 5.11(d), there is no complete superposition between the experimental and the predicted data. The location over chordwise direction strong influences the model results. Lee's model is completely not

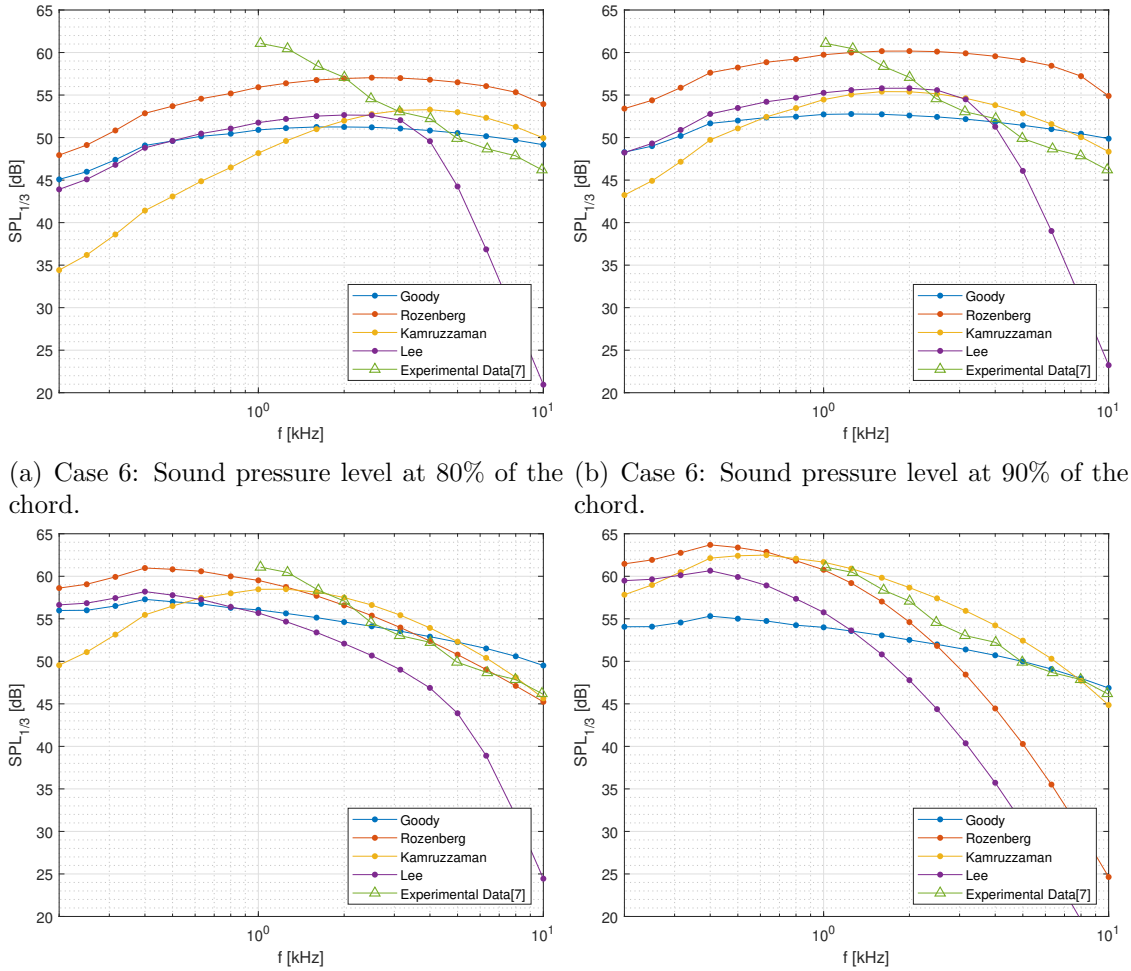

(a) Case 6: Sound pressure level at 80% of the chord.

(b) Case 6: Sound pressure level at 90% of the chord.

(c) Case 6: Sound pressure level at 95% of the chord.

(d) Case 6: Sound pressure level at 98% of the chord.

Figure 5.11: Comparison of the noise emission due to different pressure spectrum models at 6° incidence and various chord position.

adapted for the present purpose. The acoustic level is always lower than the experimental measurements and the errors progress with the frequency, until 25 dB for $f = 20$ kHz. For the medium frequencies, the differences introduced by the model is around -6 dB. This aspect makes Lee's approach completely wrong on the entire range of frequencies for both chord positions studied. Goody's approach is enough accurate for very high frequencies, where the blue curve overlies the experimental data for $x = 0.98c$, while it makes available an higher prediction for $x = 0.95c$. In Figure 5.11(d), Kamruzzaman's model predicts higher SPL than the experimental measurement with a constant error of 4 dB between 2000 and 5000 Hz. Around the $f = 1000$ Hz, the difference is reduced but still not negligible. However, Rozenberg's model offers the best approximation for the medium frequencies due to a constant error of about 2 dB. In Figure 5.11(a) and 5.11(b), the noise prediction disagrees with the experimental data. In Figure 5.11(c), the acoustic emission is plotted for chord position $x = 0.95\%$. Rozenberg's and Kamruzzaman's curves perfectly overlie the green curve. This is the best configuration studied.

Chapter 6

Acoustic simulations and results for DU96-W-180

The trailing edge noise is the most significant contribution also for DU96-W-180 airfoil. The main purpose is to verify if the proposed approach in the present work is available for non-symmetrical profiles also. Only zero incidence case is studied because of the available experimental data. The observer is located in mid-span section, over the trailing edge, at distance of one meter. The angle of attack and fluid reference conditions are specified in Table 6.1. The chord is fixed at 0.4 m and the spanwise is about 1 m. For DU96-W-180, the effect of the geometrical dimension is not described. However, since the conclusion of the previous chapter, it is possible to deduct that the increasing chord dimension, implies growing SPL.

In Figure 6.1(c), the suction side spectrum is plotted. Rozenberg's model achieves the peak level of 55 dB/Hz for 1 kHz. Increasing frequencies implies a rapid decreasing curve which trend is more emphasized than higher chord position,especially for Lee's model. As the frequency increases, the curve plummet more dramatically with respect to other models, especially Lee's model. In fact, from Figures 6.2(a) and 6.2(c), the pressure spectrum level is about 30 dB/Hz at 20 kHz, while Lee's curve reaches 10 dB/Hz. Furthermore, in Figure 6.1(d), the yellow curve is the most significant case for the pressure side.

The pressure spectrum comparison on the both airfoil sides at 95% of the chord is shown in Figure 6.2(a). Goody's model is negligible due to low predicted pressure level. The curve is invariant among the chord position and it is almost flat around 40 dB/Hz. Obviously, the behavior of the pressure spectra strictly depends on the body surface where

		Angle of attack 0°			
CASE 7:		$\mathrm{Re} = 1.5\,10^6$	$U_\infty = 56$ m/s	$c = 0.4$ m	$2d = 1$m
Velocity	U_{ref}	293.912	m/s		
Pressure	p_{ref}	$1.0315\,10^5$	Pa		
Temperature	T_{ref}	300.9389	K		
Viscosity	μ_{ref}	$1.8310\,10^{-5}$	kg/(m s)		

Table 6.1: Reference fluid conditions for DU96-W-180 profile.

the boundary quantities are measured. In fact, on the suction side, Rozenberg's model displays higher values than the other curves on the entire frequency range. It reaches 62 dB/Hz at $f = 2$ kHz and slowly lowers at high frequencies where the pressure level amounts to 42 dB/Hz. However, Kamruzzaman's and Lee's models perfectly overlies for a large frequencies interval and the error is negligible in the areas where the two curves slightly diverge. The predicted spectrum is characterized by a peak of 58 dB/Hz at about 1.5 kHz.

On the pressure side, Karmruzzaman's prediction is higher than the remaining models on frequency interval from 1 kHz to 20 kHz. Goody's curve does not present important changes while Rozenberg's and Lee's models plummet until negative values for high frequencies. Moreover, the importance of the suction side is emphasized for $f > 5$ kHz. Rozenberg's and Lee's show the same trend but they diverge of about 3 dB/Hz.

The pressure spectrum at 98% over the suction side of the chord is shown in Figure 6.2(c). The curves for Kamruzzaman's and Lee's models are very close and similar on the entire frequency range, where the maximum error is less than 2 dB/Hz at very high or lowest frequencies. According to Goody's spectrum, the pressure fluctuations have almost constant level around 40 dB/Hz. Rozenberg's prediction displays the maximum value of 61 dB/Hz around $f = 1\,kHz$, while it rapidly falls until 36 dB/Hz at $f = 20$ kHz. Furthermore, it introduces the highest pressure spectrum. The same trend is evident also for the pressure side where, the particular airfoil shape is approached with a flat plate. Except for the Goody's model,which prediction of about 52 dB/Hz for low frequency is the same on both sides, the other models show differences on the surface bodies. The differences rise by growing frequencies and the spectrum level rapidly decreases. In respect to the Figure 6.2(d), the main dissimilarities are evident at high frequencies where the suction side shows more than 20 dB/Hz gap. This confirms that the pressure fluctuations on the top surface assume the main acoustic contribution, while the pressure side in completely negligible at very high frequencies. However, for the central frequency range the spectrum level is almost the same for all models and both profile sides contributions are important. In Figure 6.2(d), Kamruzzaman's model assumes the highest values on the entire frequency range, while Goody's one returns values rounded down. For this reason, Rozenberg's or Kamruzzaman's has to be preferred indeed the acoustic prediction is rounded up as the Figure 6.3 displays.

The effect of the geometry is evident with reference to the Figures 5.5(a) and 6.3. For the DU96-W-180 profile, at zero incidence, the measured emission peak moves at 1 kHz and it reaches 65 dB; while the NACA0012 profile presents 60 dB peak. Hence, the symmetrical geometry, that is characterized also by a thinner thickness, produces a reduced noise and it should be preferred in some applications in which aerodynamic properties, such as the lift or drag coefficient, are not predominant requirements. On the other hand, the asymmetrical configuration introduces high acoustic emission that is not always predictable by the pressure spectra-based theories. The choice of the geometry cannot be reduced only on the acoustic requirement.

In Figure 6.3 the comparison of the predicted noise emission and the experimental

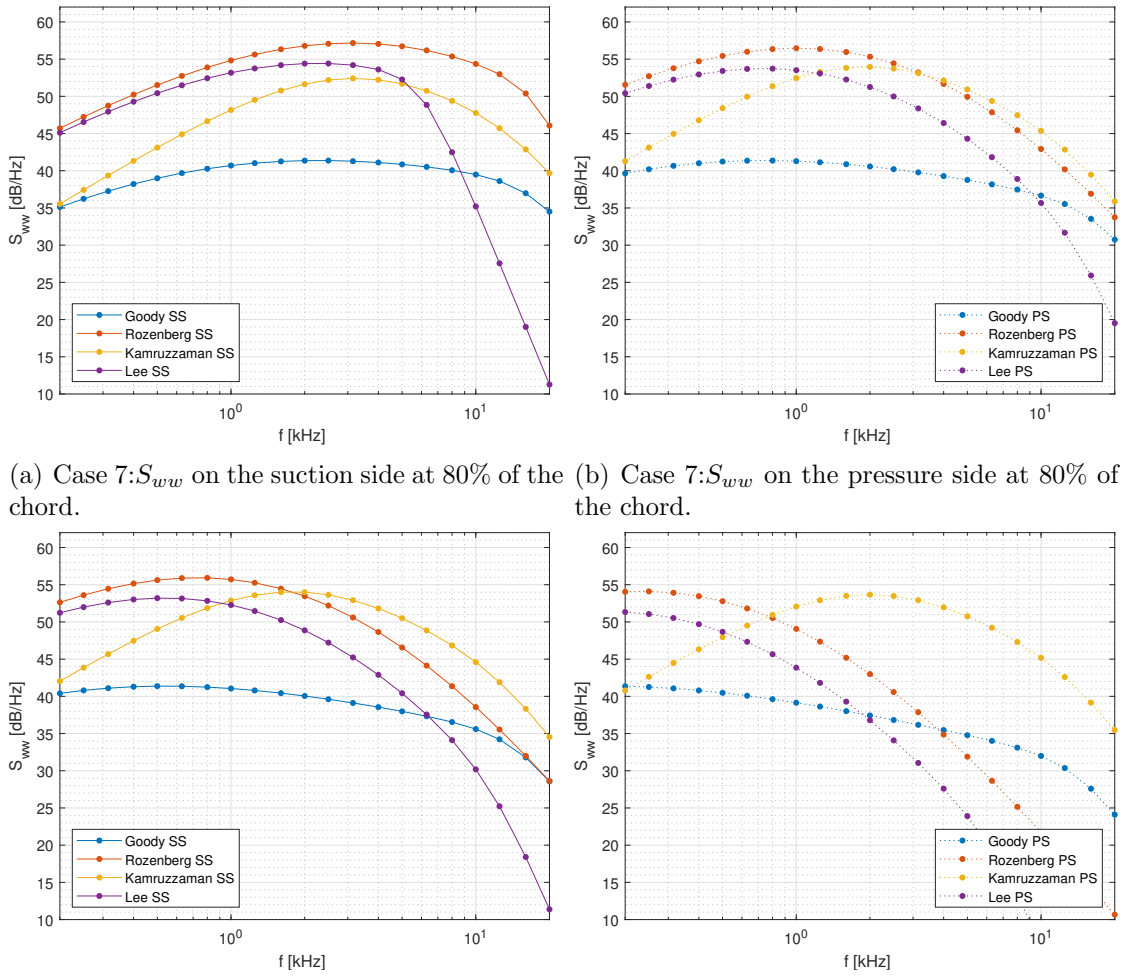

(a) Case 7:S_{ww} on the suction side at 80% of the chord.

(b) Case 7:S_{ww} on the pressure side at 80% of the chord.

(c) Case 7:S_{ww} on the suction side at 90% of the chord.

(d) Case 7:S_{ww} on the pressure side at 90% of the chord.

Figure 6.1: Comparison of the PSD on the pressure (PS) and suction side (SS) at different chord position for DU96-W-180 airfoil.

data is reported. For $x = 0.98c$, no pressure model is able to correctly predict the acoustic emission all over the considered frequency range. Moreover, the models improved do not correctly predict the peak. For frequencies between 2 and 5 kHz, Lee's model is the most accurate one because it overlies the experimental points. However, by increasing the frequencies, it is difficult to establish which model is more adapted for the phenomena description. Rozenberg's and Kamruzzaman's predictions are very close on the entire frequency interval. The two curves are higher than the experimental data. Thus, the solutions can be used for conservative predictions. The error is about 5 dB.
The same trend is evident for the other chord positions. The graph of the acoustic emission at 95% of the chord is plotted in Figure 6.3(c). The noise peak is not correctly predicted and no curves rounded the experimental data. Kamruzzaman's prediction is the most accurate in the interval $2\,\text{kHz} < f < 10\,\text{kHz}$. Lee's model perfectly overlies the green curve for a limited frequency range, while it generally reproduce a lower noise prediction.

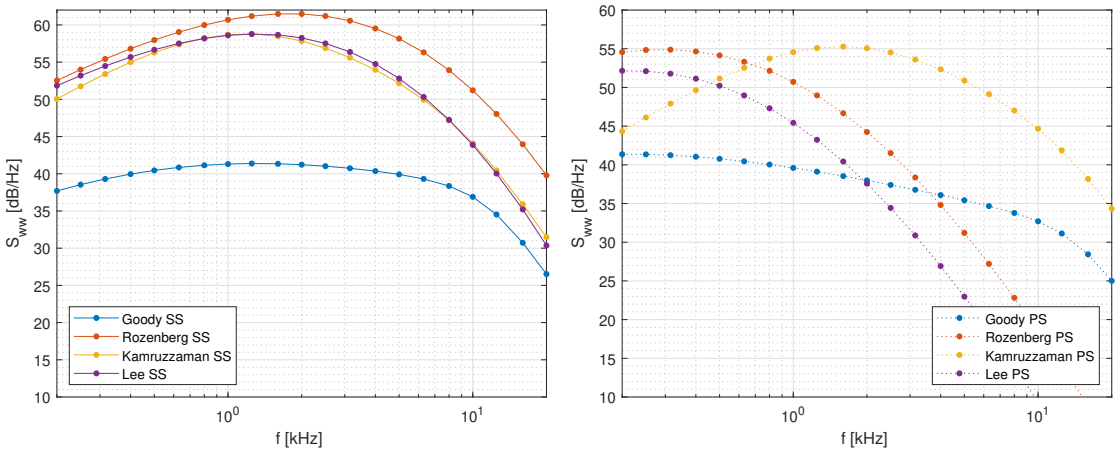

(a) Case 7:S_{ww} on the suction side at 95% of the chord.

(b) Case 7:S_{ww} on the pressure side at 95% of the chord.

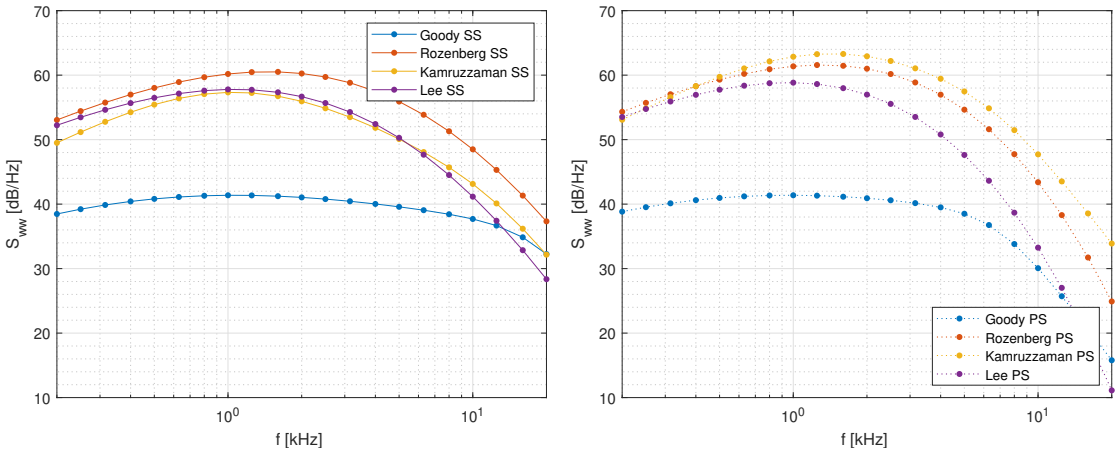

(c) Case 7:S_{ww} on the suction side at 98% of the chord.

(d) Case 7:S_{ww} on the pressure side at 98% of the chord.

Figure 6.2: Comparison of the PSD on the pressure (PS) and suction side (SS) at different chord position for DU96-W-180 airfoil.

Similarly, the SPL plot for 90% and 80% of the chord are reported in Figure 6.3(b) and 6.3(a), respectively. Paradoxically, moving forward the boundary extrapolation point, the proposed approach better approximates the acoustic data. In fact, from Figure 6.3(b), it is evident both Lee's and Kamruzzaman's models are able to reproduce the trailing-edge noise with a reduced error (less than 2 dB for the central frequencies). However, the numerical solution does not predict th emission peak as well as the corresponding frequency. The reason relies on definition of trailing edge noise as broadband noise and the tonal emission is generally radiated by vortex shedding phenomena. Indeed the error committed in the boundary layer quantities, in general the prediction concordances with the experimental data.

For $x = 0.80c$, all models do not describe perfectly the acoustic phenomena. Rozenberg's one is still the less accurate with an difference between 5 and 10 dB. The same considerations are valid for the remaining models.

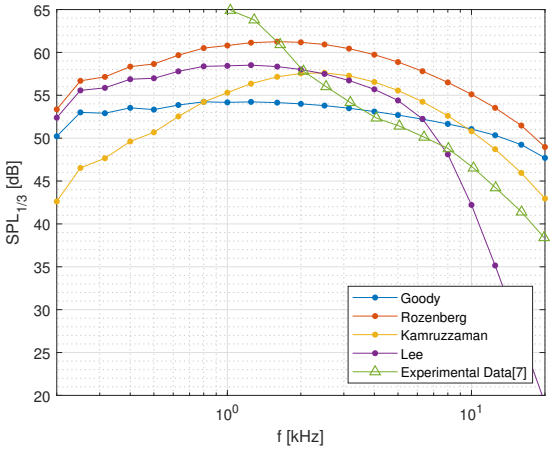

(a) Case 7:S_{ww} on the suction side at 80% of the chord.

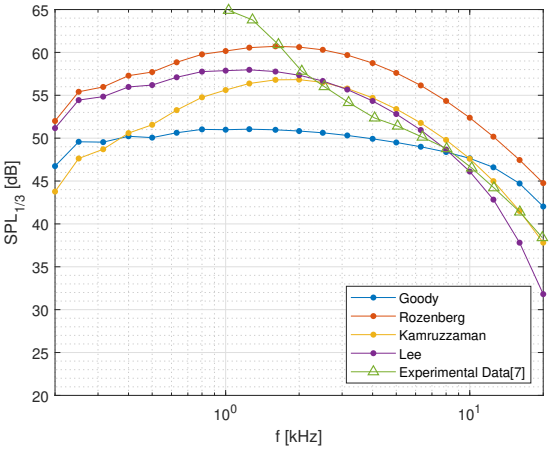

(b) Case 7:S_{ww} on the pressure side at 90% of the chord.

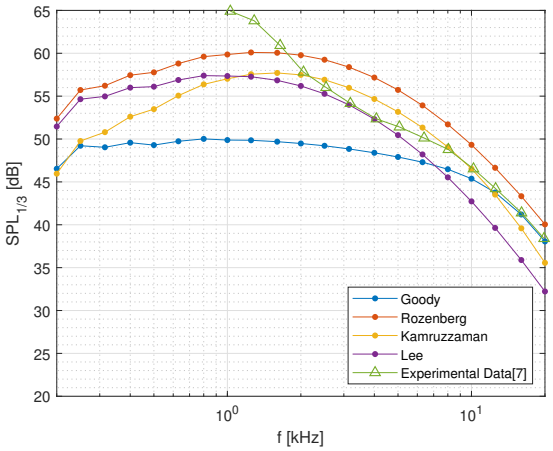

(c) Case 7:SPL at 95% of the chord.

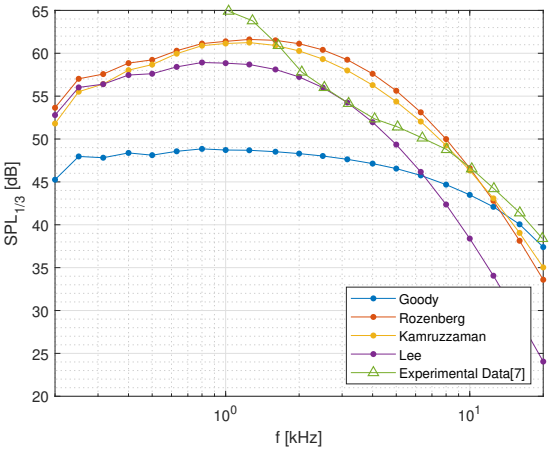

(d) Case 7:SPL at 98% of the chord.

Figure 6.3: Comparison of the PSD on the pressure (PS) and suction side (SS) at different chord position for DU96-W-180 airfoil.

Chapter 7

Sound directivity

The noise propagates in the air around the body surface in preferential directions. This property is defined as noise directivity and it can be calculated as ratio between the sound intensity in some direction and the theoretical intensity for a point source with the same sound power that radiates with a spherical wave front. However, the directivity graph, in polar coordinates, is complex to be obtained due to the difficulties in the evaluation of total power. For this reason it is possible to adopt a smarter approach that consists into defining the SPL at fixed frequencies and at different angle around the trailing edge, and introducing a reference value, like a mean intensity, as an approximation of the point source behavior. This approach was used also in reference [7] where the directivity was defined as ratio $p_{rms}/\bar{p}_{rms}$, where

$$\bar{p}_{rms} = \frac{1}{2\pi}\int_0^{2\pi} p_{rms}(\theta)\mathrm{d}\theta,$$

is the mean integration value of effective pressure. However, Amiet's theory allows to define the directivity only for the flat plate at zero incidence. For other incidence configurations, the polar graph is invariant. In literature, the directivity pattern was defined in a different way as

$$\frac{z}{\sigma}\left|\kappa c L\right|$$

. This solution comes from the pressure fluctuations in far field assumptions. In fact,

$$p(x,\omega) = -\frac{i\omega z L b}{2\pi c_0 \sigma^2}\frac{\sin\left(\frac{L}{2b}\left(\bar{K}_y - \frac{\bar{\kappa} y}{\sigma}\right)\right)}{\frac{L}{2b}\left(\bar{K}_y - \frac{\bar{\kappa} y}{\sigma}\right)} e^{i(\kappa/\beta^2)(\sigma - Mx)}\int_{-2}^{0} f(\bar{x}) e^{-iC\bar{x}}\mathrm{d}\bar{x}. \tag{7.1}$$

Two main alternatives for the directivity description are following proposed: the first approach consists into defining the directivity for the Amiet's theory as described in the previous chapters; the second approach is obtained using the Roger's formulation with scattering that allows to implement also the effect of limited span dimension (see Appendix B). Roger's formula improves also the acoustic prediction for the observer not in mid-span section and his solution collapses in the Amiet's formulation for $K_y = 0$, when the velocity is directed in chordwise direction. The main differences are evident due to the scattering terms that is zero only if the observe is located along z axis over the trailing edge. However, the directivity pattern shows a series of poles in variable number as

function of the frequency. For the observer position outside the mid-span section, finding valid experimental data is almost impossible and this configuration is neglected.

The directivity pattern is evaluated as function of dimensionless frequencies. The Helmhotz number is introduced as κc, where κ is the acoustic wave number and c the chord. As far as concern the dimensionless study, it is necessary to describe all possible cases, in terms of different behavior at frequencies and geometrical configuration. Furthermore, it is the most general description introduced. It is possible to note the directivity does not depends on the boundary quantities but only on Mach number,frequencies and the section plane of the observer.

The Amiet's solution has a directivity pattern very similar to a dipole source and slightly reclined in opposite direction of the airspeed. The maximum of emission is obtained for an angle θ more than 90, but its value strongly depends on the frequencies. At very low frequencies ($\kappa c = 0.25$), the lobes are elongated but they does not describe correctly the acoustic phenomena because they are orientated in airstream direction. Increasing the frequency, the lobes are deformed and the number of small peaks increases. Amiet's theory is almost limited in directivity description and it is not possible to establish in which way the prediction is coherent with the real emission.

For θ close to 160°, the curves in all figures are indented due to the numerical error introduced by the acoustic code. In fact, it is possible to demonstrate that, for both approaches, the formula presents a term in which the denominator tends to zero by growing the angle θ. In numerical solution, the problem was solved by introducing a better approximation of Fresnel Integrals by increasing the number of terms in Taylor series (see Appendix A). However, experimental measurements are not available and different models introduces similar directivity pattern. In all cases, as reference [7] demonstrates, the increasing frequency implies a more irregular pattern.

Roger's directivity patterns is defined as a classical dipole for a very low frequencies. The two curves, corresponding to the two models used, for $\kappa c = 0.25$, as presented in Figure 7.1(a), overlies for little angles. However, the two curves differs by increasing the frequencies. In Roger's solution many poles appear and the number or dimension is strictly function of the frequency. The directivity pattern is almost symmetrical on both sides of the profile. In Figure 7.1(b), κc assume unit value and the evolution of directivity poles is evident. The maximum emission occurs along $\theta = 100°$ direction for both approaches but Amiet's theory curve shows a lower level. The most interesting case is given by the figures 7.1(c) and 7.1(d), in which the shape of red curve differs from the blue one. For $140 < \theta < 180$, the graph is characterized by irregularities due to numerical approximation. The most evident phenomena consists into a large pole developed in opposite direction of airspeed that has the major part of the energy. This aspect is visible also for the highest value of κc, where the directivity pattern is a deformed dipole with a preferential direction along 160 while Roger's solution shows a series of small poles that increase in number at high frequencies.

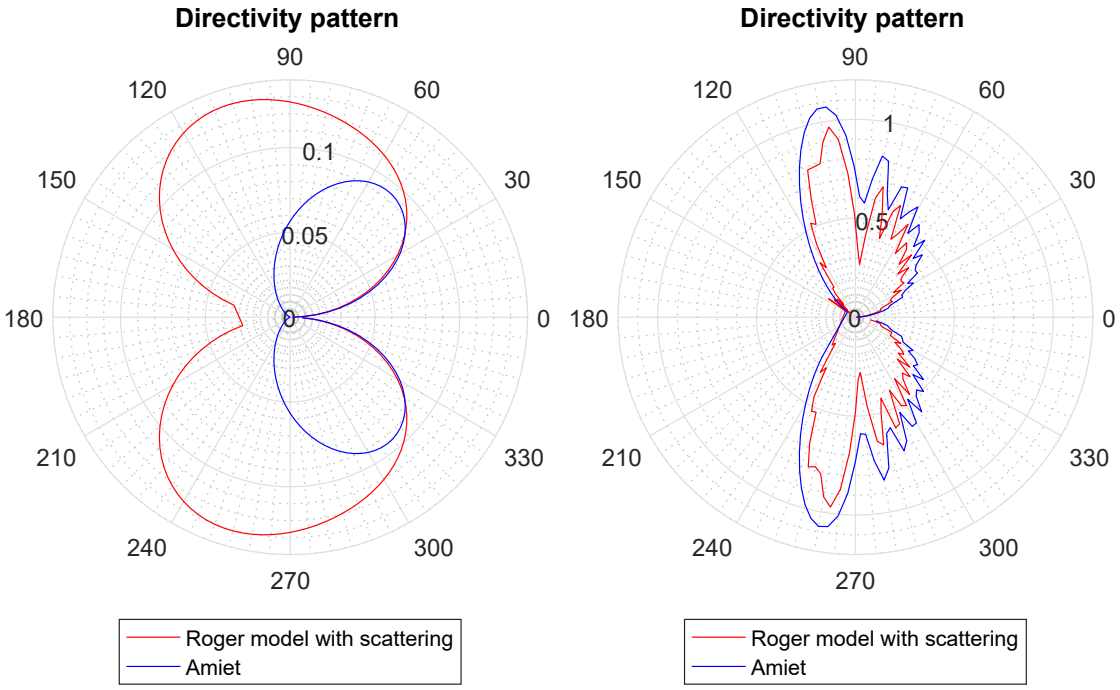

(a) Directivity Patterns for $\kappa c = 0.25$

(b) Directivity Patterns for $\kappa c = 1$

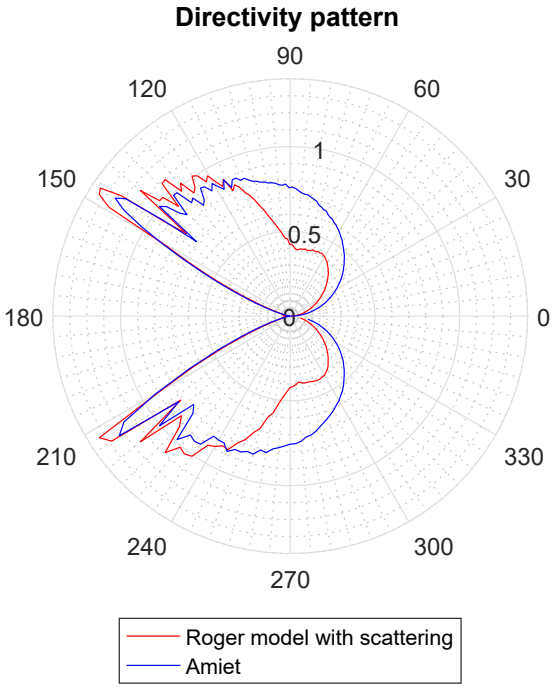

(c) Directivity Patterns for $\kappa c = 5$

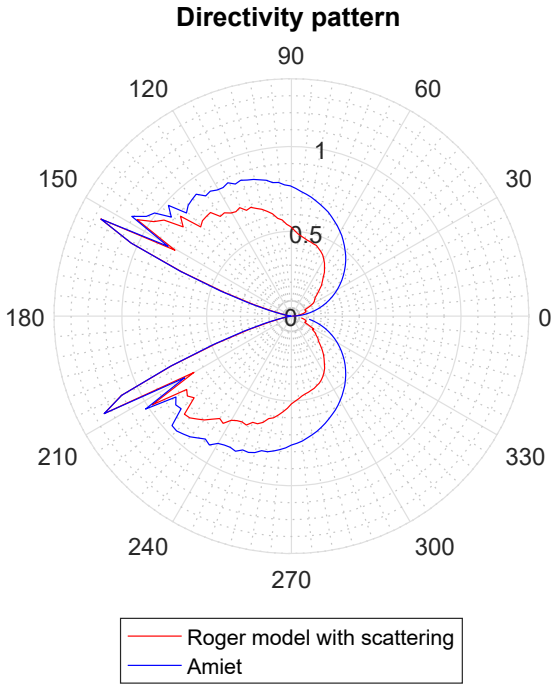

(d) Directivity Patterns for $\kappa c = 8$

Figure 7.1: Comparison of Directivity Patterns by Amiet's Theory and Roger's correction.

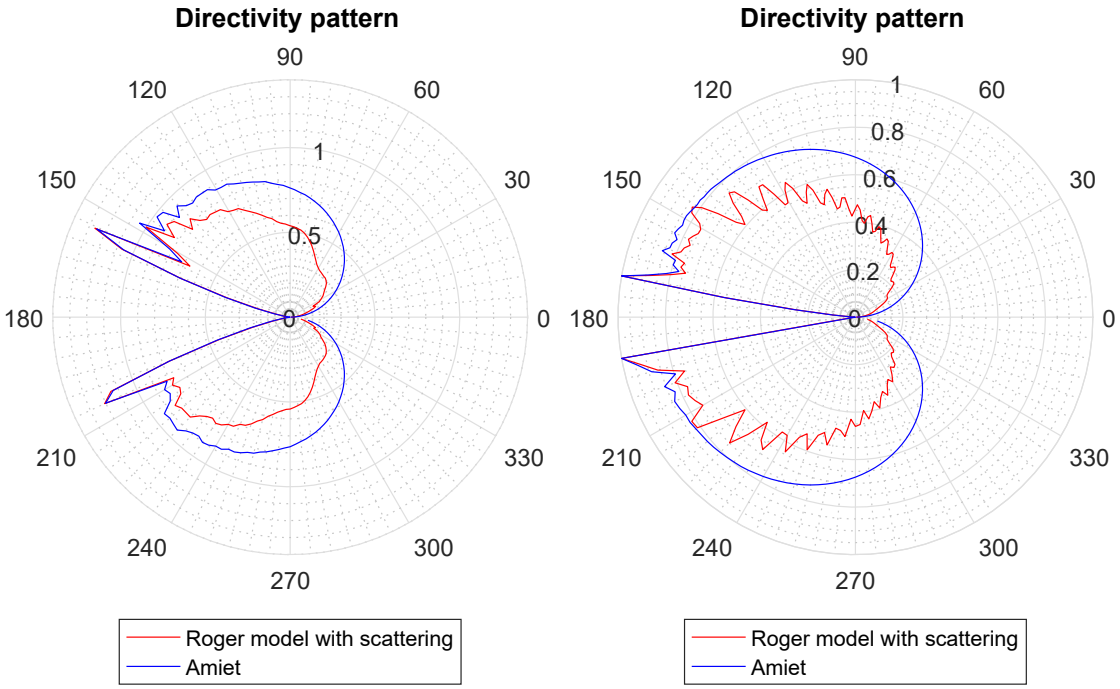

(a) Directivity Patterns for $\kappa c = 10$ (b) Directivity Patterns for $\kappa c = 50$

Figure 7.2: Comparison of Directivity Patterns by Amiet's Theory and Roger's correction.

Chapter 8

Sensitivity analysis of the acoustic model

Sensitivity approach allows to define which variables in the acoustic models mainly affects the output. According to the definition given in chapter 3, the global sensitivity indexes are computed as described by Saltelli et Al.[26] in order to establish how the single parameter and their combinations influences the results of the acoustic models. However, some advertising are necessary about which input quantities are considered and why they were chosen. In order to give a physical meaning of each input, RANS is not enough accurate because it is almost impossible repeating the simulations by modifying Reynolds or Mach number. Thus:

1. In order to introduce a variance in Reynolds and Mach, it is needed a LES (Large Eddies Simulation), that is not available in the present acoustic code. The purpose of sensitivity analysis is limited to a single RANS solution and the extrapolation of the boundary quantities is mainly affected by the mesh refining.

2. On the other hand, the time cost of the entire LES simulation is very expensive. And it contrasts with the purpose to find an alternative approach to reduce the computational cost.

A physical description is prohibitive. Hereinafter, all input quantities are supposed independent. It is a strong limitation and the models are released from the physical restrictions. In general, δ^* and θ are not independent and they both depends on the boundary thickness δ. Moreover, δ is the result of the fluid field around the airfoil and depends on Reynolds number. The friction coefficient c_f, in proximity of the trailing edge and the differential pressure $\mathrm{d}p/\mathrm{d}x$ are also input of the pressure spectrum models. The observer position and geometrical dimensions are supposed exact quantities; hence, they are neglected in sensitivity analysis.

Normal distribution function is applied for each input and the same variance is supposed for all quantities fixed. The global sensitivity indexes are calculated at various frequencies to understand if it influences the order of input importance. The influence of the angle of attack is not clearly discussed because its effect is hidden in the other

boundary quantities and it is not a direct input of the pressure spectra models.

A one-at-time discussion is not applied because it is limited on a single parameter effect, without considering any interactions between inputs. The first step is plotting the scatterplots for each models in order to compare, in qualitative ways, the effects of a single parameter. Secondly, Saletelli's method is applied. For this reason, Halton's sequence is used to extract pseudo-random points in number of 5000 units for all simulations. The same results can be obtained also with completely randomic points, with an higher computational cost, or Sobol's distribution.

8.1 Sensitivity analysis of Goody's model

Goody's model is the first introduced and the most simple pressure spectrum model to study. It is affected only by two inputs: the boundary thickness δ and the friction coefficient c_f. However, the pressure gradient does not participate in the model because Goody's formula was formulated for flat plate at zero incidence angle. In order to establish how input interviews in the sensitivity analysis, many tests are conducted at different variances and with a fixed frequency. The reference conditions used are summarized as case 1 in Table 5.1. In figure 8.1 are reported the scatterplots for δ and c_f at 1000 Hz and a variance of 20% of the mean value. From the figure, it is evident that the friction coefficient mainly affects the model output because the points show a stretched form in the plot. On the contrary, δ , which scatterplot is a cloud of points, does not affect the output. The c_f coefficient is the main parameter of the model and it has to be evaluated with an high resolution in order to reduce the error propagation. In fact, a little error in its calculus, improves a not negligible error in pressure spectrum analysis. The δ thickness is a direct function of the mesh dimension near the body wall. Therefore, the mesh sensitivity is very low and it is possible to obtain very similar results by using a larger mesh but enough accurate to reconstruct the stress distribution around the wall.

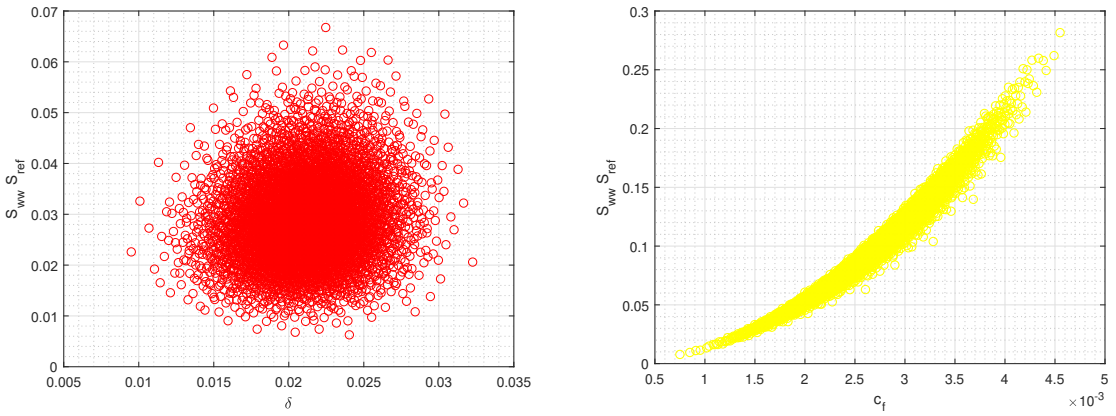

(a) Scatterplot of δ.

(b) Scatterplot of c_f.

Figure 8.1: Scatterplot analysis for Goody model

The first order global sensitivity factors are calculated and reported in the Table 8.1, in which the conclusion that comes out from the scatterplots analysis is confirmed. Moreover, the S_{c_f} is very close to one (about 0.98 in all configuration) while S_δ is almost null; thus, δ effect can be neglected. The model is nonadditive. In fact, the sum of first order indexes is lower than one, while the sum of total factors is bigger than the unit, as concerned the theory. The total indexes are always bigger than the equivalent first order factors and this demonstrates the number of points used in Monte Carlo method is enough to guarantee a correct sensitivity evaluation. The test is repeated for different variances but the hierarchy of the input is invariant. However, at constant frequency, the sensitivity factor S_{c_f} declines a little. Growing the input variances,the spectrum level becomes negative and this is not physically possible.

Increasing the frequency has not relevant effects on sensitivity indexes and they appear almost constant. At very low frequencies, δ acquires importance but it is always less than 1%.

The output distribution function is not more a normal distribution, as assumed to be for the input parameters. It is shown in Figure 8.2, where the curves are obtained at different frequencies. Even if the distribution appear similar, the scales are different. At high frequency the curve has a very thin peak around the mean value and the variance plummets. The output variance σ_y is about 0.03898, that corresponds to 39% of the mean output value, and skewness 0.5745 for 1000 Hz that corresponds to a medium frequency; while they assume 0.00114 and 0.5764 respectively, for $f = 5000$ Hz. The model is more rigid at high frequencies for which it is possible to tolerate higher input error level.

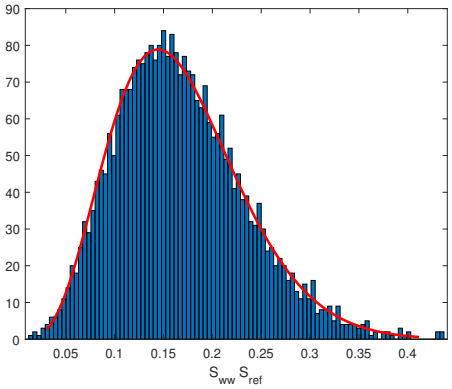

(a) Probability distribution function for f = 100 Hz.

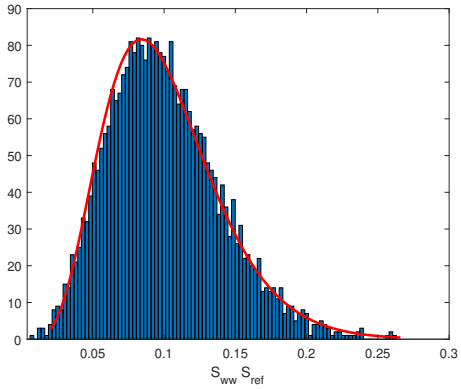

(b) Probability distribution function for f = 1000 Hz.

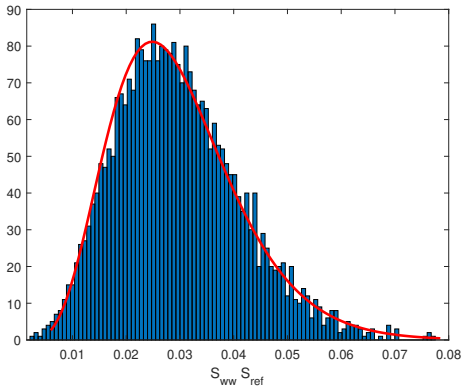

(c) Probability distribution function for f = 5000 Hz.

Figure 8.2: Goody's probability distribution function at various frequencies and fixed input variance 0.2.

Goody's model:global sensitivity factors					Frequency	100 Hz		
Var 0.1	S_i	S_{T_i}	Va 0.15	S_i	S_{T_i}	Var 0.2	S_i	S_{T_i}
δ	0.0300	0.0430	δ	0.0332	0.0445	δ	0.0367	0.0492
c_f	0.9627	0.9707	c_f	0.9591	0.9678	c_f	0.9534	0.9644
Sum	0.9927	1.0137	Sum	0.9923	1.0123	Sum	0.9901	1.0136
					Frequency	1000 Hz		
Var 0.1	S_i	S_{T_i}	Var 0.15	S_i	S_{T_i}	Var 0.2	S_i	S_{T_i}
δ	0.0106	0.0227	δ	0.0127	0.0221	δ	0.0146	0.0236
c_f	0.9830	0.9899	c_f	0.9814	0.9879	c_f	0.9749	0.9862
Sum	0.9936	1.0126	Sum	0.9941	1.01	Sum	0.9895	1.0098
					Frequency	5000 Hz		
Var 0.1	S_i	S_{T_i}	Var 0.15	S_i	S_{T_i}	Var 0.2	S_i	S_{T_i}
δ	0.0081	0.0201	δ	0.0101	0.0192	δ	0.0118	0.0203
c_f	0.9855	0.9924	c_f	0.9842	0.9905	c_f	0.9822	0.9890
Sum	0.9936	1.0125	Sum	0.9943	1.0108	Sum	0.994	1.0093
					Frequency	10000 Hz		
Var 0.1	S_i	S_{T_i}	Var 0.15	S_i	S_{T_i}	Var 0.2	S_i	S_{T_i}
δ	0.0074	0.0194	δ	0.0094	0.0184	δ	0.0109	0.0194
c_f	0.9863	0.9931	c_f	0.9850	0.9913	c_f	0.9831	0.9898
Sum	0.9937	1.0125	Sum	0.9944	1.0097	Sum	0.994	1.0092

Table 8.1: Table of global sensitivity factors at different frequencies and variance for Goody's model

8.2 Sensitivity analysis of Rozenberg's model

Rozenberg's model introduces the pressure gradient effect for the calculus of pressure spectrum. For this reason, the term $\mathrm{d}p/\mathrm{d}x$ is the main input that distinguish the present model from the Goody's one. The boundary quantities δ^* and θ are hidden in the model formula. The boundary thickness δ and c_f coefficient complete the range of model's input.

In order to graph the scatterplots, the frequency is fixed to 1000 Hz and variance 20% for all parameters. From the Figure 8.3(c) it is possible to affirm that δ is the less influential input. However, the friction coefficient c_f and momentum thickness θ are the two main parameters that more influences the model output. Even if the pressure gradient is most characteristic input of the model, its uncertainty does not propagates in the model.

Global sensitivity factors are summarized in Table 8.2. For $f = 100$ Hz, the friction coefficient is the most influential parameter, while the error for θ and $\mathrm{d}p/\mathrm{d}x$ do not influences the outputs due to their little sensitivity factor about 0.02. The global sensitivity indexes slightly change with the variance. However, the indexes for c_f decreases while the indexes for δ grows. The boundary thickness becomes the most important parameter. Very low frequencies have only academic importance and they does not describe the real acoustic phenomena. By increasing the frequency, the c_f remains the main parameter but the sum of the first order global sensitivity parameters falls. The pressure gradient and

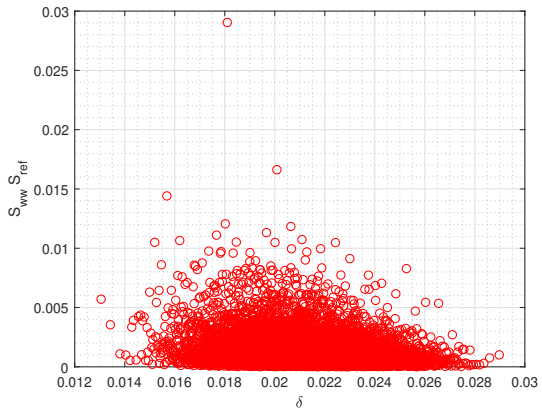

(a) Scatterplot of δ.

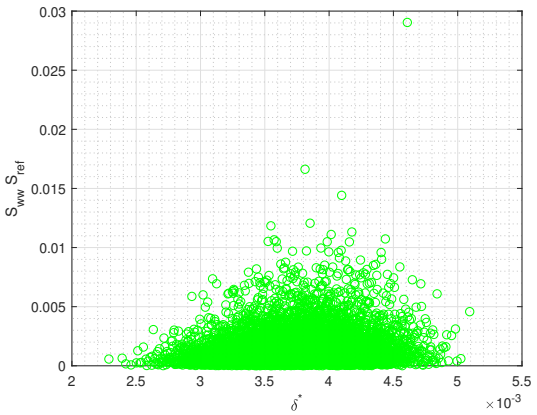

(b) Scatterplot of δ^*.

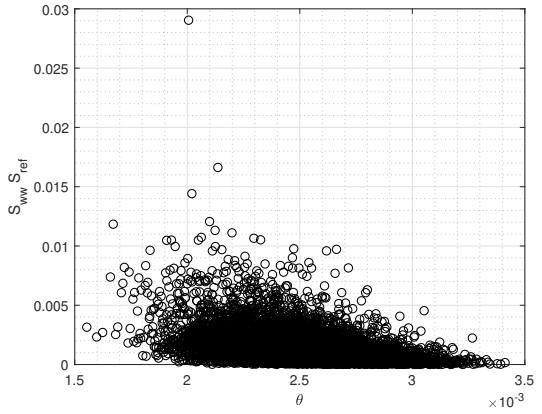

(c) Scatterplot of θ.

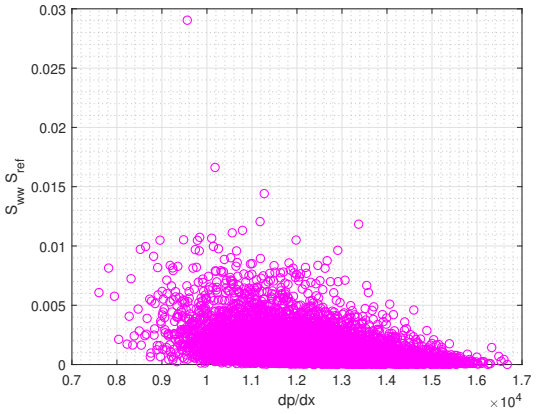

(d) Scatterplot of $\mathrm{d}p/\mathrm{d}x$.

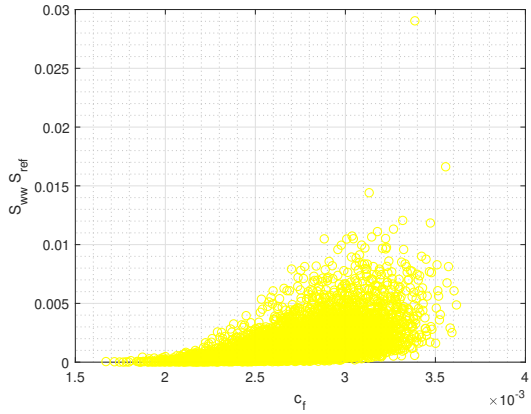

(e) Scatterplot of c_f.

Figure 8.3: Scatterplot analysis for Rozenberg's model

θ acquire importance and they are the second main parameters in the input hierarchy. However, Saltelli's algorithm does not allows to compute the second order factors and they are neglected in following sections. In respect of the Goody's model, Rozenberg proposed an algorithm that does not depend on the δ thickness(δ it is almost insignificant) but it is mainly built on c_f, $\mathrm{d}p/\mathrm{d}x$ and θ.

For high frequency (5000 Hz), the model distribution function assume a decreasing exponential trend. The skewness is very high, corresponding to 6.16 and variance $5.10\,10^{-5}$. The frequency modifies the distribution function that assumes a normal shape for very low frequencies. From lowest to the highest frequency, it gradually exhibits increasing skewness and a gamma distribution law. In Figure 8.4 are compared the distribution function for $f = 100$ Hz, $f = 1000$ Hz and $f = 5000$ Hz, with fixed variance equal to 0.2 of the mean value. The skweness comes from 3.4 for $f = 100$ Hz, to 6.16 for high frequencies. Also putput variance is frequency dependent: it varies from 0.15 of mean value for low frequencies to 0.0038469 at 1000 Hz. Rozenberg's model is the most robust of the present study.

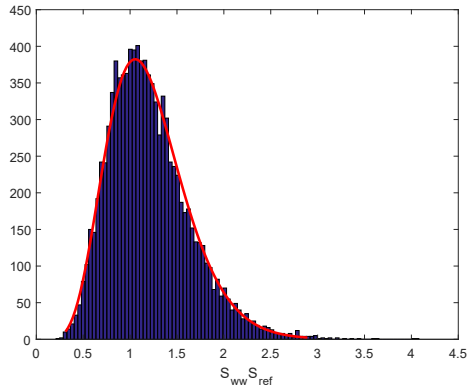

(a) Probability distribution function for $f = 100$ Hz.

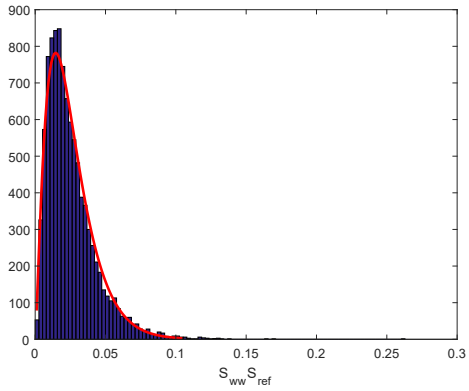

(b) Probability distribution function for $f = 1000$ Hz.

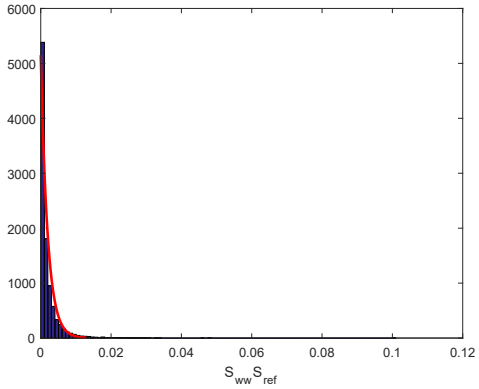

(c) Probability distribution function for $f = 5000$ Hz.

Figure 8.4: Rozenberg's probability distribution function at various frequencies and fixed input variance.

8.3 Sensitivity analysis of Kamruzzaman's model.

Kamruzzaman's model is the most accurate model for the acoustic phenomena. However, it depends on boundary quantities δ^* and θ, on the friction coefficient c_f and pressure gradient. The boundary thickness does not influences the model. In Figure 8.5 are presented the scatterplots for $f = 1000$ Hz . The main influential input is still the friction coefficient. It is evident from the Figure 8.5(d) where the graph shows an elongated point distribution. However, also δ^* is an important input, while θ and $\mathrm{d}p/\mathrm{d}x$ are less significant input. From the Table 8.3, this aspect is confirmed. Both first order or total sensitivity factors slightly depend on the frequency while they remain almost constant by increasing the variance. S_{c_f} assumes the maximum value at low frequencies and minimum variance (about 0.7843), while the second major contribution is S_{δ^*} with about 0.18. The parameters θ and $\mathrm{d}p/\mathrm{d}x$ are not significant for the model due to the little sensitivity indexes. By increasing the frequency, the indexes S_θ and S_{dp} fall and they become almost zero (see the case for $f = 5000$ Hz).

Then, a comparison between Rozenberg's model and Kamruzzaman's one is necessary. The friction coefficient c_f is the main sensible input for both models. However, the weight of the single term is different. Indeed the inputs are the same, in Kamruzzaman's approach the order of importance is invariant with the frequency.
The sum of the S_i is very close to one; thus the second order or more are not required and the first order factors are able to recover almost the totality of the output variance influence.

Kamruzzaman's distribution function is reported in Figure 8.6. The shape is not more a normal distribution. The variance highly depends on frequency. At $f = 1000$ Hz it is about $1.17\,10^{-6}$, that is $4.72\,10^{-4}$ times the mean output, and skewness 1.3.

8.4 Sensitivity analysis of Lee's model

Lee's model is the last proposed approach that improves goody's model for non symmetrical airfoils. The input quantities are the same considered for the Kamruzzaman's model. Scatterplots are drawn in Figure 8.7. However, all figures present an elongated shape similar to the figure obtained for Rozenberg's approach. The most sensible inputs are the friction coefficient c_f and the pressure gradient, while the boundary quantities show a more regular distribution of points.

The probability function is plotted in Figure 8.8. However, in respect of Goody's model or Rozenberg's one, the figure appears more peaked around the zero value. The output distribution function is characterized by a gamma law with very small variance and high skweness. The distribution law slightly depends on frequency. The high frequency is synonymous of increasing robustness of the model. At medium frequencies the variance is about $3.32\,10^{-5}$ and skewness 1.924. The variance falls with increasing frequency until $1.78\,10^{-7}$ at 5000 Hz.

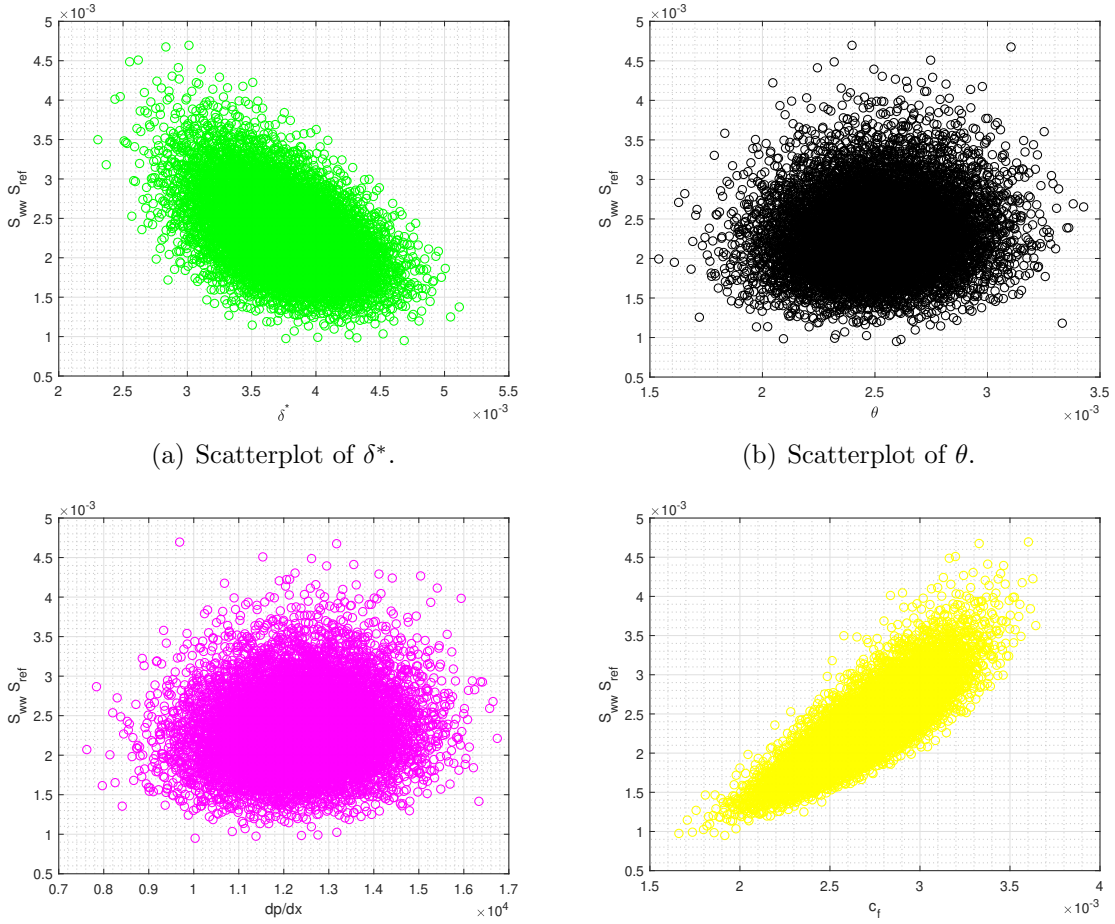

(a) Scatterplot of δ^*.

(b) Scatterplot of θ.

(c) Scatterplot of $\mathrm{d}p/\mathrm{d}x$.

(d) Scatterplot of c_f.

Figure 8.5: Scatterplot analysis for Kamruzzaman's model

The global sensitivity indexes are summarized in the Table 8.4. For very low frequency the variance seriously affects the importance hierarchy and δ becomes the most influencing parameter with $S_\delta = 0.3695$ for variance 0.2, versus $S_{c_f} = 0.3270$. Thus, if the uncertainty on the measured quantities raises, the order of importance changes. For $f = 1000$ Hz, the influence of friction coefficient gradually decreases and the sum of first order global index is very less than one. The total factors have inside the higher order indexes, thus high S_{T_i} value is symptomatic of high second order contribution. In present case, indeed the c_f is not always the main influencing parameter, the corresponding total index assumes the maximum value. Hence, the combination of c_f and other input has not negligible weight. The index S_{c_f} comes from 0.4721 for low frequency and variance to 0.20 at high frequency and variance. In general, increasing the variance induces a reduction of c_f influence. In all combination of frequencies and variance, δ^* is the less influential parameter while θ and $\mathrm{d}p/\mathrm{d}x$ have the same weight. The hierarchy does not change if total indexes are considered. Finally, it is important to note that the sum of first order indexes falls while the sum of total factors arises.

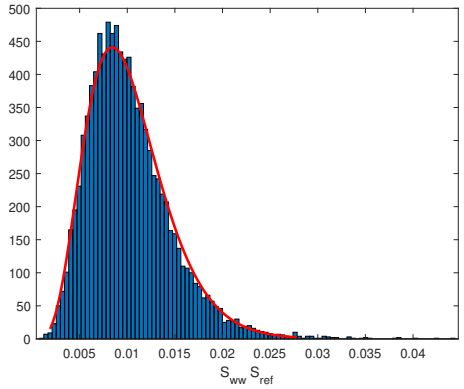

(a) Probability distribution function for f = 100 Hz.

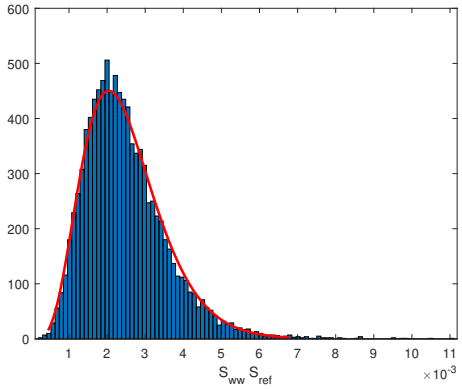

(b) Probability distribution function for f = 1000 Hz.

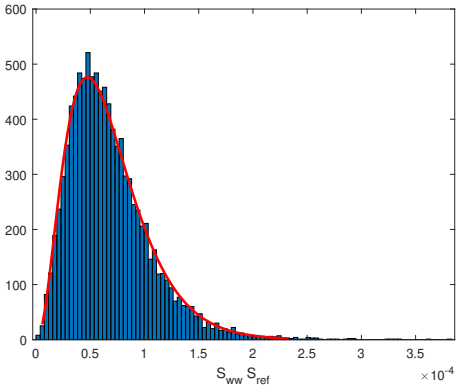

(c) Probability distribution function for f = 5000 Hz.

Figure 8.6: Kamruzzaman's model probability distribution function at various frequencies and fixed input variance 0.2.

For high frequencies δ and δ^* are not influent and their effect can be neglected in PSD model. It eases the noise prediction because of computational cost and errors reducing in θ or c_f measurement. The weight of the single factor decreases while the total effect increases.

8.5 Sensitivity analysis conclusion

The sensitivity study consists into three main steps: definition of a pseudo-random points in order to cover the entire range of variability of the quantities for which the normal distribution is supposed; elaborating of the scatterplots as a first evaluation of model sensitivity and then the calculus of first order global sensitivity indexes according to Saltelli's proposed algorithm. All input are considered independent although the physical quantities are functions of Reynolds and Mach. Reynolds and Mach are the main input for RANS simulation.

In conclusion, the friction coefficient c_f is the most influent input for all models, particularly for the Goody's one where it influences output variance for over 98% percent. Furthermore, the S_{c_f} is not constant for all models and it depends on input variance and frequency. S_{c_f} varies from about 0.14 for Rozenberg's model at high frequencies and high variance, until to reach 0.75 for Kamruzzaman's approach at low frequency and variance. The total factors allows to introduce also the effect of combination between input variables. In each cases, the index associated to friction is the highest one. This implies that also its second or higher order index has not negligible effects on the output models.

The hierarchy of input importance in not in advance predicted. For Kamruzzaman's model the effects of pressure gradient and θ are negligible while δ^* assume a greater importance with a global factor around 0.22 that increases at high frequencies. Rozenberg's and Lee's algorithms are not influenced by δ^*, thus the attention has to be directed towards the correct extrapolation of pressure gradient and momentum thickness.

The distribution function has almost the same shape for all models and it depends on frequency. Obviously, the mean values, output variances and skewness are different from a model to another. In general, at high frequencies the variance decreases while the skewness raises. Hence all models show to be more robust at high frequencies.

Rozenberg's model:global sensitivity factors					Frequency	100 Hz		
Var 0.1	S_i	S_{T_i}	Var 0.15	S_i	S_{T_i}	Var 0.2	S_i	S_{T_i}
δ	0.2879	0.3124	δ	0.3113	0.3608	δ	0.3670	0.4492
δ^*	0.1660	0.1805	δ^*	0.1561	0.2007	δ^*	0.1394	0.2180
θ	0.0188	0.0262	θ	0.0160	0.0221	θ	0.0119	0.0172
$\mathrm{d}p/\mathrm{d}x$	0.0188	0.0261	$\mathrm{d}p/\mathrm{d}x$	0.0162	0.0216	$\mathrm{d}p/\mathrm{d}x$	0.0124	0.0149
c_f	0.4755	0.4969	c_f	0.4309	0.4768	c_f	0.3585	0.4337
Sum	0.967	1.042	Sum	0.9305	1.082	Sum	0.9901	1.0136
					Frequency	1000 Hz		
Var 0.1	S_i	S_{T_i}	Var 0.15	S_i	S_{T_i}	Var 0.2	S_i	S_{T_i}
δ	0.1258	0.1802	δ	0.1398	0.2442	δ	0.2152	0.3684
δ^*	0.0431	0.0828	δ^*	0.0389	0.1138	δ^*	0.0312	0.1161
θ	0.1517	0.2029	θ	0.1317	0.2140	θ	0.1005	0.1760
$\mathrm{d}p/\mathrm{d}x$	0.1529	0.1998	$\mathrm{d}p/\mathrm{d}x$	0.1325	0.2141	$\mathrm{d}p/\mathrm{d}x$	0.1012	0.1904
c_f	0.4256	0.5009	c_f	0.3575	0.4994	c_f	0.2708	0.4351
Sum	0.8991	1.166	Sum	0.8004	1.2855	Sum	0.7189	1.286
					Frequency	5000 Hz		
Var 0.1	S_i	S_{T_i}	Var 0.15	S_i	S_{T_i}	Var 0.2	S_i	S_{T_i}
δ	0.0573	0.1453	δ	0.0570	0.2205	δ	0.0847	0.3066
δ^*	0.0161	0.890	δ^*	0.0114	0.1495	δ^*	0.0066	0.1826
θ	0.1922	0.3214	θ	0.1641	0.3777	θ	0.1350	0.3956
$\mathrm{d}p/\mathrm{d}x$	0.1909	0.3218	$\mathrm{d}p/\mathrm{d}x$	0.1597	0.3847	$\mathrm{d}p/\mathrm{d}x$	0.1303	0.4120
c_f	0.3382	0.5099	c_f	0.2491	0.5432	c_f	0.1762	0.5340
Sum	0.7947	1.042	Sum	0.6413	1.6756	Sum	0.5328	1.8308
					Frequency	10000 Hz		
Var 0.1	S_i	S_{T_i}	Var 0.15	S_i	S_{T_i}	Var 0.2	S_i	S_{T_i}
δ	0.0413	0.1471	δ	0.0385	0.2314	δ	0.0507	0.2978
δ^*	0.0103	0.1016	δ^*	0.0057	0.1783	δ^*	0.0019	0.2211
θ	0.1974	0.3671	θ	0.1664	0.4413	θ	0.1408	0.4716
$\mathrm{d}p/\mathrm{d}x$	0.1934	0.3696	$\mathrm{d}p/\mathrm{d}x$	0.1573	0.4507	$\mathrm{d}p/\mathrm{d}x$	0.1313	0.4831
c_f	0.2996	0.5210	c_f	0.2046	0.5677	c_f	0.1396	0.5717
Sum	0.742	1.5063	Sum	0.5727	1.6756	Sum	0.5328	1.8308

Table 8.2: Table of global sensitivity factors at different frequencies and variance for Rozenber's model.

Kamruzzaman's model:global sensitivity factors					Frequency	100 Hz		
Var 0.1	S_i	S_{T_i}	Var 0.15	S_i	S_{T_i}	Var 0.2	S_i	S_{T_i}
δ^*	0.1788	0.2203	δ^*	0.1887	0.2298	δ^*	0.1969	0.2469
θ	0.0065	0.0276	θ	0.0081	0.0264	θ	0.0086	0.0266
$\mathrm{d}p/\mathrm{d}x$	0.0071	0.0296	$\mathrm{d}p/\mathrm{d}x$	0.0089	0.0279	$\mathrm{d}p/\mathrm{d}x$	0.0096	0.0278
c_f	0.7843	0.7849	c_f	0.7691	0.7772	c_f	0.7502	0.7694
Sum	0.9767	1.0624	Sum	0.9748	1.0613	Sum	0.9653	1.0707
					Frequency	1000 Hz		
Var 0.1	S_i	S_{T_i}	Var 0.15	S_i	S_{T_i}	Var 0.2	S_i	S_{T_i}
δ^*	0.2445	0.2835	δ^*	0.2657	0.3072	δ^*	0.2992	0.3561
θ	0.0076	0.0236	θ	0.0048	0.0237	θ	0.0043	0.0282
$\mathrm{d}p/\mathrm{d}x$	0.0082	0.0254	$\mathrm{d}p/\mathrm{d}x$	0.0060	0.0244	$\mathrm{d}p/\mathrm{d}x$	0.0055	0.0288
c_f	0.7184	0.7274	c_f	0.6906	0.7098	c_f	0.6422	0.6809
Sum	0.9787	1.0600	Sum	0.9671	1.0651	Sum	0.9512	1.094
					Frequency	5000 Hz		
Var 0.1	S_i	S_{T_i}	Var 0.15	S_i	S_{T_i}	Var 0.2	S_i	S_{T_i}
δ^*	0.2362	0.2700	δ^*	0.2575	0.300	δ^*	0.2936	0.3566
θ	0.0009	0.0190	θ	0.0019	0.0189	θ	0.0016	0.0253
$\mathrm{d}p/\mathrm{d}x$	0.0016	0.0194	$\mathrm{d}p/\mathrm{d}x$	0.0026	0.0191	$\mathrm{d}p/\mathrm{d}x$	0.0022	0.0255
c_f	0.7360	0.7462	c_f	0.7033	0.7271	c_f	0.6474	0.6949
Sum	0.9747	1.0546	Sum	0.9653	1.0651	Sum	0.9448	1.1023
					Frequency	10000 Hz		
Var 0.1	S_i	S_{T_i}	Var 0.15	S_i	S_{T_i}	Var 0.2	S_i	S_{T_i}
δ^*	0.2275	0.2719	δ^*	0.2528	0.3217	δ^*	0.3043	0.4059
θ	0.0023	0.0201	θ	0.0035	0.0268	θ	0.0041	0.0438
$\mathrm{d}p/\mathrm{d}x$	0.0025	0.0206	$\mathrm{d}p/\mathrm{d}x$	0.0038	0.0273	$\mathrm{d}p/\mathrm{d}x$	0.0044	0.0447
c_f	0.7417	0.7539	c_f	0.6905	0.7371	c_f	0.6052	0.6910
Sum	0.974	1.0665	Sum	0.9506	1.1129	Sum	0.918	1.1854

Table 8.3: Table of global sensitivity factors at different frequencies and variance for Kamruzzaman's model.

Lee's model:global sensitivity factors					Frequency	100 Hz		
Var 0.1	S_i	S_{T_i}	Var 0.15	S_i	S_{T_i}	Var 0.2	S_i	S_{T_i}
δ	0.2772	0.3055	δ	0.3038	0.3646	δ	0.3695	0.4814
δ^*	0.1353	0.1955	δ^*	0.1274	0.1808	δ^*	0.1080	0.2285
θ	0.0345	0.0431	θ	0.0267	0.0442	θ	0.0143	0.0586
$\mathrm{d}p/\mathrm{d}x$	0.0342	0.0440	$\mathrm{d}p/\mathrm{d}x$	0.0269	0.0442	$\mathrm{d}p/\mathrm{d}x$	0.0149	0.0596
c_f	0.4721	0.5068	c_f	0.4210	0.4912	c_f	0.3270	0.4696
Sum	0.9533	1.095	Sum	0.9058	1.125	Sum	0.8337	1.2977
					Frequency	1000 Hz		
Var 0.1	S_i	S_{T_i}	Var 0.15	S_i	S_{T_i}	Var 0.2	S_i	S_{T_i}
δ	0.1053	0.1589	δ	0.1169	0.2248	δ	0.1817	0.3358
δ^*	0.0316	0.0678	δ^*	0.0275	0.0975	δ^*	0.0225	0.1265
θ	0.1626	0.2226	θ	0.1420	0.2509	θ	0.1150	0.2516
$\mathrm{d}p/\mathrm{d}x$	0.1625	0.2251	$\mathrm{d}p/\mathrm{d}x$	0.1420	0.2502	$\mathrm{d}p/\mathrm{d}x$	0.1158	0.2396
c_f	0.4080	0.4978	c_f	0.3375	0.5002	c_f	0.2574	0.4744
Sum	0.87	1.1722	Sum	0.7659	1.3236	Sum	0.6924	1.4279
					Frequency	5000 Hz		
Var 0.1	S_i	S_{T_i}	Var 0.15	S_i	S_{T_i}	Var 0.2	S_i	S_{T_i}
δ	0.0443	0.1170	δ	0.0437	0.1891	δ	0.0630	0.2821
δ^*	0.0095	0.0620	δ^*	0.0059	0.1080	δ^*	0.0040	0.1372
θ	0.1900	0.3299	θ	0.1609	0.3978	θ	0.1374	0.4305
$\mathrm{d}p/\mathrm{d}x$	0.1905	0.3382	$\mathrm{d}p/\mathrm{d}x$	0.1614	0.4026	$\mathrm{d}p/\mathrm{d}x$	0.1380	0.4161
c_f	0.3237	0.4940	c_f	0.2369	0.5172	c_f	0.1720	0.5156
Sum	0.758	1.3411	Sum	0.6088	1.6067	Sum	0.5144	1.7815
					Frequency	10000 Hz		
Var 0.1	S_i	S_{T_i}	Var 0.15	S_i	S_{T_i}	Var 0.2	S_i	S_{T_i}
δ	0.0325	0.1108	δ	0.0365	0.1820	δ	0.0634	0.2711
δ^*	0.0058	0.0639	δ^*	0.0053	0.0979	δ^*	0.0067	0.0893
θ	0.1884	0.3573	θ	0.1505	0.4009	θ	0.1079	0.3877
$\mathrm{d}p/\mathrm{d}x$	0.1895	0.3673	$\mathrm{d}p/\mathrm{d}x$	0.1529	0.4007	$\mathrm{d}p/\mathrm{d}x$	0.1127	0.3612
c_f	0.3006	0.5040	c_f	0.2379	0.5471	c_f	0.2057	0.5717
Sum	0.7168	1.4033	Sum	0.5831	1.6286	Sum	0.4964	1.681

Table 8.4: Table of global sensitivity factors at different frequencies and variance for Lee's model

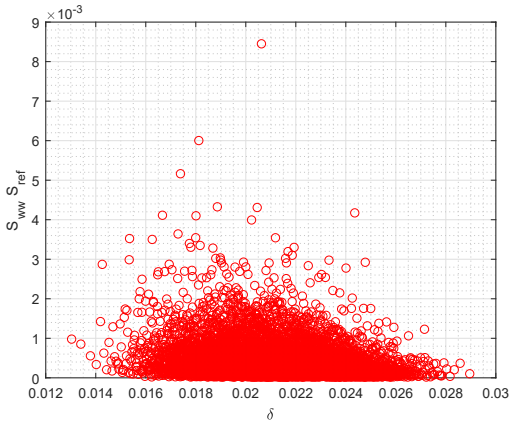

(a) Scatterplot of δ.

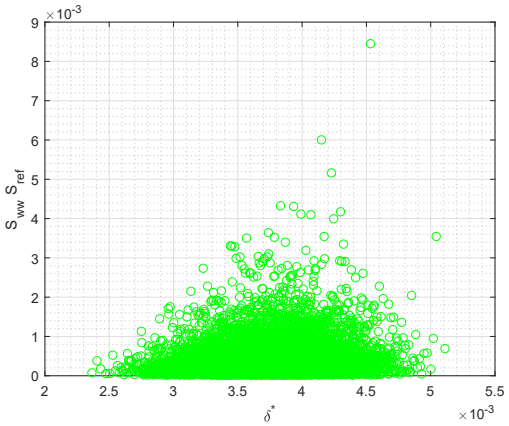

(b) Scatterplot of δ^*.

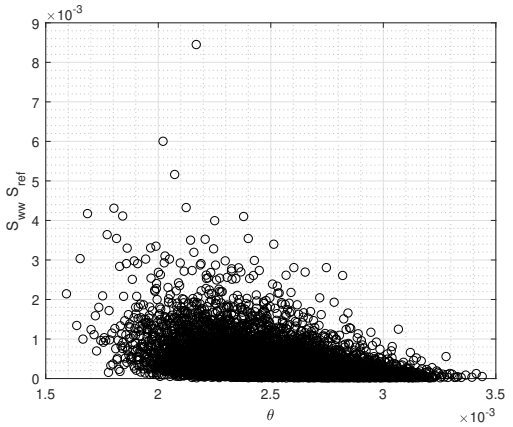

(c) Scatterplot of θ.

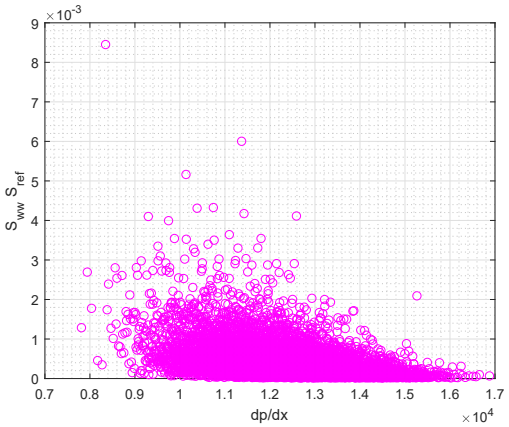

(d) Scatterplot of $\mathrm{d}p/\mathrm{d}x$.

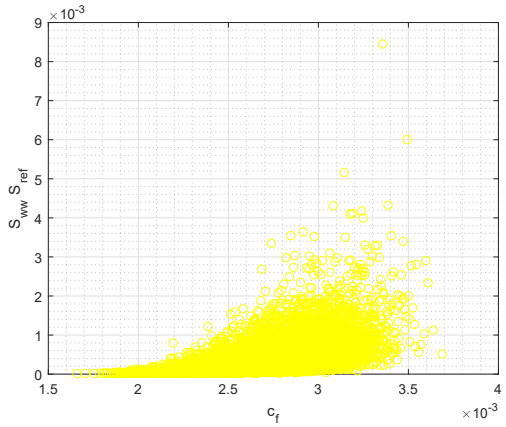

(e) Scatterplot of c_f.

Figure 8.7: Scatterplot analysis for Lee's model

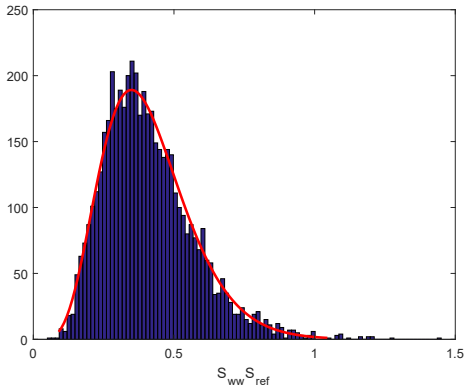

(a) Probability distribution function for $f = 100$ Hz.

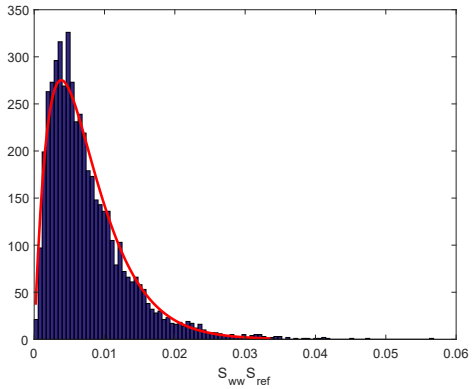

(b) Probability distribution function for $f = 1000$ Hz.

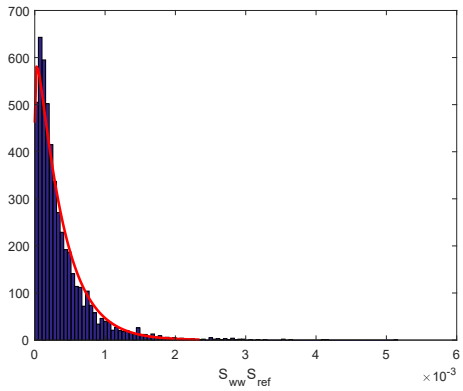

(c) Probability distribution function for $f = 5000$ Hz.

Figure 8.8: Lee's probability distribution function at various frequencies and fixed input variance.

Chapter 9

Conclusions

The approach proposed in the present work is an example of hybrid method used in aeroacoustics to predict the noise radiated by airfoil immersed into turbulent flow. Amiet's formula allows to predict the trailing edge noise due to interaction of turbulent flow at high Reynolds and low Mach number (uncompressible fluid). Although the Amiet's theory was elaborated for infinite chord flat plate, it is still an important reference for the broadband noise prevision also for thin airfoil with finite chord.

The first step is solving the RANS equations for a certain geometry and the second one consists into the boundary extrapolation of the boundary quantities in proximity of the trailing edge. The isentropic velocity was introduced in order to compute the boundary thickness from the velocity profile. The RANS solution returns δ^*/c and θ/c that were compared with reference data. The two values shows errors that depends on geometry and chordwise position. For NACA0012 the error is always lower than 5% and it decreases near the trailing edge; while the DU96-W-180 profile shows many problems. The difference between computed and reference conditions often assumes 10% error and it barely depends on the extrapolation position. Except for the $x/c = 80\%$, in which the error is very high, indeed the shape factor H is almost the same, the other cases studied present acceptable error. Furthermore, some differences are evident between suction and pressure side. The pressure side generally shows higher error. This influences the acoustic results and it produces a growing predicted emission. Although the not perfect correspondence with reference boundary quantities, the acoustic model produces a good approximation. Very close the trailing edge, the errors between the reference and computed quantities decreases.

Different semi-empirical models are introduced in order to improve the pressure spectrum. Thus, Goody's model is the first described but it was developed for a flat plate. For this reason, from the comparison with the experimental data available, Goody's model is not able to reproduce the acoustic phenomena despite the variability of cases analyzed. Moreover, the boundary layer extrapolation position does not significantly influences the Goody's prediction as well as the angle of attack. The predicted level is always limited around 40 dB and the curves appear almost flat on the entire frequency range. The same trend is found for both geometries.

Lee's model highly depends on the airfoil shape. The model was introduced in order to adapt the Amiet's formula for asymmetrical geometries. In fact, it returns good results for DU96-W-180 profile, where the prediction overlies the experimental data for a short frequency interval. The extrapolation point and the angle of incidence modify the accuracy of the model. However, it introduces a bad prediction for NACA0012 profile for all cases studied.
Rozenberg's and Kamruzzaman's models are the most accurate. However, the accuracy mainly depends on geometry and incidence. For NACA0012 airfoil, Kamruzzaman's prediction has good agreement with the experimental data for zero incidence configuration. The chord dimension and Reynolds number does not affect the acoustic results. The error introduced is almost acceptable for a large range of frequencies. For zero incidence and case 2, the yellow curve remarks the experimental points and the error is reduced till 2 dB. For the case 5 and 6, the graph does not follow the experimental trend and the differences are about 6 dB or more. However, the frequency peak is well predicted. Kamruzzaman's model is conservative in many cases and it should be very useful in preliminary project phase. For DU96-W-180 profile,Kamruzzaman's model is still the most accurate. At 90% of the chord, the boundary layer quantities allows to reproduce correctly the acoustic emission. However, the peak is not predicted because the model reproduce only the broadband noise.
Rozenberg's model is the most accurate for high angle of attack. For NACA0012 profile, in case 5 and 6 it has a good agreement with experimental data with 3 dB as maximum error for medium frequencies. The choice of boundary position influences highly the accuracy mainly for high frequencies where the curve decreases rapidly. However, the central frequencies need great attention because they are the most sensitive range for human hear. On the other hand, choosing a position of 95% of the chord allows a better approximation on the entire frequency range. The DU96-W-180 airfoil solution shows the highest error in respect to the experimental data. For this reason, Rozenberg's model is not adapted for the acoustic purpose.

The question about the most accurate pressure spectra model has not univocal answer and it depends on many factors: geometry, angle of attack and extrapolation point. The Mach number is little influential for not compressible flow; while the main parameter is still the Reynolds number.

The sensitivity analysis describes which input parameters have the main influences on the acoustic results. The distribution function of the results is plotted in order to verify how the single parameter affects the output variance. However, the physical meaning of each input is neglected and they are considered independent in order to reduce the complexity of the analysis. On the other hand, the present definition is useful to understand which quantities need more attentions.
Scatterplot provides a qualitative description. Global sensitivity factors allows to quantify the single input influences. The first order and the total indexes are enough accurate to establish the importance order for each model. The sensitivity analysis is repeated for a range of variance and frequency.

For each model the number of input parameters is different. Generally, the friction coefficient is a common parameter for all models and it is the most influential input, particularly for the Goody's one where its error influences the output variance for over 98% percent. For Kamruzzaman and Rozenberg the height of c_f is reduced until S_{c_f} assumes about 0.3 at low frequencies. It decreases by growing input variance and it modifies the importance order. The same trend is evident for Lee's model. The quantities δ^* and θ highly influences the models, mainly at high frequencies. The pressure gradient dp/dx is not mainly interesting as well as the δ thickness.
Although the first order allows to describe the single parameter affect, S_{tot} provides the combined effect with other input quantities. If S_{tot_i} is close to S_i, the input combination with other parameter is not relevant, while it became very important for high S_{tot_i} values.

The frequency effect is discussed from the analysis of output distribution function. The input variance is fixed to 0.2 and the output is plotted in order to capture the trend for low, medium and high frequency. The graphs show a different scale to evidence the phenomena. At high frequency, all models present output distribution function limited to very small variance. Thus, the model strength depends mainly on frequencies and very high value implies a lower influence of the input even if the variance is fixed. For this reason, for high frequency it is allowed higher error in input due to robust models. On the contrary, low frequencies introduces high variability in output.

The proposed approach is useful in many engineering application: from the analysis of wing acoustic emission to the noise of helicopter rotors, from the wind turbine design to ventilation system or turbomachinery. The advantages are mainly due to the computational cost and time; that has to be compared with result accuracy. The test cases show the Amiet's theory is suitable for thin airfoil while it has a good approximation also for asymmetrical profiles. Trailing edge prediction is accurate only for Kamruzzaman's pressure spectra model but it depends on angle of attack and geometry.
The present theory has margins of improvement. For example, introducing other pressure spectra models such as Blake TNO model and improving the back scattering. However, the most limitation is function of geometry studied in two-dimensional simulation. The future studies aim to extend the Amiet's formula for three dimensional body with complex geometry, warped and tripped, or equipped with acoustic regulators.

Acknowledgement

At the end of my thesis, that coincides with the end of an important phase of my life, I would like to write few words to thank my tutors and friends that believed in me during these years.

During my work I had to face with many arguments that I never studied before and I was able to overcome a series of issues, seemed insuperable, thanks to my tutors Professor Renzo Arina and Professor Andrea Ferrero, that answered all my questions and doubts. They always supported me and allowed me to develop an unusual topic, like aeroacoustics, in order to have good basis for my future project: I hope to continue my studies with a PhD program.

A special thanks to my friends that made my life very funny also during this last intense period. They listened to all my boring stories, even if they wanted to kill me, and helped me to fight my stress. I would like to tell them thanks for their support because they are now a sort of a second family: I feel a new man since I met them and I would like to live inside my second family.

Few words are dedicated to my parents, my brother and sister. They always encouraged me to continue my courses even if away from home. Now, I am an adult but without them I would never grew up as a person.

Appendix A

Computational method for Fresnel integrals

Numerical approach for Fresnel integrals are used to accelerate the acoustic model. The model was proposed by Mielenz [29] and it is based on Boersma solution. The Taylor expansions are not used because of the large number of constant to be determined. The analytical expression for Fresnel integrals is:

$$E(u) = \int_0^u \frac{1}{\sqrt{2\pi\tau}} e^{-i\tau} \mathrm{d}\tau = \frac{1-i}{2} + e^{-iu}\sqrt{\frac{4}{u}} \sum_{n=0}^{11} (p_n + iq_n) \left(\frac{4}{u}\right)^n ; \qquad (A.1)$$

where p_n and q_n are constants []. By introducing the substitution $t = \pi\tau^2/2$ and $x = \pi u^2/2$, the equation (A.1) can be written as:

$$E(x) = \int_0^x e^{-i\pi t^2/2} \mathrm{d}t = C(x) - iS(x) = \frac{1-i}{2} - e^{-i\pi x^2/2} \sum_{n=0}^{11} \frac{g_n - if_n}{x^{2n+1}} \quad for x \geq 1.6; \quad (A.2)$$

where

$$f_n = \left(\frac{8}{\pi}\right)^{n+1/2} q_n, \qquad g_n = -\left(\frac{8}{\pi}\right)^{n+1/2} p_n.$$

This method coincide with the Boersma solution and it presents an error less than $5\,10^{-10}$. In Table A.1 are reported the constant of Mielenz's computational method.

For $|x| \leq 1.6$ Taylor expansions are instead used. Thus,

$$\begin{aligned} C(x) &= \sum_{n=0}^{\infty} c_n x^{4n+1} \quad c_0 = 1. \\ c_{n+1} &= \frac{-\pi^2(4n+1)c_n}{4(2n+1)(2n+2)(4n+5)} \end{aligned} \qquad (A.3)$$

$$\begin{aligned} S(x) &= \sum_{n=0}^{\infty} s_n x^{4n+3} \quad s_0 = \pi/6, \\ s_{n+1} &= \frac{-\pi^2(4n+3)s_n}{4(2n+2)(2n+3)(4n+7)}. \end{aligned} \qquad (A.4)$$

n	f_n	g_n
0	0.318309844	0
1	9.34626 10^{-8}	0.101321519
2	-0.09676631	-4.07292 10^{-5}
3	0.000606222	-0.152068115
4	0.325539361	-0.046292605
5	0.325206461	1.622793598
6	-7.450551455	-5.199186089
7	32.20380908	7.477942354
8	-78.8035274	-0.695291507
9	118.5343352	-15.10996796
10	-102.4339798	22.28401942
11	39.06207702	-10.89968491

Table A.1: Table of constants for Mielenz's method.

The first eleven terms give an error less than $6\,10^{-10}$.

The Matlab©code is shown below.

```
function [y] = E(x)
%Function E allows to compute  Fresnel integrals by improving
    Mielenz's
%method.
f=[0.318309844  9.34626e 8  0.09676631  0.000606222  0.325539361
    0.325206461  7.450551455  32.20380908  78.8035274  118.5343352
     102.4339798  39.06207702];
g=[0  0.101321519  4.07292e 5  0.152068115  0.046292605
    1.622793598  5.199186089  7.477942354  0.695291507
     15.10996796  22.28401942  10.89968491];


x=pi*x.^2/2;
y=ones(1,length(x));


for j=1:length(x)

        if abs(x(j))>1.6
      y(j)=(1 1i)/2 exp( 1i*x(j).^2*pi/2)*sum((g 1i*f)./(x(j)
          .^(2*(0:11)+1)));
        else if abs(x(j))<1.6

            C=1.*x(j);
            S=pi/6.*x(j).^3;

```

```
21                for n=1:12
22
23            C=(1 pi^2*(4*n+1)/(4*(2*n+1)*(2*n+2)*(4*n+5)).*x(j)^(4*
                  n+1))*C;
24            S=(1 pi^2*(4*n+3)/(4*(2*n+2)*(2*n+3)*(4*n+7)).*x(j)^(4*
                  n+3))*S;
25
26                end
27      y(j)=C 1 i*S;
28   end
29            end
30
31 end
```

Appendix B

Farfield Roger's scattering solution

Roger's model was introduced in order to describe the directivity behavior of the sound emission for the Amiet's theory with back scattering correction. It is based on the hypothesis of finite chord formulation that is a limit of the present approach. However, Amiet proposed a good solution of the problem by defining the TE noise as not affected by the turbulent interaction on the leading edge. Roger and Al.[15] demonstrated the leading edge scattering correction allows to ddetermine the noise emission also for an observer not in the mid-span section and introduces a directivity for the signal that is not predicted by the original Amiet's solution. Furthermore, the authors based their deonstration on the Schwarzschild problem reformulated for the leading edge and summed to the previous solution. It became very important for low frequencies. The theory is extended also for three dimensional configuration.

The equation (1.36) is modified. The term L, given by the formula (1.38), is written as sum of two terms that are functions of the wave numbers $\bar{K}_x$ and $\bar{K}_y$, already defined in Chapter 1. However, $\bar{K}_y$ was fixed null because the gust was supposed to be directed along the chordwise; assumption valid for a mid-span observer. In general, the present assumption is not valid and contemplated in back scattering correction. Thus, the function $L(\bar{K}_x, \bar{K}_y)$ is obtained as:

$$L(\bar{K}_x, \bar{K}_y) = \int_{-2}^{0} f(\bar{x}) e^{-iC\bar{x}} \mathrm{d}\bar{x}, \tag{B.1}$$

where $f = f_1 + f_2$ and $\bar{x}$ the dimensionless coordinate.

Hence, the function

$$f_1 = (1+i)E(-B\bar{x}) - 1,$$

in which the constant $B = \bar{K}_x + M\mu + \bar{\kappa}$ and $\bar{\kappa} = \mu^2 - \bar{K}_y^2/\beta^2$. The parameter β and μ are already presented in Chapter 1.

The integral is now calculated by parts:

$$\int_{-2}^{0} f_1(\bar{x}) e^{-i\bar{x}} \mathrm{d}\bar{x} = -\frac{e^{2iC}}{iC} \left\{ (1+i)e^{-2iC} \sqrt{\frac{B}{B-C}} E(2(B-C)) - (1+i)E(2B) + 1 - e^{-2iC} \right\}. \tag{B.2}$$

The parameter

$$C = \bar{K}_x - \mu\left(\frac{x}{\sigma} - M\right).$$

The equation (B.2) collapses into the Amiet's proposed formula for $\bar{K}_y = 0$.

The correction is introduced by the function f_2, which presents a complex formulation. The constant $\epsilon = \sqrt{1 - 1/(4\mu)}$ has to be introduced. With the annotation $\{\cdot\}^2$, it indicates that the imaginary part is multiplied by ϵ. Thus, the analytical expression of integral is:

$$\frac{1}{H}\int_{-2}^{0} f_2 e^{iC\bar{x}}\mathrm{d}\bar{x} = \left\{e^{4i\bar{\kappa}}\left[1-(1+i)E(4\bar{\kappa})\right]\right\}^c - e^{2iD} + i\left[D + \bar{K}_x + M\mu - \bar{\kappa}\right]G; \quad \text{(B.3)}$$

where

$$H = \frac{(1+i)e^{-4i\bar{\kappa}}(1-\Theta^2)}{2\sqrt{\pi}(U_\infty/U_c - 1)\bar{K}\sqrt{B}}.$$

end $D = \bar{\kappa} - x/\sigma$. The function G is defined as:

$$\begin{aligned} G = (1+\epsilon)e^{i(2\bar{\kappa})+D}\frac{\sin(D-2\bar{\kappa})}{D-2\bar{\kappa}} + (1-\epsilon)e^{i(-2\bar{\kappa}+D)}\frac{\sin(D+2\bar{\kappa})}{D+2\bar{\kappa}} + \\ \frac{(1+\epsilon)(1-i)}{2(D-2\bar{\kappa})}e^{4i\bar{\kappa}}E(4\bar{\kappa}) - \frac{(1-\epsilon)(1+i)}{2(D+2\bar{\kappa})}e^{-4i\bar{\kappa}}E(4\bar{\kappa}) \\ + \frac{e^{2iD}}{2}\sqrt{\frac{2\bar{\kappa}}{D}}E(2D)\left[\frac{(1+i)(1-\epsilon)}{D+2\bar{\kappa}} - \frac{(1-i)(1+\epsilon)}{D-2\bar{\kappa}}\right]. \end{aligned} \quad \text{(B.4)}$$

The present result is applied to compute the corresponding power spectral density of the far-field sound as presented in Chapter 1.

Bibliography

[1] R. K. Amiet. Acoustic radiation from an airfoil in a turbulent stream. *Journal of Sound and Vibration*, 41:407–420, 1975.

[2] M. Goody. Empirical spectral model of surface pressure fluctuations. *AIAA Journal, American Institute of Aeronautics and Astronautics*, 42:1788–1794, 2004.

[3] Gilles Robert Y. Rozenberg and S. Moreau. Wall-pressure spectral model including the adverse pressure gradient effects. *AIAA Journal, American Institute of Aeronautics and Astronautics*, 50:2168–2179, 2012.

[4] Th. Lutz W. Würz M. Kamruzzaman, D. Bekiropoulos and E. Krämer. A semi-empirical surface pressure spectrum model for airfoil trailing-edge noise prediction. *Aeroacoustics*, 14:833–882, 2015.

[5] S. Lee and A. Villaescusa. Comparison and assessment of recent empirical models for turbulent boundary layer wall pressure spectrum. *23rd AIAA/CEAS Aeroacoustics Conference*, 2017.

[6] D. Pope T. Brooks and M. Marcolini. Airfoil self-noise and prediction. *NASA reference publication*, 1989.

[7] Rautmann M. Kamruzzaman D. Bekiropoulos A. Iob R. Arina P. Battern S. Chakravarthy F. Bertagnolio M. Herr, R. Ewert. Broadband trailing-edge noise predictions: Overview of banc-iii results. *21st AIAA/CEAS Aeroacoustics Conference*, 2015.

[8] A. Guédel M. Roger, S. Moreau. Vortex-shedding noise and potential-interaction noise modeling by reversed sears' problem. *12th AIAA/CEAS Aeroacoustics Conference*, 2006.

[9] A. Powell. On the aerodynamic noise of a rigid flat plate moving at zero incidence. *Journal of Acoustical Society of America*, 31:1649–1653, 1959.

[10] D. G. Crighton. Radiation properties of a semi-infinite vortex sheet. *Proceeding of the Royal Society London*, A330:185–198, 1972.

[11] D. S. Jones. Aerodynamic sound due to a source near half-plate. *Journal of the Institute of Mathematics and its Applications*, 9:114–122, 1972.

[12] D. M. Chase. Sound radiated by turbulent flow off a rigid half-plane as obtained from a wavevector spectrum af hydrodynamic pressure. *Journal of the Acoustical Society of America*, 52:1011–1023, 1972.

[13] D. M. Chase. Noise radiated from an edge in turbulent flow. *American Institute of Aeronautics and Astronautics Journal*, 13:1041–1047, 1975.

[14] M. Landahl. Unsteady transonic flow. *New York:Pergamon Press, Inc.*, pages 27–30, 1961.

[15] S. Moreau M. Roger. Back-scattering correction and further extensions of amiet's trailing-edge noise model. part 1:theory. *Journal of Sound and Vibration*, 286:477–506, 2005.

[16] M. S. Howe. A review of the theory of trailing edge noise. *Journal of Sound and Vibration*, 61:437–465, 1978.

[17] J. Christophe Y. C. Küçükosman and C. Schran. Rans-based trailing-edge noise prediction using amiet's theory:accuracy and mesh sensitivity of semi-empirical and integral wall pressure models. *AIAA/CEAS Aeroacoustics Conference*, 2018.

[18] S.K. Lele W.R. Wolf. Investigation of the noise generated by a du96 airfoil. *AIAA Aeroacoustic Conference*, 2012.

[19] R. van Rooij W.A. Timmer. Summary of the delft university wind turbine dedicated airfoils. *AIAA Aeroacoustic Conference*, 2003.

[20] F. Avallone D. Ragni R. Merino Martinez, W. van der Velden. Acoustic measurements of a du96-w-180 airfoil with flow-misaligned serrations at high reynold number in a closed-section wind tunnel. *17th International Conference on Wind Turbine Noise*, 2017.

[21] R. K. Amiet. Compressibility effects of in unsteady thin-airfoil theory. *American Institute of Aeronautics and Astronautics Journal*, 12:253–255, 1974.

[22] J. M. R. Graham. Similarity rules for thin airfoils in non-stationarity flow. *Journal of Fluid Mechanism*, 43:753–766, 1970.

[23] R. K. Amiet. High frequencies thin-airfoil theory for subsonic flow. *American Institute of Aeronautics and Astronautics Journal*, 14:1076–1082, 1976.

[24] S. R. Allmaras P.R. Spalart. A one equation turbulnece model for aerodynamic flows. *La Recherche Aérospatiale*, 1:5–21, 1994.

[25] F. T. Johnson P.R. Spalart, S. R. Allmaras. Modifications and clarifications for the implementation of the spalart-allmaras turbulence model. *Seventh International Conference on Computational Fluid Dynamics*, 2012.

[26] T. Andres F. Campolongo J. Cariboni D. Gatelli M. Saisana A. Saltelli, M. Ratto and S. Tarantola. *Global sensitivity Analysis: The primer*. John Wiley and Sons, 2008.

[27] A. Saltelli T. Homma. Importance measures in global sensitivity analysis of non linear models. *Reliability Engineering and System Safety*, 52:1–17, 1996.

[28] A. Ferrero. Computational fluid dynamics for aerospace propulsion systems: an approach based on discontinuous finite elements.

[29] K. D. Mielenz. Computation of fresnel integrals. *Journal of Research of the National Institute of Standards and Technology*, 105:589–590, 2000.